

6. SITE 719: BENGAL FAN¹

Shipboard Scientific Party²

HOLE 719A

Date occupied: 2 August 1987
Date departed: 6 August 1987
Time on hole: 3.9 days
Position: 0°57.646'S, 81° 23.967'E
Water depth (sea level, m, bottom felt): 4736.8
Penetration (m): 460.2
Number of cores: 49
Total length of cored section (m): 460.2
Total core recovered (m): 185.53
Core recovery (%): 40.3
Deepest sedimentary unit cored:
Depth sub-bottom (m): 357.0
Nature: silty and silty mud turbidites
Age: late Miocene
Measured vertical sound velocity (km/s): 1.75

HOLE 719B

Date occupied: 6 August 1987
Date departed: 9 August 1987
Time on hole: 2.4 days
Position: 0°57.646'S, 81°23.967'E
Water depth (sea level, m, bottom felt): 4736.8
Penetration (m): 465.6
Number of cores: 0
Total length of cored section (m): 0
Deepest sedimentary unit cored: none

SITE SUMMARY

Site 719 is located in the central Indian Ocean approximately 800 km south of Sri Lanka and 200 km northwest of the Afanazy Nikitin seamount group (Fig. 1). It lies at the distal end of the Bengal Fan within a large region of intraplate deformation, which affects both the basement and the overlying sediments. Site 719 is located near the center of one of the tilted fault blocks that make up the tectonic fabric of the region. It was designed as a companion site to Site 717, located 3.2 km to the northwest on the northern (lower) edge of the same block. Site 717 cored a complete syn-deformation sequence in the axis of a synclinal structure developed in the sediments. Site 719 is located part way up the fault block, in an area where the syn-deformation sedimentary sequence is attenuated, to determine the time of deformation and the history of motion on the block

through a comparison of the sedimentary record at the two sites.

Site 719 consists of two holes. Hole 719A, consisting of one APC core, penetrating 4.2 m and recovering 4.27 m (101%), and 48 XCB cores, penetrating 456 m and recovering 181.26 m (39.8%), obtained a section through the syn-deformational sediments. Hole 719B was drilled to 465.6 m and was utilized for three successful logging runs.

Principal drilling results. The stratigraphic section recovered at Site 719 ranges from late Quaternary to late Miocene in age and has been divided into five main lithologic units. The dominant lithologies and ages of the stratigraphic sequence are as follows.

Unit I (0.0–4.0 mbsf): Clay and calcareous clay and mud of Holocene to latest Pleistocene age.

Unit II (4.0–135.0 mbsf): Micaceous silt and silty mud turbidites with thin intervening muds of late Pleistocene age.

Unit III (135.0–207.0 mbsf): Mud turbidites and biogenic mud turbidites with thin interbedded pelagic clays of Pleistocene to early Pliocene age.

Subunit IVA (207.0–240.0 mbsf): Silt turbidites with thin muds and mud turbidites of early Pliocene age.

Subunit IVB (240.0–357.0 mbsf): Mud turbidites with interbedded pelagic clays of early Pliocene and late Miocene age.

Subunit V (357.0–460.2 mbsf): Silt and silty mud turbidites with rare intervals of pelagic clay and organic rich mud turbidites of late Miocene age.

Sedimentation at Site 719 has been almost exclusively through fan deposition processes, and the section consists primarily of a sequence of turbidites. A thin layer of mud and calcareous mud (4 m) overlies a sequence of silty turbidites that accumulated very rapidly during the late Pleistocene. Units III and IV together represent a section of mainly muddy turbidites that accumulated during the late Miocene and Pliocene. It is within these units that most of the attenuation of the sedimentary section between Sites 717 and 719 occurs. The lowest unit consists of a monotonous sequence of micaceous silt and silty mud turbidites with thin interbedded clays. The seismic horizon that marks the onset of deformation occurs within Unit V and does not represent a lithologic boundary.

The sedimentary section at Site 719 corresponds very closely to the section obtained at Site 717, and in many instances distinctive individual turbidites and turbidite sequences can be correlated between the two sites. Attenuation of the section between Sites 717 and 719 appears to have occurred through a combination of pinch outs and thinning of individual beds. The limiting factor in determining the deformation history will probably prove to be the age resolution that can be obtained. Biostratigraphic control at all of Site 719 is provided primarily through nannofossils as the other microfossil groups are either poorly preserved or absent. Preliminary shipboard studies suggest that the rotation of the fault block has occurred throughout the period of intraplate deformation at a fairly constant rate.

BACKGROUND AND OBJECTIVES

Background

Site 719 is the third of three closely-spaced sites located near 1°S, 81°24'E in the central Indian Ocean and is designed as a

¹ Cochran, J. R., Stow, D.A.V., et al., 1988. *Proc. ODP, Init. Repts.*, 116: College Station, TX (Ocean Drilling Program).

² Shipboard Scientific Party is as given in the list of Participants preceding the contents.

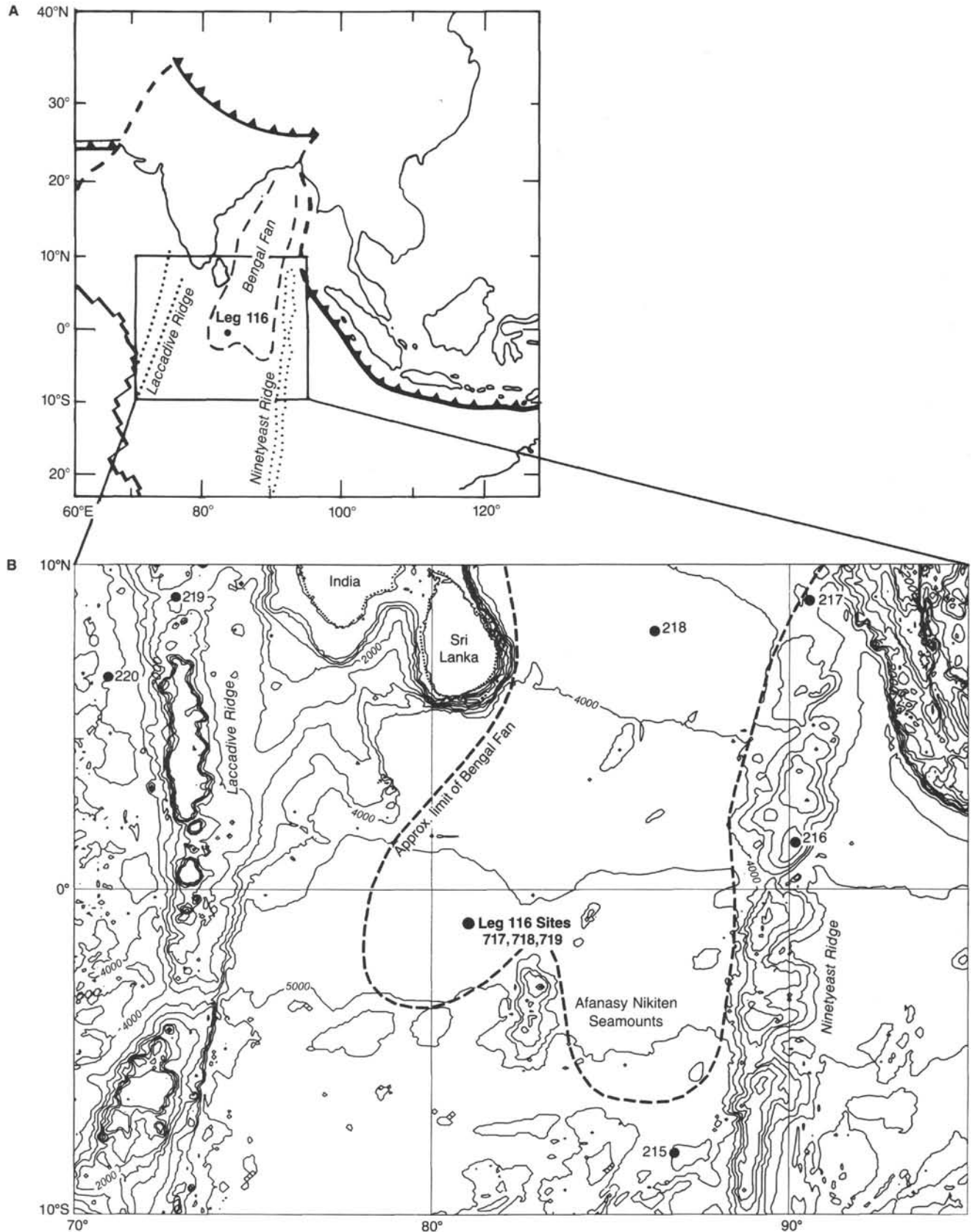


Figure 1. Location map for Leg 116 sites. (A) Setting of the Leg 116 sites relative to tectonic elements of the eastern Indian Ocean. Heavy solid line represents mid-ocean ridge axes, dashed lines are transform plate boundaries and saw-tooth pattern shows convergent plate boundaries. (B) Geologic setting of Leg 116 sites within the north central Indian Ocean. Bathymetry is machine-contoured DBDB10 gridded data at 500-m intervals. Location of other DSDP drill sites within the region is also shown.

companion site to Site 717, located 3.2 km to the north-northwest. The sites are located at the distal end of the Bengal Fan approximately 800 km south of Sri Lanka and 200 km northwest of the Afanazy Nikitin Seamount Group. They are within a large area of intraplate deformation that affects both the oceanic crust and the thick pile of overlying sediments.

Both deposition and deformation in this part of the central Indian Ocean have been affected by the collision between the Indian and Eurasian Plates. The continental portions of these plates began to interact during the Eocene at Anomaly 22 time (approximately 53 Ma) with a *soft* collision, probably between continental India and an island arc lying seaward of Asia (Curry et al., 1982). This collision resulted in a reduction of the spreading half-rate from 8 cm/yr to about 4 cm/yr (Sclater and Fisher, 1974). A regional unconformity observed on seismic profiles in the proximal- and mid-fan areas (Curry and Moore, 1971) has been dated to this time by extrapolation from DSDP Site 217 (Moore et al., 1974).

During the Oligocene, the spreading half-rate decreased further to 2.5 cm/yr, the direction of spreading on the southeast Indian Ridge changed from N-S to NE-SW (Sclater et al., 1976), and sedimentation in the region now covered by the Bengal Fan probably increased (Powell and Conaghan, 1973). The *hard* continent-continent collision may have occurred at that time, although other estimates are as late as upper Miocene (Powell and Conaghan, 1973; Gansser, 1964, 1981). A second major regional unconformity in the area of the Bengal Fan has also been dated as late Miocene by drilling at DSDP Site 218 (von der Borch, Sclater, et al., 1974). The unconformity marking the onset of deformation in the distal fan (Unconformity "A", Fig. 2) is inferred by extrapolation to be the same event (Weissel et al., 1980).

Rapid terrigenous sedimentation on an incipient Bengal Fan began in the Eocene as a response to the first intraplate collision and has continued to the present, building the world's largest submarine fan. The Bengal Fan is over 2500 km long and is more than 16 km thick under the northern Bay of Bengal (Curry et al., 1982). In the area of the Leg 116 sites, the sediments are about 1.5 to 2 km (2 s of two-way traveltime) thick under the distal part of the fan.

This enormous volume of sediments is assumed to have been derived principally from denudation of the uplifting Himalayan Mountains and then supplied to the delta front via the Ganges-Brahmaputra river systems. Sediments are funneled very efficiently to the fan via a delta-front trough, the "Swatch of No Ground." This trough is presently connected to only one active fan channel, but has been effectively cut off from rapid sediment supply since the most recent rise in sea level, probably about 7,000–10,000 yr ago (Emmel and Curry, 1983). The active fan channel appears to terminate some 50–100 km north of the Leg 116 sites and no channel- or levee-type features have been observed on seismic records in the vicinity of the Leg 116 area.

Increased resistance to subduction, and shortening across the Himalayas since the continent-continent collision, combined with continued spreading on the southeast Indian Ridge, has placed the central Indian Ocean under a large N-S compressive stress regime (Stein and Okal, 1978). As a result, the oceanic crust and most of the overlying sediments have been deformed into long-wavelength (100–300 km) undulations with peak-to-trough amplitudes of 1 to 3 km over a large area. This area extends from the Chagos-Laccadive Ridge in the west to the Ninety East Ridge and from 5° N to 10° S latitude (Weissel et al., 1980; Geller et al., 1983).

Superimposed on the long-wavelength undulations are faulted and rotated blocks, 5–20 km wide, interpreted as showing a re-

verse sense of displacement on the faults separating them (Geller et al., 1983), consistent with N-S compression. The top of the oceanic crust is seen to be offset across these faults by up to 0.5 s (approximately 0.5 km) on seismic reflection records (Fig. 2). The lower portion of the sedimentary sequence is characterized by reflectors which are parallel to the basement, and the sequence is assumed to predate the deformation. A prominent unconformity (Unconformity "A", Fig. 2) separates the predeformation sequence from an upper syn-deformation sequence, which thins toward the top of the blocks and shows pinching out of individual reflectors.

Objectives

Site 719 is located in 4737 m of water, near the center of same fault block on which Site 717 is situated. Site 717 was situated in the thickest part of the sedimentary section between adjacent block highs in a location where the seismic reflection records suggested that sedimentation has been nearly continuous (Fig. 2). Site 719 is located part way up the fault block where the syn-deformation sediments have thinned from 0.70 s at Site 717 to 0.52 s. A well-defined unconformity (Unconformity "A") is developed separating pre- and syn-deformation sediments and in addition the section appears to have thinned through the pinching out of reflectors. The principal objectives of Site 719, were as follows:

1. To determine the sedimentary sequence within an area affected by rotation of the fault block and by comparison with Site 717 to determine the history of motion and uplift;
2. To characterize the main lithofacies and determine the depositional processes responsible;
3. To establish the provenance of the sediments on the distal fan and to assess to what extent compositional variations reflect the uplift history of the Himalayas;
4. To characterize the nature of early diagenesis in deep-water fan sediments; and
5. To measure the physical and hydrological properties of sediments in an actively deforming area.

OPERATIONS

JOIDES Resolution moved the 7 km from Sites 718 to 719 in dynamic positioning mode with 4500 m of drill pipe suspended under the ship. This was more time efficient than carrying out a full round trip, and a seismic line had already been run over the site during the short survey between the two previous sites. The beacon was dropped at 0°57.6'S, 81°23.95'E at 2045 hr on 2 August.

The bit was positioned just above the seafloor with the aid of the TV camera and the APC core barrel fired to spud Hole 719A. The mud line was established at 4747.3 m below the rig floor and one 4.2-m core was brought on deck at 2300 hr on 2 August. The rest of the hole was cored continuously to a depth of 460.2 mbsf using the XCB system. The last core was brought on deck at 0415 hr on 6 August, giving an average core recovery of 40.3% that was good in the mud lithologies and poor in the silts. Details of the coring operation are given in Table 1.

A round trip was made to avoid using a bit-release assembly, and a second hole was drilled after moving the ship 10 m. Hole 719B was then drilled ahead to 466 mbsf and conditioned for use as a dedicated logging hole. Four successful logging runs were made, using three separate tool strings, from the bottom of the hole to the seafloor. During logging operations the drill pipe was positioned at 143 mbsf. Following completion of the logging, pipe was pulled as the ship returned to Site 718 in dynamic positioning mode.

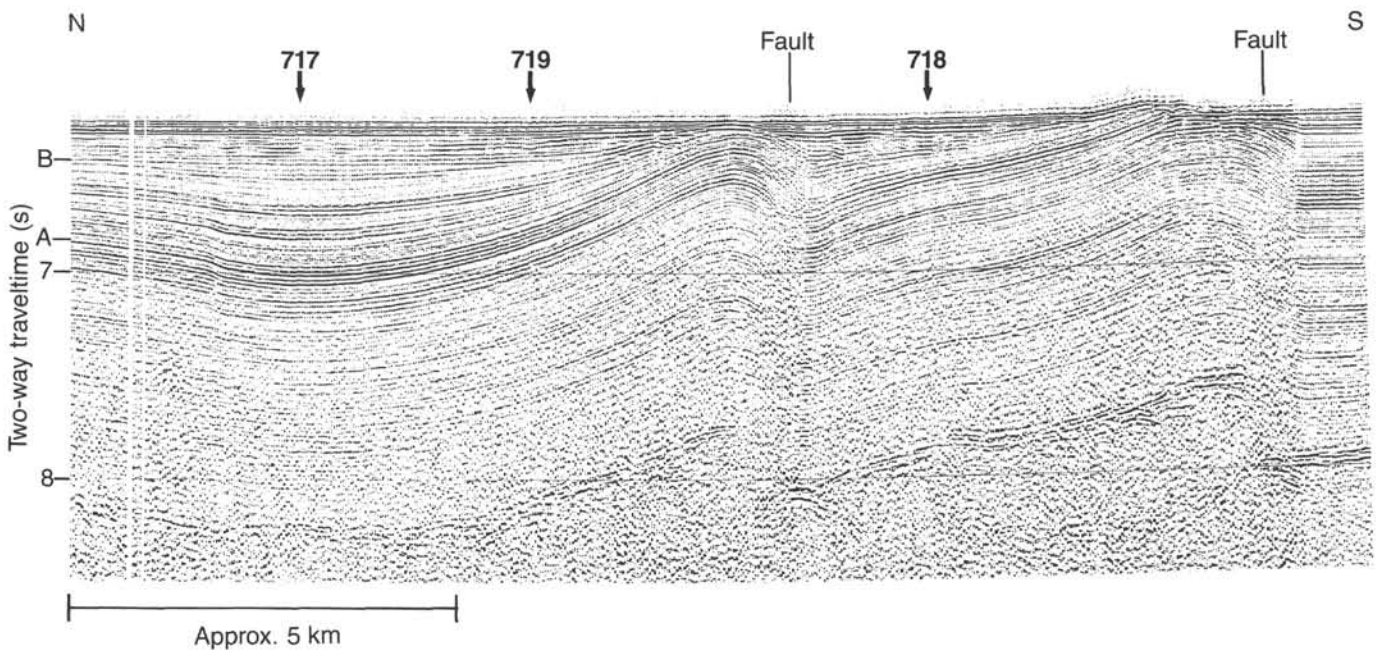


Figure 2. North-south seismic reflection profile across the Leg 116 drill sites. Locations of Sites 717, 718, and 719 are shown. Also noted are the locations of the faults bounding the tilted blocks and prominent unconformities "A" and "B".

LITHOSTRATIGRAPHY

Lithofacies

The stratigraphic sequence recovered at Site 719 consists predominantly of interbedded clays, silty clays, and silts, with lesser amounts of sandy silts and calcareous clay, ranging in age from Quaternary to late Miocene. The sediments can be divided into seven distinct facies on the basis of texture, sedimentary and biogenic structures, color, organic carbon content, and the presence or absence of calcareous microfossils.

Facies 1. Silt and Silt-Mud Turbidites (F1)

Facies 1 consists of sharp-based upward-fining beds of dark-gray silt or, less commonly, sandy silt, which grade upward through silty clay to clay. Internally the beds may be massive or rarely show a faint horizontal lamination in the basal few centimeters. The beds of this facies range from 5 to 95 cm thick, averaging 40 cm. Silt fractions are very micaceous (5–15%), generally quartz-rich (50–70%) and often slightly calcareous (2–10% calcite). Bioturbation and calcareous microfossils are rare.

Facies 2. Organic-poor Mud Turbidites (F2)

Facies 2 consists of sharp-based, 5- to 80-cm thick (average 33 cm) beds of light gray to gray, silty clays which pass upward into clay. Typically silt comprises only 10% of this facies. The bases of beds are often marked by 0.5- to 3.0-mm thick quartz-rich basal silt laminae. The silt fraction consists mainly of quartz with mica (less than 10%) and feldspar (traces). Plant debris ranges from zero to 1% and calcareous microfossils are largely absent. Bioturbation is common in the upper portion of beds and may extend downward through much of the bed. In some cases bioturbation is so extensive that even the bottom boundary appears bioturbated and gradational. The true turbidite nature of these beds becomes doubtful.

Facies 3. Organic-rich Mud Turbidites (F3)

Facies 3 is characterized by large amounts (2–15%, avg. 5%) of plant debris and consists of very dark-gray to black, sharp-based, upward-fining beds 5- to 50-cm thick (avg. 17 cm) of

silty clay (Fig. 3). The beds generally commence with clayey silts (less than 80% silt) and pass upward into clay. Typically the basal few centimeters exhibit a horizontal lamination that passes upward into a faint wispy lamination and finally a massive interval. The tops of the beds are commonly bioturbated and, as with Facies 2, this bioturbation may extend downwards through much of the bed. In some cases the bioturbation appears to have been caused by organisms burrowing upward from the underlying unit (Fig. 4). These beds are less clearly of true turbidite origin. Pyrite, or an iron sulfide precursor, (after wood, burrows, and as concretions) is ubiquitous (see below).

Facies 4. Biogenic Mud Turbidites (F4)

This facies consists of sharp-based, upward fining, olive-gray calcareous silty clays (with a silt content less than 10%) and clay. Beds of this facies are found only in lithologic Unit III except for a single example in Unit IV, and range in thickness from 18 to 110 cm (avg. 58 cm). There is a tendency for bed thickness to increase upsection. A thin (less than 3 cm) basal calcareous silt layer may occur. Rarely, a faint horizontal lamination is present, particularly at the base, but most commonly the beds appear massive. In contrast to the other facies (with the exception of the basal silts of Facies 6) calcareous microfossils (mainly nannofossils, but with many foraminifers) are ubiquitous, making up to 20% of the sediment. In addition, unidentified calcareous silt and clay-sized material account for 20–30% of the sediment. The tops of the beds are commonly bioturbated.

In Core 116-719A-18X a 6-cm laminated white chalk was observed within lithologic Unit III that may correlate with a similar chalky horizon at Site 717.

Facies 5. Pelagic Clays (F5)

This facies consists of gradationally based beds of clay 5–10 cm thick, varying in color from a mottled green to whitish gray. Moderate to intense bioturbation characterizes the facies. Common trace fossils include chondrites, planolites, and zoophycos. Ferromanganiferous(?) chemical fronts characterize the gray clays of this facies. Calcareous microfossils are rare to absent; those that remain show evidence of extreme dissolution.

Table 1. Coring summary for Site 719.

Core no.	Date Aug. 1987	Time	Sub-bottom top (mbsf)	Sub-bottom bottom (mbsf)	Meters cored (m)	Meters recovered (m)	Percent recovery
1H	02	2300	0.0	4.2	4.2	4.27	101.0
2X	03	0315	4.2	13.7	9.5	1.53	16.1
3X	03	0425	13.7	23.2	9.5	0.10	1.1
4X	03	0540	23.2	32.7	9.5	0.72	7.6
5X	03	0625	32.7	42.2	9.5	0.86	9.1
6X	03	0750	42.2	51.7	9.5	0.64	6.7
7X	03	0845	51.7	61.2	9.5	0.67	7.1
8X	03	1210	61.2	70.7	9.5	0.94	9.9
9X	03	1305	70.7	80.2	9.5	0.06	0.6
10X	03	1410	80.2	89.7	9.5	0.14	1.5
11X	03	1710	89.7	99.2	9.5	1.35	14.2
12X	03	1800	99.2	108.7	9.5	1.30	13.7
13X	03	1900	108.7	118.2	9.5	1.14	12.0
14X	03	2240	118.2	127.7	9.5	2.63	27.7
15X	03	2355	127.7	137.2	9.5	0.74	7.8
16X	04	0125	137.2	146.7	9.5	10.00	105.2
17X	04	0310	146.7	156.2	9.5	9.97	105.0
18X	04	0940	156.2	165.7	9.5	9.96	105.0
19X	04	1110	165.7	175.2	9.5	4.40	46.3
20X	04	1240	175.2	184.7	9.5	9.54	100.0
21X	04	1405	184.7	194.2	9.5	4.10	43.1
22X	04	1515	194.2	203.7	9.5	9.14	96.2
23X	04	1635	203.7	213.2	9.5	3.30	34.7
24X	04	1750	213.2	222.7	9.5	1.34	14.1
25X	04	1900	222.7	232.2	9.5	1.07	11.2
26X	04	2020	232.2	241.7	9.5	1.19	12.5
27X	04	2140	241.7	251.2	9.5	3.30	34.7
28X	04	2250	251.2	260.7	9.5	10.14	106.7
29X	05	0005	260.7	270.2	9.5	4.25	44.7
30X	05	0130	270.2	279.7	9.5	9.95	105.0
31X	05	0240	279.7	289.2	9.5	9.35	98.4
32X	05	0400	289.2	298.7	9.5	4.05	42.6
33X	05	0520	298.7	308.2	9.5	2.64	27.8
34X	05	0640	308.2	317.7	9.5	9.57	101.0
35X	05	0750	317.7	327.2	9.5	5.28	55.6
36X	05	0905	327.2	336.7	9.5	8.82	92.8
37X	05	1045	336.7	346.2	9.5	8.74	92.0
38X	05	1155	346.2	355.7	9.5	8.10	85.2
39X	05	1310	355.7	365.2	9.5	1.83	19.2
40X	05	1420	365.2	374.7	9.5	0.65	6.8
41X	05	1535	374.7	384.2	9.5	0.47	5.0
42X	05	1700	384.2	393.7	9.5	1.45	15.2
43X	05	1825	393.7	403.2	9.5	0.98	10.3
44X	05	1950	403.2	412.7	9.5	0.93	9.8
45X	05	2100	412.7	422.2	9.5	0.94	9.9
46X	05	2240	422.2	431.7	9.5	0.85	9.0
47X	06	0030	431.7	441.2	9.5	1.14	12.0
48X	06	0215	441.2	450.7	9.5	9.97	105.0
49X	06	0415	450.7	460.2	9.5	1.03	10.8
					460.2	185.53	

Facies 6. Pelagic Calcareous Clays (F6)

Facies 6 consists of light- to dark-gray calcareous bioturbated clays (50–85 cm thick) with approximately 5% silt. It is characterized by an abundant fauna of nannofossils (up to 30%) and foraminifers (up to 5%). Bioturbation is common and intense.

Facies 7. Structureless Muds (F7)

Facies 7 consists of beds (10–60 cm thick) of dark- to light-gray silty clay and clay with indistinct bed boundaries. The beds tend to be bioturbated throughout. Ferro-manganiferous(?) chemical fronts are absent. Calcareous microfossils are largely absent but occasionally occur in trace amounts.

These facies are very similar to those of Site 717. There is a tendency for both silt and mud turbidite facies (Facies 1–3) to be thinner at Site 719 than at Site 717. The biogenic mud turbidites show a similar trend.

Lithologic Units

On the basis of the distribution of the facies identified, the sedimentary sequence penetrated at Site 719 has been divided into five lithologic units, which correspond with units identified in nearby Site 717 (Fig. 5).

Unit I. Cores 116-719A-1H; 0 to 4 mbsf

Unit I is 4.0 m thick and is composed of interbedded structureless muds (F7), organic-poor mud turbidites (F2), and calcareous clays (F6). This unit was piston cored and the recovery was 100%.

Unit II. Cores 116-719A-2X to 116-719A-15X; 4.0 to 135 mbsf

Unit II consists of 131.0 m of predominantly Facies I silt and silt-mud turbidites, with thin interbeds of structureless muds (F7). Recovery for this unit was very poor (approximately 10%).

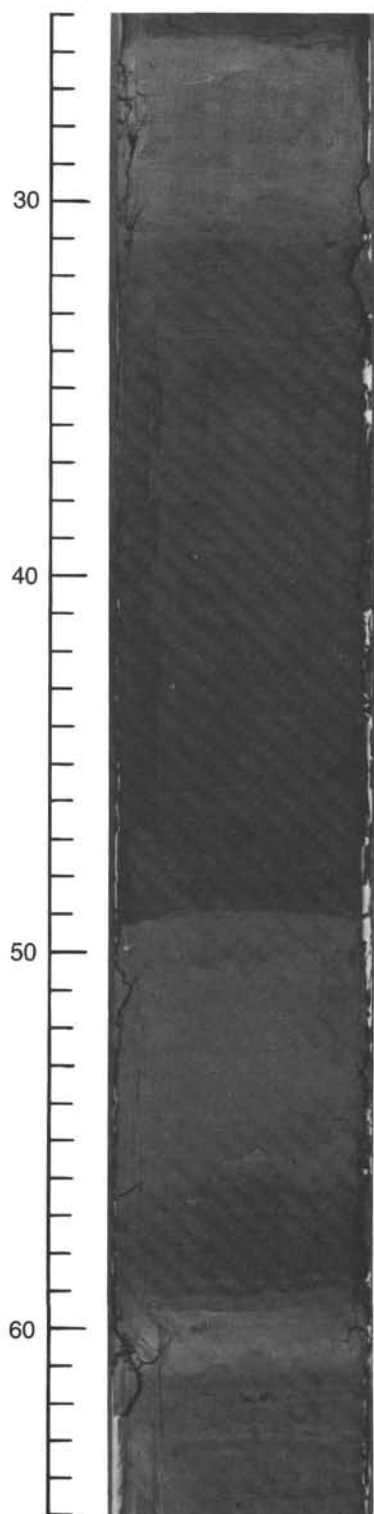


Figure 3. Photograph of organic-rich mud turbidite cycle (Section 116-719A-16X-6).

Unit III. Cores 116-719A-16X to 116-719A-23X; 135 to 207 mbsf

Unit III is 72 m thick and is characterized by the presence of biogenic mud turbidites (F4), which decrease in abundance with depth through the unit. Interbedded with the biogenic mud turbidites are organic-poor (F2) and organic-rich mud turbidites

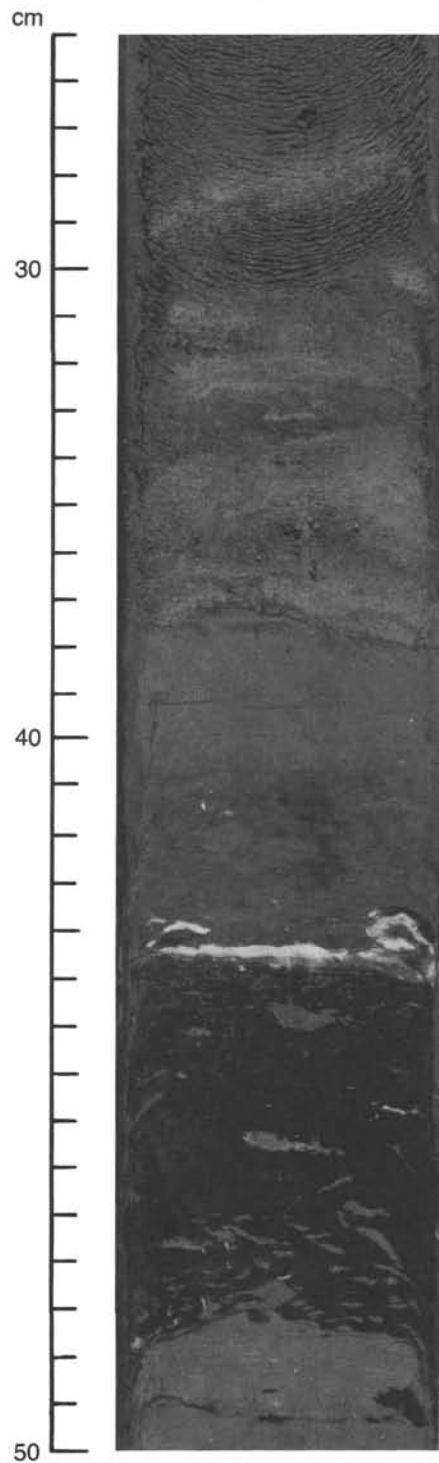


Figure 4. Photograph of organic-rich mud turbidite cycle showing bioturbation at base (Section 116-719A-36X-6).

(F3), together with structureless muds (F7), calcareous clays (F6), and pelagic clays (F5). Both Facies F5 and F6 tend to occur as thin *caps* on the mud turbidite facies. Recovery was approximately 84%.

Unit IV. Cores 116-719A-23X to 116-719A-39X; 207 to 357 mbsf

At Site 717 this unit was subdivided into four subunits on the basis of the presence, abundance, and thickness of silt and silt-

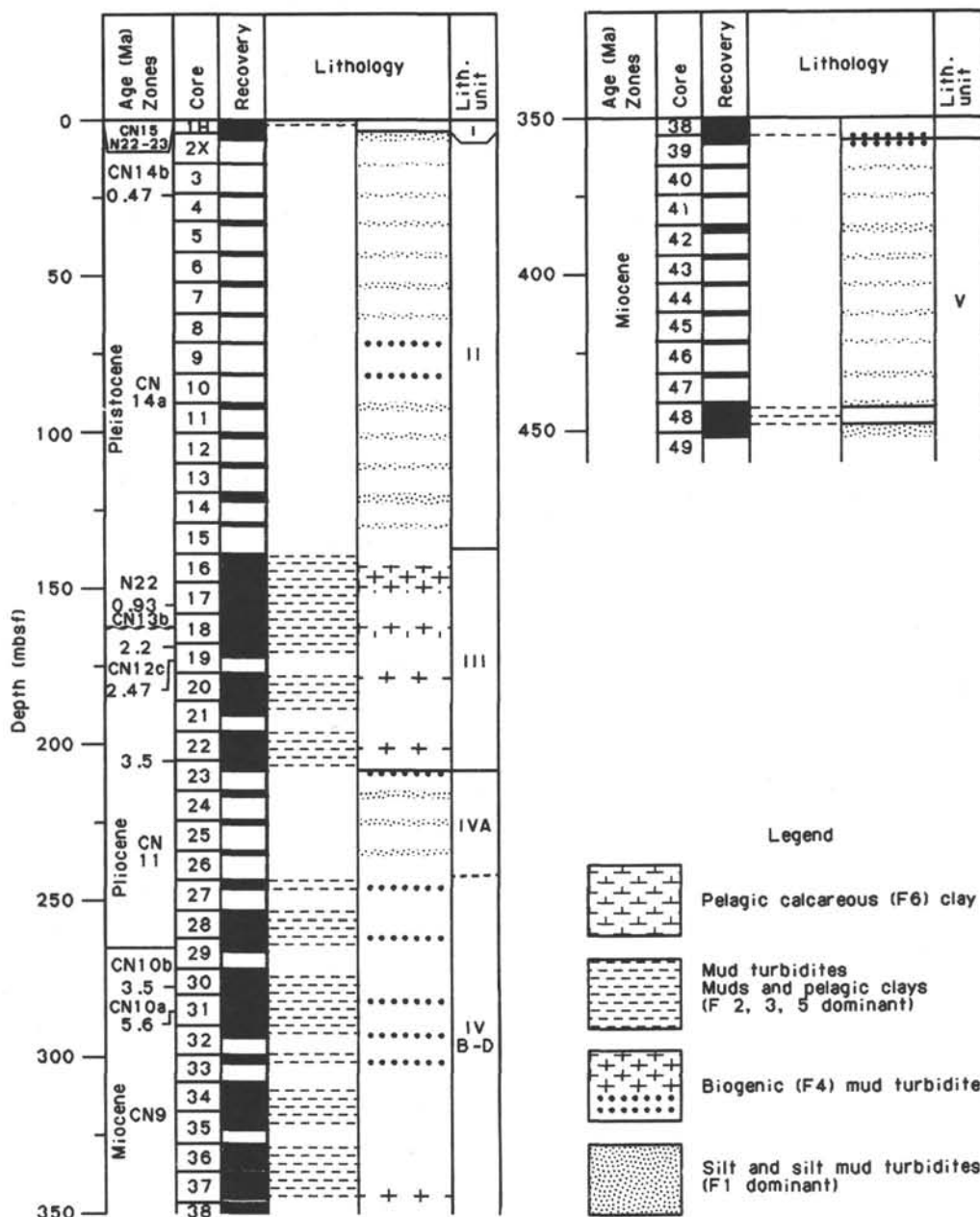


Figure 5. Lithostratigraphy of Site 719.

mud turbidites. At Site 719 Subunits IVB, IVC, and IVD cannot be differentiated so are considered here as a single composite subunit, IVB-D.

Subunit IVA. Cores 116-719A-23X to 116-719A-26X; 207 to 240 mbsf

Subunit IVA is 33 m thick and is characterized by an abundance of silt turbidites of Facies 1, although thin structureless muds (F7) and mud turbidites of Facies 2 and 3 also occur. Recovery was approximately 11%.

Subunit IVB/D. Cores 116-719A-27X to 116-719A-39X; 240 to 357 mbsf

Subunits IVB/D total 117 m thick and consist of interbedded organic-rich (F3) and organic-poor (F2) mud turbidites, structureless muds (F7), and pelagic clays (F5), differing from Unit III in that the biogenic mud turbidites (F4) are largely ab-

sent and that rare silt-mud turbidites (F1) occur. Recovery was approximately 73%.

Unit V. Cores 116-719A-39X to 116-719A-49X; 357 to 460.2 mbsf

This unit is a monotonous sequence (103.2 m thick) of predominantly silt and silt-mud turbidites (F1) with rare, thin intervals of pelagic calcareous clay (F6), structureless mud (F7), and organic-rich mud turbidites (F3). Recovery was approximately 18%.

Maximum Quartz Grain Size

Maximum grain size was determined at approximately 10-m intervals down Hole 719. In each case the coarsest and/or thickest lithology in the individual core (generally from the base of the coarsest turbidite) was chosen for smear-slide analysis and

the largest equant quartz grain measured. Results of the analysis are shown graphically in Figure 6.

Analysis reveals that the maximum grain size range is from 30 to 565 μm (coarse silt to coarse sand on the Wentworth Scale). As at Site 717 the coarsest maximum grain size corresponds to the sandy silt and silt turbidites of Facies 1 within lithologic Units II and V. Maximum grain size in Unit IVa only reaches 240 μm (fine sand). However, the background values throughout the sequence show that coarse silt-sized material was able to reach this most distal fan setting via turbidity currents throughout the interval from the late Miocene to the Quaternary sampled at Site 719.

Carbonate Content

Results of analysis of carbonate content at Site 719 are shown in Figure 7. Carbonate values for most of the core are low (0–10%), but at several horizons values of 30–50% are seen. Most of these very high values probably correspond to the biogenic mud turbidite facies (F4), reflecting their high biogenic calcite content. The high value near the seabed corresponds with pelagic calcareous clays of Facies 6. The peak at approximately 320-m depth corresponds with a thin whitish colored biogenic turbidite that appears to correlate with a similar thin calcareous turbidite at Site 717 (475 mbsf).

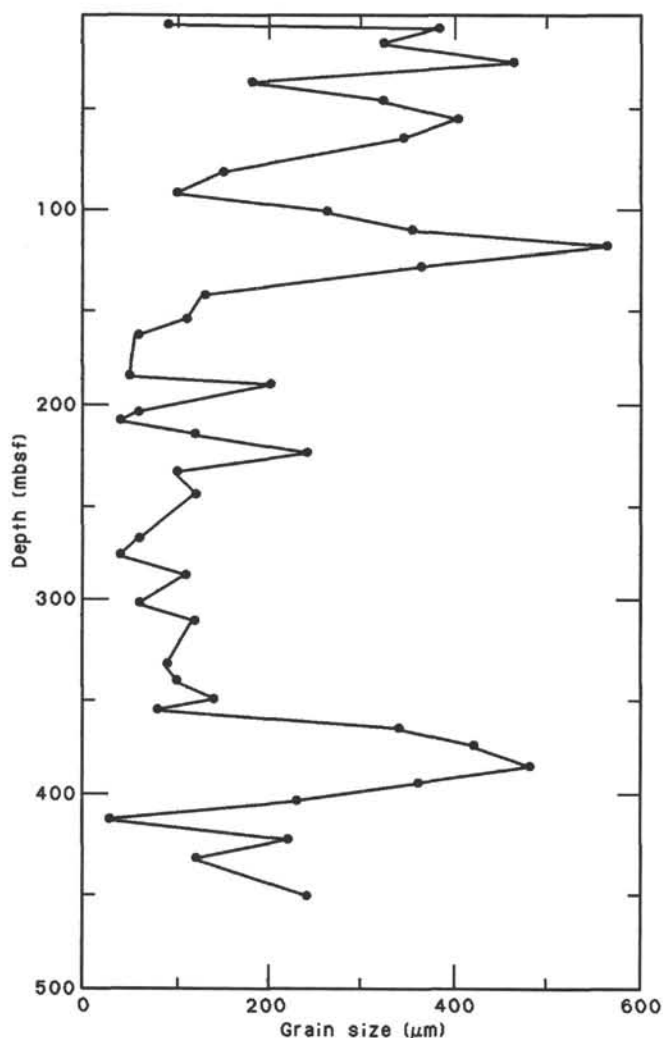


Figure 6. Graph of maximum grain size vs. depth, Site 719.

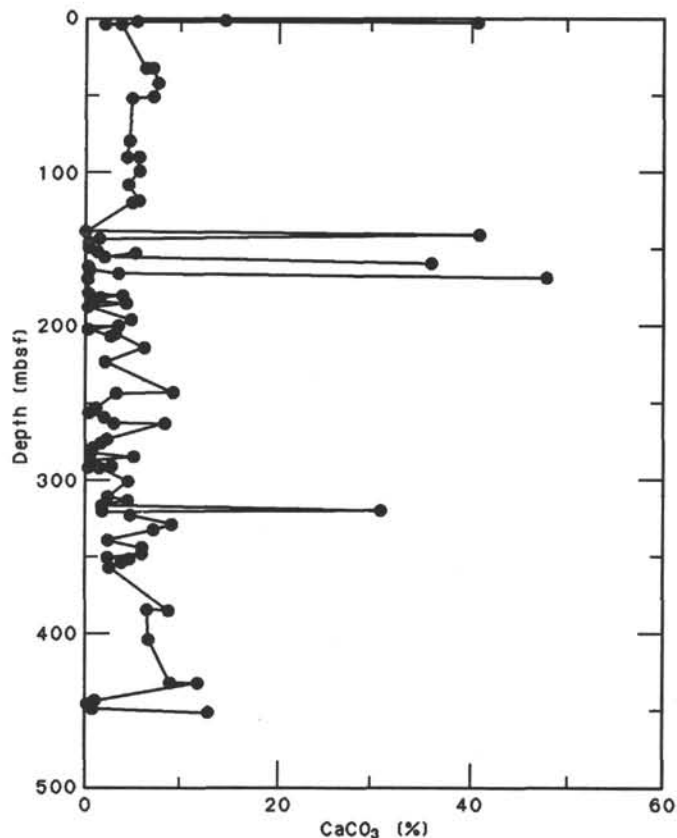


Figure 7. Graph of carbonate content vs. depth, Site 719.

Pyrite Occurrence

Pyrite occurs most commonly as scattered concretions or nodules, 6–20 mm in length, in gray to very dark-gray and black clays; however, it also occurs less frequently in greenish or bluish gray clays of Units III and IVB-D (Cores 116-719A-17X to -719A-23X, 116-719A-27X to -719A-29X, and 116-719A-34X to -719A-38X). Vertically oriented tube fillings, which were common at both Sites 717 and 718, are also observed at Site 719 in X-radiographs taken of the very dark-gray clays. The fillings are 1–2 mm in diameter and approximately 5 mm in length. The thin layers or lenses of pyrite-rich and plant debris-rich silt observed at Site 717 appear to be absent here. Pyritized bioclasts (sponge spicules, foraminifers, radiolarians, fine plant debris) scattered or occasionally agglutinated in large (20–40 mm) concretions, are abundant (up to 20%) in the silty facies.

BIOSTRATIGRAPHY

Diatoms

Isolated or sporadic specimens of diatoms were recovered in 11 of the 91 samples processed and examined from 49 cores of this site. They were found in some of the green clays and, less frequently, in calcareous oozes and chalks. Diatoms were sparse in all of the samples due to tremendous dilution by terrigenous or carbonate material. Recovered valves were, however, generally very well preserved and easily identifiable.

Only in the first core (Samples 116-719A-1H-1, 74–76 cm; 116-719A-1H-2, 68–72 cm and 136–138 cm) was the recovered diatom assemblage moderately diverse; up to 29 taxa were encountered. All three samples contain the same assemblage of oceanic planktonic diatoms. The last sample also contains fairly numerous neritic and some freshwater diatoms. Fairly abundant phytoliths also indicate influx of fossils of terrestrial origin.

Only a few diatoms with stratigraphic significance were recovered in the samples from the first core: *Actinocyclus ellipticus*, *Coscinodiscus nodulifer*, *Hemidiscus cuneiformis*, *Nitzschia marina*, and *Thalassiosira oestrupii*. Following Burckle (1972) and Barron (1983), Cenozoic stratigraphic distribution of these diatoms in low latitudes is as follows: *A. ellipticus*, 14 Ma to Recent; *C. nodulifer*, approximately 13.5 Ma to Recent; *H. cuneiformis*, approximately 12.5 Ma to subfossil; *N. marina*, 8 Ma to Recent; *T. oestrupii*, 5 Ma to Recent. *Pseudoeunotia doliolus* was not encountered. The mid-Pleistocene to the latest Miocene species, *Nitzschia reinholdii*, was present here, apparently redeposited, because the calcareous nanofossils in these samples indicate an age younger than 0.65 Ma, which is the last occurrence of *N. reinholdii*.

In Sample 116-719A-18X-4, 53–55 cm, isolated and well-preserved specimens of *Stephanopyxis appendiculata* were recovered (stratigraphic range from 2 Ma to early Oligocene).

In all the other samples (Cores 116-719A-21X, -719A-22X, -719A-28X, -719A-29X, -719A-31X, and -719A-36X) diatoms were coated with pyrite. Nevertheless, preservation was very good and identification was possible if a sufficiently large fragment or whole valve was recovered. The most diverse assemblage was recovered from Section 116-719A-31X, CC, which contained several pelagic diatoms, *Actinocyclus divisus* among them. *Actinocyclus divisus* is known in the Indian Ocean from sediments no older than earliest Pliocene.

The deepest sample containing diatoms (116-719A-36X-5, 111–113 cm), also pyritized, yielded much older taxa. *Stephanopyxis antiqua* and *Goniothecium decoratum*, which was undoubtedly redeposited.

Radiolarians

Well-preserved radiolarian assemblages at Site 719 are mostly limited to Core 116-719A-1H, similar to Sites 717 and 718. Samples 116-719A-1H-1, 74–76 cm, -719A-1H-2, 68–72 cm, and -719A-1H-2, 136–138 cm, contain well-preserved abundant assemblages belonging to the *Buccinosphaera invaginata* Zone of Quaternary age (Nigrini, 1971). They are typically represented by a radiolarian fauna of more than 50 taxa, and are markedly similar to the biocoenosis from the modern tropical oceans. The samples may be considered of Holocene age.

The diversified fauna in Sample 116-719A-1H-2, 68–72 cm includes *Acanthosphaera actinota*, *Amphispyris costata*, *Anthocyrtdium ophirensis*, *A. zanguebaricum*, *Acrosphaera spinosa*, *A. murrayana*, *Acanthodesmia vinculata*, *Botryostrobos aquilonaris*, *Botryocyrtdis scutum*, *Buccinosphaera invaginata*, *Centrotobryis gravida*, *Collosphaera tuberosa*, *Carpocanarium papillosum*, *Carpocanarium* sp. D, *Clathrocanium diadema*, *Cornutella profunda*, *Dictyocoryne profunda* (the last includes *Hymeniastrum euclidis*), *D. truncatum*, *Didymocyrtdis tetrathalamus tetrathalamus*, *Druppatractus acquilonius*, *Euchitonia elegans*, *Eucyrtdium accuminatum*, *E. hexagonatum*, *Heliodiscus asteriscus*, *Hexacontium axotrias*, *Hexalanche hystricina*, *Lamprocyclus maritalis*, *Lamprocyrtis nigrinae*, *L. hannai*, *Lithopora bacca*, *Otosphaera polymorpha*, *Peripyramis circumtexta*, *Phormosticoartus corbula*, *Pterocanium praetextum praetextum*, *P. trilobum*, *Pterocorys campanula*, *P. zancleus*, *Siphonospaera polysiphonia*, *Spongaster tetras tetras*, *S. pentas*, *Stylochamydium asteriscus*, *Tetrapyle octacantha*, *Theocorythium trachelium trachelium*, *Theopilium tricostatum*, and several additional species. The Samples 116-719A-1H-1, 74–76 cm and -719A-1H-2, 136–138 cm contain less diversified radiolarian faunas (about half the number of taxa in the fraction > 63 μ m) than the above list due to a slightly increased level of dissolution; they may also be assigned to the *B. invaginata* Zone. Besides the Quaternary species, the Sample 116-719A-1H-2, 136–138 cm contains *Eucyrtdium diaphanes* (Oligocene to early Mi-

ocene) and *Siphostichoartus corona* (middle to late Miocene), indicating redeposition.

Below Core 116-719A-1H, preserved radiolarians are pyritized and found only in the following samples: Samples 116-719A-31X-3, 113–115 cm, -719A-31X, CC, and -719A-38X-5, 78–80 cm. Among these are many Liosphaerids and Actinommids. One specimen each of *Anthocyrtdium ehrenbergi ehrenbergi* and *Lamprocyrtis* sp. were found in Sample 116-719A-38X-5, 78–80 cm. *A. ehrenbergi ehrenbergi* is rare in the early Miocene and common in the late Miocene (Nigrini and Moore, 1979). It is tentatively concluded that the sample is of Miocene age pending detailed shore-based analysis of the Liosphaerids and Actinommids with scanning electron microscopy (as transmission light microscopy is generally not definitive for pyritized radiolarians). The remainder of the samples with pyritized radiolarians did not yield any useful information concerning age assignment.

Holocene productivity of Site 719 must be high, based on morphology of several radiolarian species, which agrees with the result from Site 718. For example, skeletons of *D. profunda* have well-developed patagium, an auxiliary spongy skeletal meshwork, which is known to occur in highly productive geographical areas such as the Panama Basin.

Silicoflagellates

Silicoflagellates are almost completely lacking in the 110 samples examined from this site. Only Sample 116-719A-1H-2, 136–138 cm contains several specimens of *Dictyocha messanensis messanensis*, a subspecies commonly found in the modern tropical oceans.

Foraminifers

Site 719 yielded fewer foraminifers than the previous Leg 116 Sites, and consequently provided less biostratigraphic information than the previous sites.

A Holocene age was recognized in Samples 116-719A-1H-1, 120–122 cm and -719A-1H-2, 69–71 cm by the presence of *Bolliella adamsi*.

A Pleistocene age was documented downward to Core 116-719A-16X, based on the occurrence of *Globorotalia truncatulinoides* in Section 116-719A-14X, CC and Sample 116-719A-16X-4, 120–128 cm.

From Core 116-719A-17X down to Core 116-719A-20X, *Sphaeroidinella dehiscentis* persistently occurs but with no other index species. Therefore, the age of these cores can be constrained only to the early Pliocene-Pleistocene interval.

From Core 116-719A-22X downhole *Sphaeroidinellopsis seminulina* enters in the foraminiferal record. Its range, which is extended from late Miocene to early Pliocene, overlaps that of *Sphaeroidinella dehiscentis* in the early Pliocene. However, the two species have not been found associated at any level of this site. Therefore, a late Miocene age assignment is considered most reasonable.

Aside from the scanty planktonic record, the occurrence of the benthic foraminifer *Hyalinea balthica* in Samples 116-719A-16X-4, 120–128 cm, -719A-31X-3, 113–115 cm, and -719A-37X-5, 87–89 cm should be noted. These samples are from biogenic turbidites which, according to their foraminiferal content, are considered to be of shelf-slope provenance. The presence of *H. balthica* is consistent with such an assemblage. Taking into account the most recent literature concerning the distribution of this species, the lowest occurrence of *H. balthica* is documented at Zone N21 (late Pliocene) in Eureka core material from the Gulf of Mexico (van Morkhoven, et al., 1986) However, according to Bandy (1968, cited in Boltovskoy, 1977) *H. balthica* has been found even in Miocene strata in the Philippine Islands. If the correlation with the most recent biostratigraphic scales can

be confirmed, then the occurrence of *H. balthica* in the above-mentioned samples of Site 719 is consistent with calcareous nannofossil stratigraphy.

Calcareous Nannofossils

The calcareous nannofossil record at Site 719 is, in most respects, very similar to Site 717 and, to a lesser degree, to Site 718. The most significant difference is that the various biohorizons are more closely spaced at Site 719 than at Site 717, which reflects a lower sedimentation rate. Nannofossils appear to be more abundant at Site 719; however, this may be an incorrect surmise, an expression of cumulative experience in recognizing promising fossiliferous horizons among the generally unfavorable lithologies of the numerous turbidites. As at Sites 717 and 718, the zonal designation of Okada and Bukry (1980) is used, and the numerical chronology is based on the Berggren et al. (1985) compilation.

Sample 116-719A-1H-1, 71–73 cm is the only one that yielded the late Pleistocene marker *Emiliana huxleyi*. This level is, therefore, clearly late Pleistocene (Zone CN15), i.e., younger than 0.28 Ma. The inconsistent occurrence of *Emiliana huxleyi* at the top of each of the three sites may indicate that this ubiquitous late Pleistocene-Holocene species has been dissolved from the assemblages in which it really should be present. Apparently this species is more susceptible to dissolution than other members of the assemblage. Zone CN14b is identified from this level to the next lower datum, which is the highest occurrence of *Pseudoemiliana lacunosa* in Section 116-719A-4X, CC, from which level down this second marker species is present consistently although usually in low abundance. The age of this datum is 0.47 Ma and it marks the top of Zone CN14a.

In Sample 116-719A-17X-4, 40–42 cm, small species of *Gephyrocapsa* dominate to the virtual exclusion of large species of *Gephyrocapsa*. This and the absence of *Helicosphaera sellii* and of *Calcidiscus tropicus* identifies this level as belonging to the small *Gephyrocapsa* acme interval, which extends from approximately 0.93 to 1.27 Ma and is roughly equivalent to Zone CN13b. This same zone was identified in the next lower sample, 116-719A-17X-5, 87–89 cm, but the next lower sample below, at 116-719A-18X-1, 40–42 cm, yielded an assemblage including *Discoaster brouweri*. Late Pliocene assemblages continue downward to 116-719A-22X-CC, except for the early to mid-Pliocene assemblage at 116-719A-19X, CC, which probably corresponds to very similar displaced assemblages at 116-717C-35X, CC and 116-718-13X-2, 126–128 cm.

The next lower datum is the highest occurrence of *Sphenolithus abies* and of *Reticulofenestra pseudumbilica*, placed at Core 116-719A-22X, CC, below which level both of these species are present consistently and in appropriate proportion in the assemblage. Both also are present, but in disproportionately small numbers, in assemblages above this level, which is to be expected of these two durable species. The age of this datum is 3.5 Ma and it marks the mid-Pliocene. The interval immediately above this datum is assigned to Zone CN12a/b. Immediately below the datum is Zone CN 11, which extends to Sample 116-719A-29X-2, 99–101 cm, the highest occurrence of *Ceratolithus armatus*. The lowest occurrence of the latter is in Sample 116-719A-30X-4, 106–108 cm, the interval being assigned to Zone CN10b, with an age of 5.3 Ma at its base. Zone CN10a extends from this level to the highest occurrence of *Discoaster quinqueramus* in Sample 116-719A-31X-3, 113–115 cm, which is here taken to correspond to the Miocene/Pliocene boundary and has been assigned an age of 5.6 Ma. Zone CN9 extends from this level to the bottom of the cored interval, although one additional datum, the lowest occurrence of *Amaurolithus amplifucus* in Sample 116-719A-43X-1, 16–18 cm can be recognized. This last datum has an age of 5.9 Ma.

The succession of biohorizons at the three sites is remarkably similar, given the limitations of extremely poor fossil recovery. Dilution by massive detrital sedimentation, redeposition by turbidites, and deposition below the regional CCD, all probably work against preservation of calcareous fossils. It should come as no surprise that paleontological correlation and lithological correlation correspond very closely, as is to be expected on a distal fan. The chronological framework established by the above can be used with confidence for further studies.

Sediment Accumulation Rate

The depths and ages of the various biohorizons (datum levels) for Site 719 are given on Table 2. A graphic presentation of the data is given in Figure 8 as a sediment accumulation rate curve, along with similar curves for Sites 717 and 718 for comparison. The sediment accumulation rate was quite high during the late Pleistocene–higher than at Site 718 but less than at Site 717. All three curves show a sharp reduction in sediment accumulation from about 1 Ma down to about 2 Ma, which is actually a hiatus, a period of little or no sediment accumulation during most of the first half of the Pleistocene. From the Pliocene/Pleistocene boundary downward, sedimentation rate increases progressively and, seemingly, very sharply in the latest Miocene. However, not too much faith should be placed in the details of any of the three curves because redeposition and poor fossil recovery combine to render biostratigraphic control somewhat unreliable.

ORGANIC GEOCHEMISTRY

The organic geochemical program at Site 719 consisted of measurements of hydrocarbon gases, organic carbon, and Rock-Eval pyrolysis as at the previous sites. This work is thus an extension of that described in "Organic Geochemistry" sections of the Site 717 and 718 chapters.

Hydrocarbons

Vacutainer Gases

Although Site 719 is located only 3.2 km south of Site 717, no measureable Vacutainer gases were present at any depth, which is in contrast to the routine recovery of gases from Site 717. The difference in average organic carbon concentration between the two sites is not great (0.96% at Site 717, 0.80% at Site 719), but isolated high values (up to 7.5%) were observed at Site 717. This may account for the different results obtained.

Extracted Gases

Analyses of headspace gas samples are given in Table 3 and Figure 9. Methane (C_1) concentrations range from 0 to 6500 ppm, reaching broad maxima in the middle of lithologic Unit II, throughout Unit IV, and in the lower part of Unit V. Values in Unit III and at the top of Unit V are significantly lower.

Table 2. Depths and ages of Neogene nannofossil biohorizons at Site 719.

Depth (mbsf)	Age (m.y.)
37.7	0.47
153.1	0.93
168.5	2.2
168.8	2.47
203.7	3.5
277.3	5.3
285.3	5.6
385.7	5.9

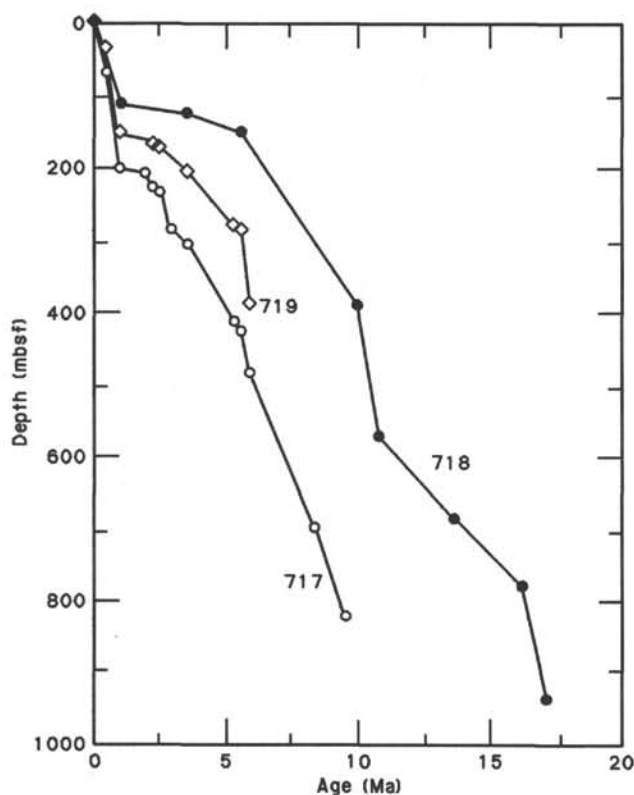


Figure 8. Sediment accumulation rates at Sites 717, 718, and 719.

Methane/ethane (C_1/C_2) ratios are plotted with depth in Figure 9 and closely mirror the absolute concentrations of C_1 . The C_2 values remain below 5 ppm and show no increase with depth, indicating immature and nonmarine organic matter.

Carbon

Physical property and squeeze-cake samples were used for determinations of organic carbon. Table 4 and Figure 9 show the organic carbon concentration with depth. As a whole, organic carbon contents range from 0.13% to 2.17% (avg. 0.8%) and are less than that at Site 717. In lithologic Units II and V, organic carbon contents are less than in other units. This observation is similar to that at Site 717, except in Unit V, which has slightly lower organic carbon values than those in Unit V at Site 717. The concentrations of organic carbon and C_1 do not change in parallel and in some parts seem to be directly opposed. This is presumed to be due to differences in bacterial activity.

Rock-Eval

The squeeze-cake samples have been analyzed by Rock-Eval pyrolysis. Rock-Eval results are given in Table 4 for 15 samples from Site 719. Hydrogen Index (HI) and Oxygen Index (OI) values are plotted on a van Kreveln-like diagram (Fig. 10). The HI and OI values range from 0 to 74 and from 78 to 554, respectively, and fall in the range for Type III Kerogens derived from terrestrial wood. T_{max} values range from 231 to 435°C, which indicates that organic matter is immature with regard to petroleum generation as was found at Site 717. These results for Sites 717, 718, and 719 suggest that a major part of the organic material in the sediment encountered on Leg 116 was transported from the Ganges-Brahmaputra River and delta plain.

INORGANIC GEOCHEMISTRY

Site 719 is located about 3.2 km south of Site 717. At Site 719 one should expect about the same lithology with some thin-

Table 3. Headspace gases from Hole 719A.

Core-Section (Interval, cm)	Depth (mbsf)	C_1 (ppm)	C_2 (ppm)	C_1/C_2
Hole 719A				
1H-2, 0-5	1.50	3.8	1.0	3.8
2X-1, 118-123	5.38	7.1	1.6	4.4
4X-1, 0-5	23.20	1361.0	1.2	1134.0
5X-1, 0-5	32.70	1890.0	1.6	1181.0
6X-1, 0-5	42.20	4271.0	0.6	7228.0
7X-1, 0-5	51.70	5494.0	1.7	2616.0
8X-1, 0-5	61.20	5982.0	1.0	5982.0
11X-1, 0-5	89.70	5521.0	1.4	3943.0
12X-1, 0-5	99.20	6525.0	3.7	1764.0
13X-1, 0-5	108.70	4302.0	2.6	1655.0
15X-1, 0-5	127.70	2140.0	1.5	1427.0
16X-5, 0-5	143.20	4705.0	1.6	2941.0
17X-5, 0-5	152.70	1641.0	1.1	1492.0
18X-1, 0-5	156.20	549.0	2.2	250.0
19X-3, 0-5	168.70	205.0	3.0	68.0
20X-5, 0-5	181.20	74.0	2.8	26.0
21X-2, 0-5	186.20	15.1	3.8	4.0
22X-5, 0-5	200.20	2016.0	1.4	1440.0
23X-2, 0-5	205.20	3097.0	2.6	1191.0
24X-1, 0-5	213.20	2878.0	2.8	1028.0
25X-1, 0-5	222.70	4592.0	1.3	3532.0
26X-1, 0-5	232.20	148.0	1.0	148.0
27X-2, 0-5	243.20	4683.0	2.0	2341.0
28X-3, 0-5	254.20	4923.0	1.9	2591.0
29X-3, 0-5	263.70	4381.0	0.6	7301.0
30X-5, 0-5	276.20	5029.0	1.9	2647.0
31X-5, 0-5	285.70	5312.0	2.4	2213.0
32X-3, 0-5	292.20	4785.0	1.7	2815.0
33X-2, 65-70	300.85	4782.0	1.6	2989.0
34X-5, 0-5	314.20	5056.0	2.1	2408.0
35X-2, 0-5	319.20	4673.0	4.7	994.0
36X-6, 0-5	334.70	3244.0	0.7	4634.0
37X-5, 0-5	342.70	4413.0	1.7	2596.0
38X-5, 0-5	352.20	4571.0	2.8	1632.0
39X-1, 0-5	355.70	3531.0	1.7	2077.0
41X-1, 0-5	374.70	98.0	1.1	89.0
42X-1, 0-5	384.20	516.0	1.0	516.0
43X-1, 0-5	393.70	1486.0	2.4	619.0
44X-1, 0-5	403.20	3510.0	1.7	2065.0
46X-1, 0-5	422.20	4730.0	2.5	1900.0
47X-1, 65-70	432.35	5063.0	4.6	1101.0
48X-5, 0-5	447.20	4818.0	3.1	1554.0
49X-1, 56-61	451.26	5003.0	4.9	102.0

ning of layers due to the deformation as seen from the single channel seismic line of R/V CONRAD Cruise 2706. The chemistry of interstitial waters (IW) at Site 719 should also be comparable with that of Site 717.

Sampling and Methods

Fluid sampling was carried out mostly at depth intervals of about 30 m. One successful *in-situ* pore-water sampling offered the opportunity to check possible large deviations in compositions due to the sampling procedure and the squeezing effects. As already noticed at the two previous sites, the interstitial water (IW) recovery was poor in the clay-rich layers (8-10 cm³) and larger in the silty layers (15-70 cm³). The analytical methods and procedures employed for IW are the same as those for Site 717 and are described in the "Explanatory Notes" chapter.

Results

Chloride (Cl) and Sodium plus Potassium (Na + K)

The concentration of Cl as well as Na + K show large variations ranging over 10% (Fig. 11). The overall variations of Cl vs. depth are similar to that of Site 717. The extremes are larger than at Site 717, and there is a slight depth difference in their location (about 40-50 m between Sites 719 and 717) at depths greater than 125 mbsf, the depths at Site 719 being shallower.

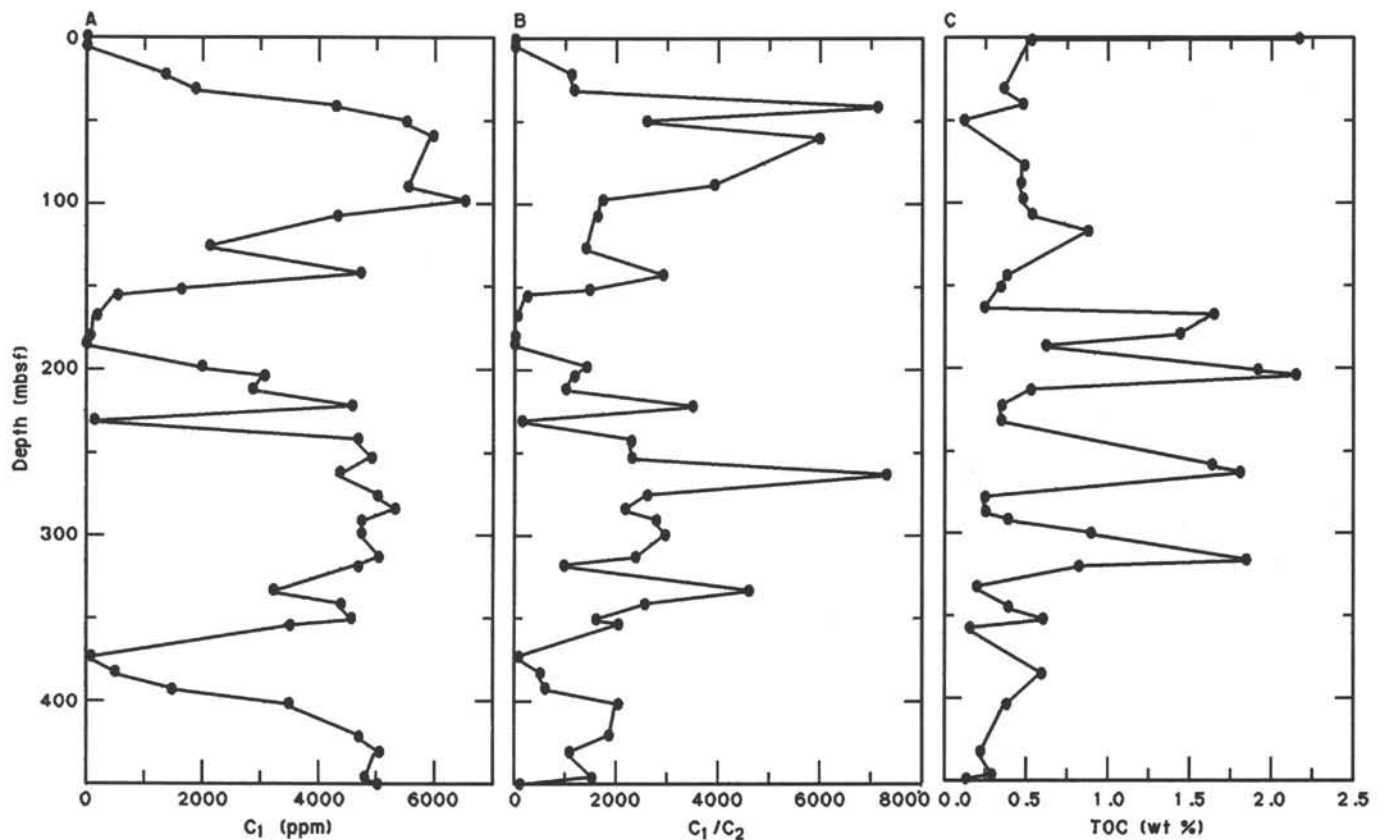


Figure 9. Concentrations with depth of (A) C_1 , (B) C_1/C_2 ratios in gases extracted from sediments by the headspace procedure, and (C) organic carbon, from Hole 719A.

Na + K variations in the upper 125 mbsf are quite different from those found at Site 717. The lower values obtained at Site 719 may be due to more extensive K and Na uptake in clay minerals. At depths larger than 125 mbsf, one finds the same pattern of Na + K vs. depth variations as at Site 717. As for the extremes of Cl, extremes of Na + K are larger than at Site 717. Also the depth profile seems to be shifted 40–50 m upward as compared to 717 at depths greater than 125 mbsf.

The (Na + K)/Cl ratios decrease in clay-rich layers and are larger in silt, although always lower than in seawater. The general trend is toward decrease of (Na + K)/Cl with increasing depth. This corresponds to the effect of clay diagenesis with uptake of K and Na.

Calcium (Ca)

The Ca vs. depth profile for Hole 719A (Fig. 11) has the same features as that of Site 717. The general trend is toward decrease of Ca in the upper 150 mbsf, probably due to deposition of carbonate, and gradual increase of Ca at lower depths. Some shifts are found in the depths of characteristic features:

1. A first minimum is found at 20 mbsf at both locations;
2. A small maximum followed by a sharp minimum are shifted up 30 m compared to Site 717;
3. At the last IW sample (about 455 mbsf) shows a decrease of Ca which might be compared to that found at 505 mbsf at Site 717.

However, at Site 719 this last variation corresponds to a silt layer in lithologic Unit V and is located under a clay-rich layer, whereas at Site 717 it is located in a silt layer interbedded in the

clays of lithologic Unit IVC. Because this feature of Ca seems to be quite characteristic of what is otherwise a quite smooth Ca vs. depth curve, its location is not in agreement with the lithostratigraphic observations.

Magnesium (Mg)

The general features of the Mg vs. depth curve (Fig. 11) compare well with those of Site 717. However, the decrease of Mg is more accentuated at Site 719. This may correspond to a more extensive clay diagenesis and is in agreement with the larger variations of (Na + K)/Cl.

The depth profile of Mg is the same as at Site 717 in the first 50 mbsf. Between 50 and 125 mbsf the two sites give quite different results as Mg presents a small maximum and not a minimum as in Hole 717C. Such a maximum may be related to the Mg-NH₄ exchange in clay minerals and/or inhibition of Mg deposition with dolomite as suggested at Site 717. This suggests future careful studies of clay mineralogy compositions and fine-grained carbonates to decipher this early difference in diagenesis. Below 140 mbsf the variations of Mg with depth are nearly linear with local variations due to lithology (clay vs. silt). We can estimate $dMg/dz = -59 \text{ mmol}/(\text{L} \times \text{km})$ (dashed line, Fig. 11), which is much larger than at Site 717 where $dMg/dz = -28 \text{ mmol}/(\text{L} \times \text{km})$. This should correspond to more extensive uptake of Mg by clay minerals as well as deposition with carbonates.

Alkalinity (Alk) and Calcium Carbonate Saturation

As for the elements discussed above, the Alk values from Hole 719A (Fig. 11) are comparable with those at Site 717. There is a shift in the characteristic high values found at 140–

Table 4. Rock-Eval data summary from Hole 719A.

Core Section (Interval, cm)	Depth (mbsf)	T _{max}	S ₁	S ₂	S ₃	OC	HI	OI
Hole 719A								
1H-2, 145-150	2.95	385	0.19	0.55	3.74	2.17	25	172
2X-1, 46-50	4.66					0.54		
5X-1, 43-53	33.13	344	0.05	0.02	1.21	0.37	5	327
6X-1, 47-50	42.67					0.49		
7X-1, 53-58	52.23	231	0.03	0.00	0.63	0.12	0	525
10X-CC (0-4)	80.20					0.50		
11X-1, 110-120	90.80	303	0.06	0.06	2.89	0.48	19	602
12X-1, 74-76	99.94					0.49		
13X-1, 36-40	109.06					0.55		
14X-1, 140-150	119.60	350	0.11	0.25	3.57	0.89	28	401
16X-6, 138-142	146.08					0.39		
17X-4, 140-150	152.60	316	0.05	0.08	1.94	0.35	23	554
18X-6, 90-94	164.60					0.25		
19X-3, 81-85	169.51					1.66		
20X-4, 140-150	181.10	392	0.25	1.07	1.90	1.45	74	131
21X-3, 35-37	188.05					0.63		
22X-6, 91-95	202.61					1.93		
23X-1, 140-150	205.10	389	0.16	0.46	3.78	2.16	21	175
24X-1, 66-70	213.86					0.54		
25X-1, 52-56	223.22					0.36		
26X-1, 77-87	232.97	308	0.05	0.07	0.88	0.36	19	244
28X-6, 60-64	259.30					1.65		
29X-2, 140-150	263.60	399	0.13	0.58	3.04	1.82	32	167
30X-6, 103-107	278.73					0.26		
31X-6, 23-27	287.43					0.26		
32X-2, 140-150	292.10	435	0.06	0.16	0.31	0.40	40	78
33X-2, 59-62	300.79					0.91		
34X-6, 85-89	316.55					1.86		
35X-2, 140-150	320.60	361	0.08	0.35	0.83	0.84	42	99
36X-4, 90-94	332.60					0.20		
37X-6, 39-43	344.59					0.40		
38X-4, 140-150	352.10	353	0.06	0.26	1.77	0.62	42	274
39X-CC (17-21)	357.22					0.16		
42X-1, 93-103	385.13	249	0.01	0.00	0.60	0.61	0	98
44X-1, 37-41	403.57					0.39		
47X-1, 70-75	432.40	272	0.02	0.01	1.00	0.22		
48X-4, 6-10	445.76					0.29		
49X-1, 61-66	451.31					0.13		

155 mbsf at Site 719 and at 155-185 mbsf at Site 717. This is a shift similar to those for Ca and Mg profiles in the same depth range.

The variations of the Ion Activity Product (IAP) of CaCO₃ (Fig. 12) are less scattered than at Site 717. Also, there is no value above the calcite solubility product. The overall IAP values are close to saturation with 3%-Mg calcite. The comparison of Ca, Alk, and IAP depth profiles suggests there may be carbonate deposition in the upper 300 mbsf.

Sulfate (SO₄)

The depth profile of SO₄ from Hole 719A (Fig. 13) shows the same features and the same corresponding SO₄ values as that of Site 717. After a sharp decrease in the upper 30 mbsf, a similar secondary maximum was found near 60-100 mbsf which correlates with that of Ca. Below 125 mbsf the SO₄ values are nearly constant, with local variations which may be due to the oxidation of pyrite following coring operations. Below 125 mbsf the SO₄ values are about 1 mmol/L, which is 1.5 mmol/L less than at Site 717. This difference reflects slightly more reducing conditions and more extensive microbial degradation of organic matter at Site 719.

Silica (SiO₂)

As shown in Figure 13, the SiO₂ values decrease in the upper 30 mbsf of Hole 719A after the classical maximum near the seafloor. There is a maximum of SiO₂ near 160 mbsf which corre-

lates with that of Alk. It is probably due to dissolution of siliceous tests.

Phosphate (PO₄) and Ammonia (NH₄)

In the upper 200 mbsf the values of PO₄ and NH₄ are high and correspond to extensive degradation of organic matter. Maximum values of PO₄ and NH₄ are obtained near 100 mbsf, slightly above those of Alk and SiO₂ (150-160 mbsf). Below 200 mbsf PO₄ is low (2000 mmol/L) and NH₄ is quite variable, in the range 0.9-1.5 mmol/L.

In-Situ Sample

Cl, Ca, Alk, IAP (CaCO₃), NH₄, and PO₄ values are higher in the *in-situ* sample than in the IW sampled 1.5 to 9.5 m below it (the uncertainty in depth is due to poor core recovery), whereas Na + K, SO₄, and SiO₂ values are lower. Differences are about 10% for Ca and Alk, 5% for Mg, and less than 1% for Cl. However, due to the large variations in compositions with depth observed in the depth range of the *in-situ* sampling, such differences should be expected. Thus we can consider that the sampling of IW and the *in-situ* pore water give concordant results.

Discussion

The results obtained at Site 719 are quite clear and their preliminary interpretation supplements those acquired at Site 717. The suggested diagenetic effects (carbonate deposition, dissolved

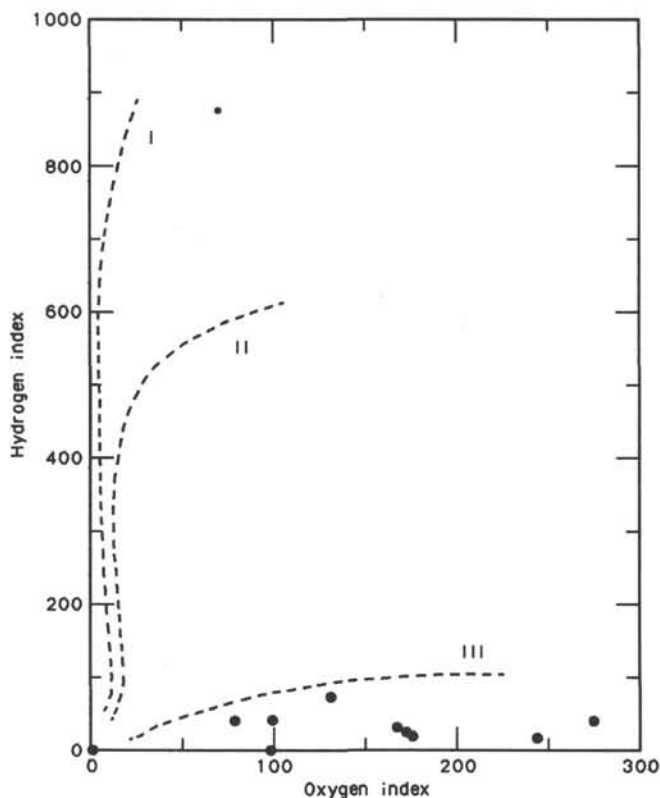


Figure 10. Hydrogen and Oxygen Indexes obtained from Rock-Eval pyrolysis of sediments from Hole 719A and plotted on a van Krevelen-like diagram.

ions-clay exchanges) will be studied in detail in shore-based laboratories for further confirmation.

As expected, the concentrations of the dissolved elements in the IW samples are nearly the same in equivalent sedimentary layers sampled some 3.2 km apart. This indicates the role of lithological control as well as diagenetic control on the concentration of dissolved elements in IW. Hence the differences, such as that found for Mg, which seem to be more affected by diagenesis at Site 719, are also significant and should be investigated further.

It is worth noticing that the Ca profiles are similar in the respective depth ranges of 320–455 and 370–505 mbsf at Sites 719 and 717. This is not in complete agreement with the preliminary depth assignment of Lithologic Units IVC and V between Sites 717 and 719. It is, however, not so contradictory to the assigned ages of the sediments at the same depths.

Conclusions

The depth profiles of the major dissolved elements from interstitial waters collected at Site 719 are very similar to those obtained at Site 717, with some shifts in depths. Hence, most of the conclusions given for Site 717 can be applied at Site 719:

1. There is a differentiation in values due to variation in lithology (i.e., clay vs. silt);
2. The effect of clay diagenesis on Cl and Na + K decreases in the clay-rich layers and increases in the silt layers;
3. There is an exchange of Ca and Mg in clays; and,
4. Deposition of carbonates (probably Mg-rich) occurs at least in the upper 300 mbsf.

On the basis of (Na + K)/Cl, Mg, Alk, and nutrients, the effects of clay diagenesis and microbial degradation of organic matter are more extensive at Site 719 than at Site 717.

PALEOMAGNETISM

Remanent Magnetic Intensity

The natural remanent magnetization (NRM) of the archive half of each core from Hole 719A was measured at 5-cm intervals. Although the range of NRM intensities was similar to that observed at Sites 717 and 718, the mean intensity, 18.2 mA/m, is considerably smaller. As a result, at this site only eight sections (i.e., 7%) were too strongly magnetized to be measured with the cryogenic magnetometer. The histogram of the NRM intensities (Fig. 14) shows a skewed distribution similar to that observed at Site 718. All sections were demagnetized using an alternating field of 9 mT, and their remanence was remeasured. After alternating field (AF) demagnetization, all sections could be measured with the cryogenic magnetometer. The mean intensity of the demagnetized cores, 3.7 mA/m, was much smaller than that observed at Site 718 but very similar to the value obtained at Site 717 (2.5 mA/m).

The remanent intensities after demagnetization were used to calculate the logarithmic mean values for the lithologic Units II through V (See "Lithostratigraphy" section). These values are compared with those from Sites 717 and 718 in Table 5. Because of their proximity and the fact that both sites were located on the same fault block, it was anticipated that the values for Sites 717 and 719 would be very similar. In the case of Units II and V, however, the values were significantly lower at Site 719, although the recovery was poor for both units and the values obtained may not be representative. Unit III, on the other hand, appeared to be much more strongly magnetized at Site 719 than at Site 717 and was closer to Site 718 in intensity (Table 5). Of the various units, only the mean intensities for Unit IV at Sites 717 and 719 were comparable. The intensity of Unit IVA agreed remarkably well, though for Site 719 the mean value was based on only 37 measurements. Although somewhat more strongly magnetized at Site 719 than at Site 717, the mean intensity of the lower part of Unit IV was nevertheless much closer to that of the same unit at Site 717 than at Site 718.

With the limitations imposed by the poor recovery, it was difficult to directly compare many of the units from site to site. Unit III, however, was an exception as there was good recovery throughout this depth interval. On the basis of the values at each of the three sites, it appeared that a significant part (about 60–70 m) of the upper, more weakly magnetized portion of this unit is absent at Sites 718 and 719.

Comparison of the remanent intensities with the volume magnetic susceptibility measurements yielded several relatively good correlations. For example, between depths 140 and 205 mbsf both parameters showed large intensity values suggesting that ferromagnetic grains were responsible for both signals. As noted at previous sites, however, there were several zones of high-intensity remanence (e.g., 40–90 mbsf) where the susceptibility was low or moderate and vice versa. Correlations of the remanent intensity patterns between Site 717 and 719 were attempted but found to be too uncertain to be used without further constraints.

Magnetic Inclination

In a similar manner to both Sites 717 and 718, the NRM magnetic inclinations at Site 719 were biased toward large negative inclinations reflecting the coherent vertical overprint that has been ascribed to the drill pipe or core barrel. In the case of Site 719, however, the negative bias appeared to have been almost completely removed by the demagnetization process. In Figure 15, histograms of inclination values before and after AF demagnetization indicate a change in the peak value from about -45° to about -5° . The positive and negative values of inclination were analyzed separately to determine the amplitude of any residual inclination bias in the demagnetized values. The

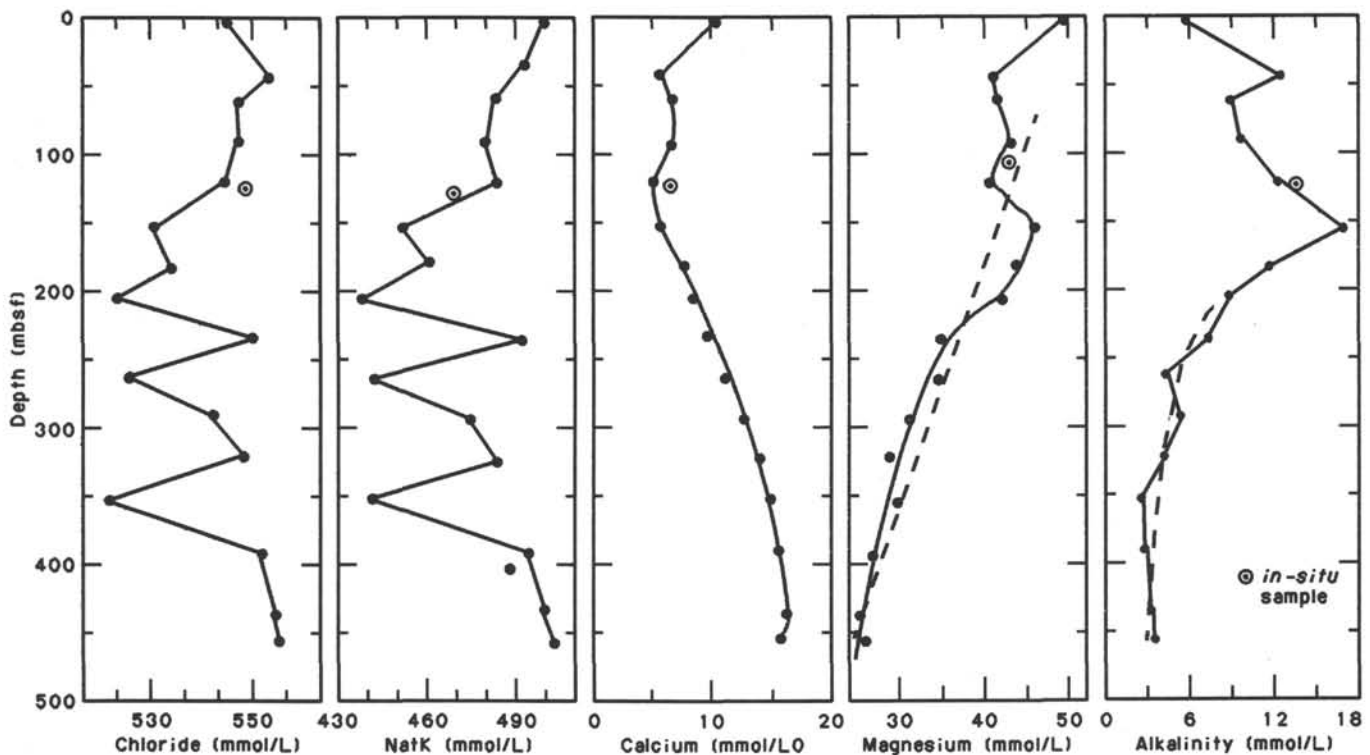


Figure 11. Plot of Cl, Na + K, Ca, Mg, and alkalinity concentration vs. depth for Hole 719A. For Mg the dashed line shows estimated linear trend. For alkalinity the dashed line shows trend of values from below 200 mbsf.

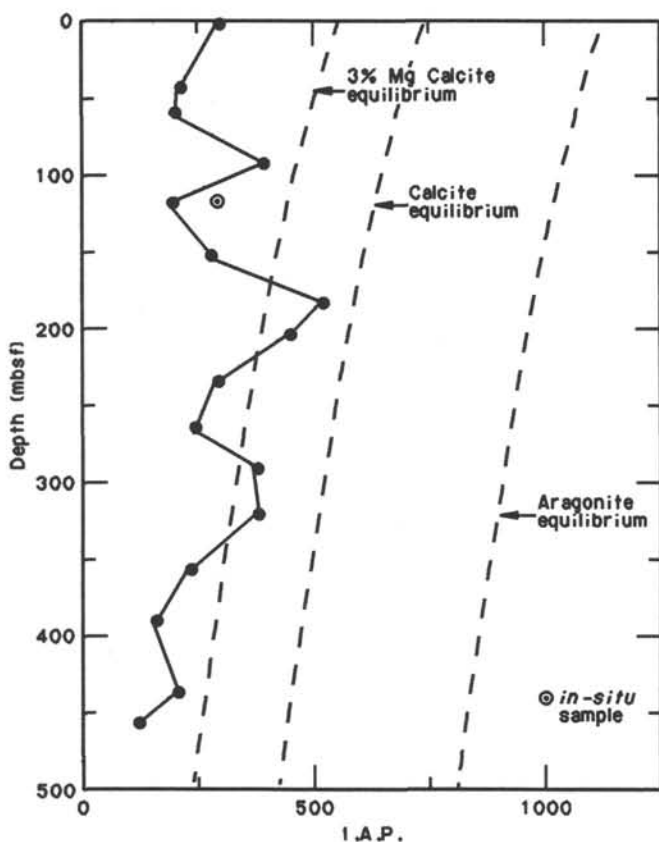


Figure 12. Plot of calcium carbonate ion activity product (I.A.P.) vs. depth for Hole 719A. The 3%-Mg calcite, calcite, and aragonite equilibrium curves have been corrected for pressure and temperature effects at *in-situ* conditions.

mean values of positive and negative inclinations obtained were 24.5° and -20.1° , respectively, and imply a small positive bias of about 2° . In view of the large standard deviations of these mean values (about 20°) and the obvious negative nature of the overprint, the $+2^\circ$ bias was considered insignificant. However, though it may be assumed that the negative overprint has been effectively removed from the core as a whole, it must be remembered that individual cores were affected by the overprint to a greater or lesser degree. The overall mean inclination was approximately 22° , somewhat steeper than expected at this site for material less than 6 Ma. Adjustments to the observed value of magnetic inclination, based upon the dip of the sedimentary layers and the influence of *far-sided* long-term nondipole effects, are discussed in the Site 718 chapter. As rocks older than 6 Ma were not sampled at Site 719, the maximum expected inclination for an axial dipole is about 6° , taking into account plate tectonic drift. It was difficult to account for the observed value solely in terms of the factors mentioned above; it appears likely that there are other effects, possibly related to the bisecting of the core material by the drilling procedure, that also contribute systematically to this disparity.

A study of variations in inclination with depth was carried out by determining the mean inclination for each successive group of 800 measurements. Core recovery at this site was so poor in the upper 140 mbsf that it is meaningless to calculate mean inclinations based upon uniform depth intervals. Not surprisingly, the analysis failed to show any appreciable inclination increase, as only a modest increase was expected and the uncertainty in each mean value was large.

The relatively poor recovery and the use of the XCB for Cores 116-719A-2X through -719A-49X made any attempt at magnetostratigraphy fruitless. A somewhat cursory look at the magnetic polarity based upon the inclination values yielded two zones where the field seems to be dominantly normal or dominantly reverse. The first was between 140 and 160 mbsf where the core material is normally magnetized, the second was be-

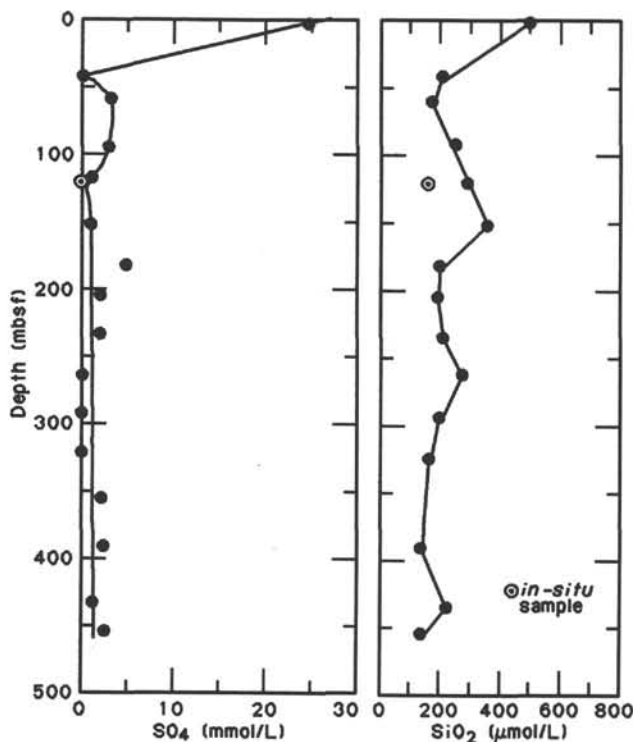


Figure 13. Plots of SO_4 and SiO_2 concentration vs. depth for Hole 719A.

tween 308 and 332 mbsf and indicated reverse magnetization. Comparison of these zones with the biostratigraphic control (see "Biostratigraphy" section) suggested that the first may correspond with the Olduvai normal polarity period (Chron 2), while the second may coincide with the reversed interval between 4.79 and 5.41 Ma (Chron 3r). Such correlations, however, are extremely tentative, as the variations in inclination values are large and the core recovery poor.

Magnetic Declination

A histogram of the magnetic declination values before and after AF demagnetization is shown in Figure 16. The distribution of NRM declination values was fairly flat, reflecting an almost random distribution of values. This is in marked contrast to Site 718 where the values were not randomly distributed but had a major peak near 180° – 200° . Unlike Site 718 where the AF demagnetization reduced the azimuthal bias, in the case of Site 719 the AF values were more highly peaked than the NRM values with a maximum between 60° and 80° suggesting that the overprint in this case may have been due to the demagnetization process itself. If so, then the preferred orientation may have been the result of an anhysteretic remanence produced by the demagnetizing coils in the cryogenic magnetometer. In support of such an interpretation, there is also a peak in the histogram of the AF demagnetized declination values for Site 718 that lies between 80° and 100° .

Magnetic Susceptibility

Volume magnetic susceptibility measurements were made at 5-cm intervals on 1.5-m whole core sections from Hole 719A. In all, 3,427 readings were recorded from these cores. The susceptibility values displayed a similar range to those found in cores from Sites 717 and 718. For Hole 719A cores, the lowest recorded susceptibility was 9.0×10^{-6} cgs, in Core 116-719A-16X, whereas the highest was 5.7×10^{-4} cgs, in Core 116-719A-31X.

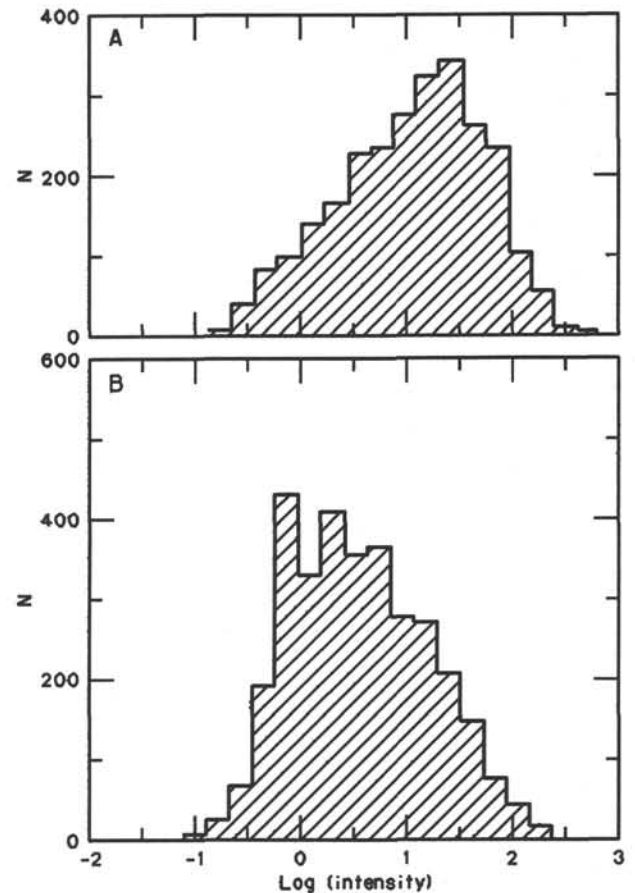


Figure 14. Histogram of logarithmic intensity of magnetic remanence for (A) NRM, and (B) 9-mT AF demagnetization measurements for Hole 719A.

The character of the susceptibility record from Hole 719A cores was also similar to that of Hole 717C cores. Although poor recovery in the silt layers at Site 719 made comparison difficult, the susceptibility values in these layers appeared moderately high and scattered as at Site 717. Better recovery was achieved in the mud layers of Hole 719A. They displayed a relatively low background susceptibility of about 1.0 – 3.5×10^{-5} cgs punctuated by peaks, often in excess of 1.0×10^{-4} cgs, that were well-correlated with dark-gray mud turbidites. These characteristics were also typical of similar mud layers in Hole 717C cores.

Table 5. Logarithmic mean remanent intensity (mA/m) after 9-mT AF demagnetization of sediment units encountered on Leg 116.

Unit	Subunit	Site 717	Site 718	Site 719
II	—	20.1	24.5	13.5
III	—	1.3	6.7	5.0
IV	all	1.2	18.2	2.7
	A	4.5	—	5.0
	B	1.0	—	2.7*
	C	0.6	—	—
V	all	7.4	6.4	3.3
	A	—	6.0	—
	B	—	6.7	—
I-V	—	2.5	7.4	3.7

* includes B thru D

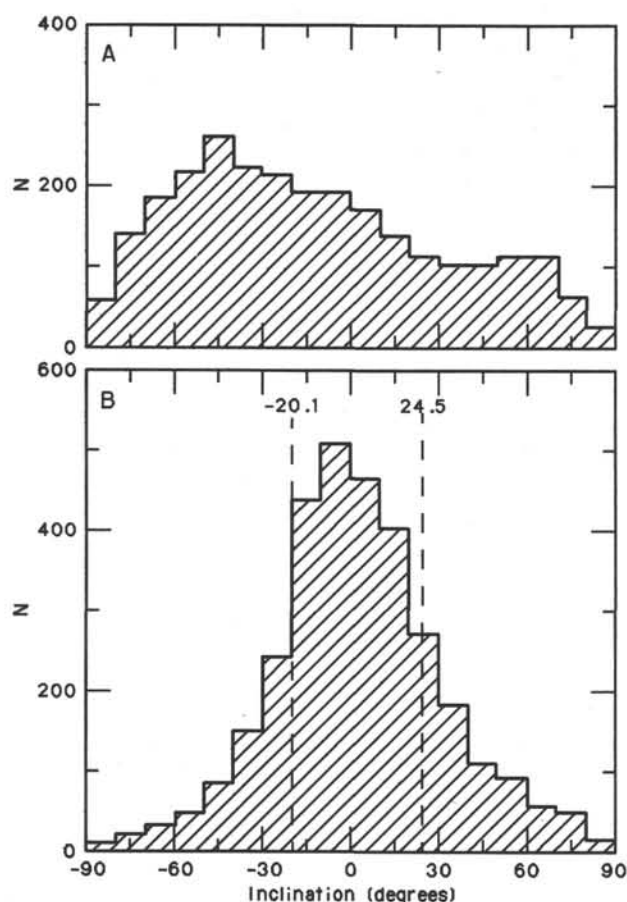


Figure 15. Histogram of magnetic inclinations for (A) NRM, and (B) 9-mT AF demagnetization measurements for Hole 719A. Dashed lines in (B) indicate arithmetic mean values of positive and negative inclinations.

On a large scale, the Hole 719A susceptibility measurements showed a pattern of low and high values similar to those of Hole 717C. Between 140–210 and 250–360 mbsf the recovered sediments gave many large susceptibility spikes (Fig. 17). Additionally, high-amplitude peaks were also measured in the last core of Hole 719A. Each of these three *pulses* of high-susceptibility value corresponded to a section of gray mud, whereas the intervening lower values corresponded to silty sediments. The shallowest susceptibility pulse encompassed Unit III, and the pulse below it, Units IVB–IVD. The high-susceptibility values found in cores taken near the bottom of the hole were mainly from a gray mud layer in Unit V. Given lithologic (see “Lithostratigraphy” section) and biostratigraphic (see “Biostratigraphy” section) constraints, the susceptibility pulses from Hole 719A were correlated with those measured in Hole 717C as shown in Figure 18. The high values between 140–210 and 250–360 mbsf in Hole 719A cores probably correspond to the high values found between 250–320 and 390–480 mbsf in Hole 717C cores. Furthermore, the high-susceptibility values observed in the last cores of Hole 719A may correspond to those measured beginning at 570 mbsf in Hole 717C cores.

If these correlations are valid, they have several interesting implications. Both of the upper susceptibility pulses from Hole 719A were approximately the same width as measured in Hole 717C, yet they were found closer together and shallower in Hole 719A (Fig. 18). This suggests that these particular sedimentary units have remained intact whereas those surrounding them have

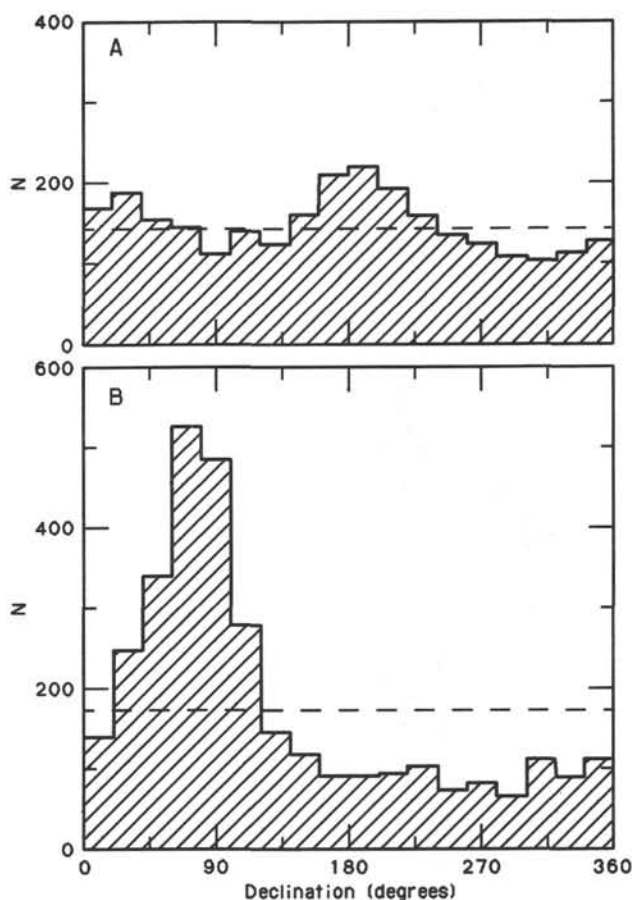


Figure 16. Histogram of magnetic declinations for (A) NRM, and (B) 9-mT AF demagnetization measurements for Hole 719A. Horizontal dashed lines indicate distribution of declinations expected for a random distribution of values.

been either eroded or not deposited. It appears that the less-magnetic upper part of Unit III observed in Hole 717C is not present in Hole 719A, a conclusion that also fits the remanent magnetic intensity data discussed above. Additionally, these results suggest that only about half of Unit IV between 310–400 mbsf, sampled in Hole 717C, is found in Hole 719A. However, the distance between the deeper susceptibility pulses observed in Hole 719A cores were the same as those observed in Hole 717C, suggesting that this section is intact in Hole 719A cores.

Although the correlation of large-scale susceptibility features between Sites 717 and 719 is good, the correlation of fine structure is not obvious. The individual susceptibility peaks, caused by turbidites, could not be traced from one hole to the other with any confidence. A comparison of the upper susceptibility pulses in both holes showed that the susceptibility peaks from Hole 719A were noticeably narrower and decidedly more numerous than those from Hole 717C. Within this portion of the core, four times as many peaks with amplitudes in excess of 1.0×10^{-4} cgs were found in the former as in the latter. The relative narrowness of the Site 719 turbidite layers compared to Site 717 might be expected if Site 719 were located updip from Site 717 due to vertical tectonics. However, the greater number of turbidite layers found in Hole 719A is then unexpected and difficult to explain. One possibility that must be considered is that the correlation between holes made on the basis of the broad-scale susceptibility features was in error. These differences were not found when comparing the second susceptibility peak down-

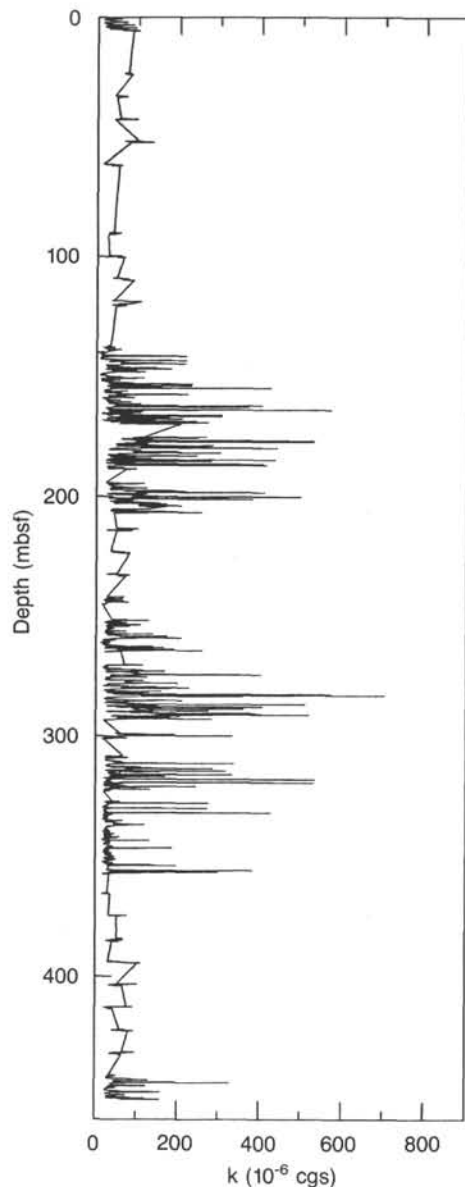


Figure 17. Whole-core volume magnetic susceptibility (k) plotted vs. depth for Hole 719A.

hole. In this section of each hole the susceptibility peaks were of similar width and number. However, in this case as before, it was difficult to make a one-to-one correlation of susceptibility peaks from hole to hole. With more detailed lithologic and age correlations, this task might prove tractable.

PHYSICAL PROPERTIES

Core 116-719A-1H was obtained by the Advanced Piston Core (APC). Cores 116-719A-2X through 116-719A-49X were recovered by the Extended Core Barrel (XCB) operations. Physical properties measured routinely on all cores recovered at Site 719 include GRAPE density and thermal conductivity from full-round core sections, vane shear strength, compressional wave velocity, and index properties from split sections. The methods used are described in the "Explanatory Notes" chapter. Results of physical properties measurements at Site 719 are summarized in Tables 6 to 9.

Index Properties

Index properties determinations included wet-bulk density, water content (related to wet weight), porosity, and grain density (Table 6). The measurements were mainly made on fine-grained deposits because silty to sandy sediments were too disturbed by drilling to determine index properties. The scatter of the data points are attributed to disturbance by drilling, variations in sediment composition, and measurement errors.

Porosity

The porosity of the sea-floor sediments is approximately 80% (Fig. 19). The porosity decreases within the upper 100 m nearly exponentially to a value of 55%. Below that depth the decrease is almost linear with a rate of 2.86% per 100 m. The porosity at the bottom of the hole averages 45%. As previously noted at Sites 717 and 718, the porosity values show a range of scattering, especially in the compositionally more complex lithologic units.

Wet-Bulk Density

Wet-bulk density (Fig. 19) increases from 1.37 g/cm³ at the seafloor to about 1.75 g/cm³ at 100 mbsf with a rate of 0.38 g/cm³ per 100 m. Below this depth, the rate of increase decreases to 0.07 g/cm³ per 100 m. The wet-bulk density at the bottom of the hole averages 2.00 g/cm³.

Water Content

The wet-water content decreases nearly exponentially from a sea-floor value of about 60% to about 30% at 100 mbsf (Fig. 19). Below that depth, the rate of decrease is nearly linear with a rate of 1.43% per 100 m. The water content averages 25% at the bottom of the hole.

Grain Density

The grain density has averages ranging between 2.75 and 2.85 g/cm³ (Fig. 19). Grain densities between 2.60 and 2.90 g/cm³ are considered to be reliable and to be related to variations in mineralogy and organic carbon content.

Compressional Wave Velocity

Sonic velocity measurements range from 1.514 km/s at the mud line to about 1.7–1.8 km/s at the bottom of Hole 719A (Table 7; Fig. 19). Because of poor recovery and drilling disturbances, only two sonic velocity measurements were done in lithologic Units I and II (interval 0–135 mbsf). Lithologic Unit III (135–207 mbsf) shows homogeneous velocities ranging around 1.6 km/s with a slight increase with depth (0.016 km/s per 100 m). Lithologic Unit IVA (207–240 mbsf) again corresponds to a gap on the sonic velocity dataset. Lithologic Unit IVB shows a less homogeneous dataset than Unit III but a higher gradient (0.077 km/s per 100 m) can be observed in this unit. The few data collected in lithologic Unit V have an average of 1.7 km/s.

Drilling disturbances affect the sonic velocity measurements: values on the same core and same lithology range from typically 1.55 km/s in Sections 1 to about 1.65 km/s in Sections 6 and/or core catchers.

A systematic anisotropy (up to 8%–10%) was observed on relatively well-consolidated samples, the horizontal velocities being always higher than the vertical velocities.

Thermal Conductivity

The thermal conductivity measurements were routinely performed on each section from the mud line to the bottom of the hole (Fig. 19). Thermal conductivities measured at Site 719 were used for evaluation of the heat flow in connection with tempera-

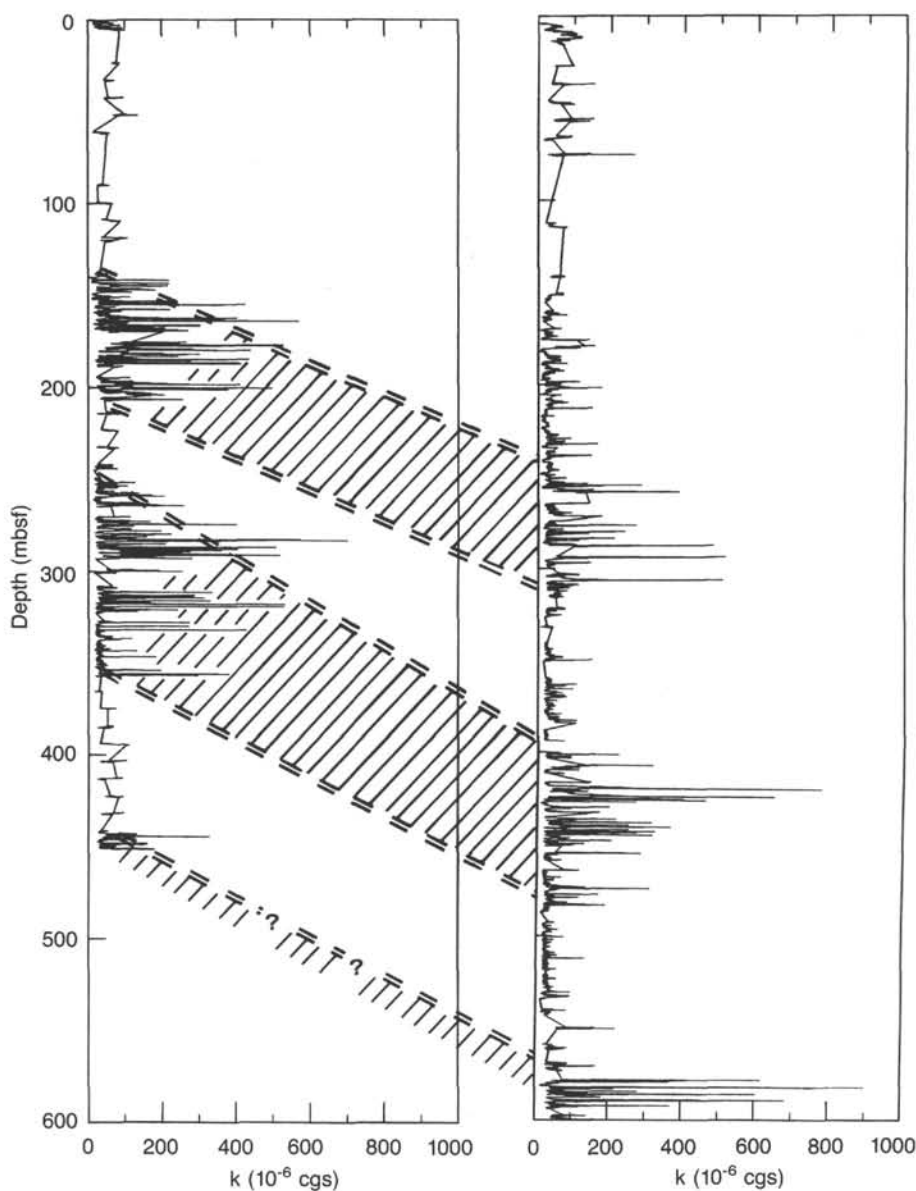


Figure 18. Possible correlation of magnetic susceptibility values from Hole 719A (left) with 717C (right). Hatched bands show suggested correlations of high-susceptibility sections of core.

ture measurements in Hole 719A (see "Heat Flow" section, this chapter). The conductivities measured range from 1.95×10^{-3} cal/(°C × cm × s) at the top of the hole to maximum values of about 5.2×10^{-3} cal/(°C × cm × s). The thermal conductivity dataset, characterized by highly variable values, appears difficult to interpret. A mean thermal conductivity of 3.34×10^{-3} cal/(°C × cm × s) was calculated for Site 719.

Undrained Shear Strength

The undrained shear strength was measured in Hole 719A down to 349.8 mbsf, below which core material was too disturbed to make valid measurements. No measurements were carried out between 4.9 and 120.2 mbsf because of low core recovery and the large amount of drilling disturbance. Values obtained for undrained shear strength are presented in Table 9 and are plotted vs. depth in Figure 19.

The undrained shear-strength vs. depth profile shows four major trends within the tested sections of Hole 719A.

1. Depths 2.24–120.21 mbsf: the shear strength increases slightly within the upper interval from 9.5 kPa at 3.79 mbsf to 49.7 kPa at 120.21 mbsf.
2. Depths 138.38–200.03 mbsf: the shear strength for this interval shows considerable scatter. The range of the shear-strength data range between 125.3 kPa (141.05 mbsf) and 397.2 kPa (166.7 mbsf). This interval corresponds to lithologic Unit III. The boundary between Units II and III is marked by a sharp increase of shear strength from 49.7 kPa at 120.21 mbsf to 132.4 kPa at 138.38 mbsf. Erosion may provide an explanation for this sharp transition.
3. Depths 202.54–251.68 mbsf: the shear-strength data for this interval are very low and consistent compared to the upper and lower regions. The values range from 208.1 kPa (204.8 mbsf) to 262.4 kPa (206.17 mbsf). This interval corresponds to the silty turbidites of lithologic Unit IVA.
4. Depths 252.96–349.8 mbsf: the shear-strength data are very scattered within this interval. The values vary between 122.9 kPa

Table 6. Index physical properties from Hole 719A.

Core	Sec./CC	Top (cm)	Bot. (cm)	Depth (mbsf)	Water content (%)	Porosity (%)	Bulk density (g/cm ³)	Dry bulk density (g/cm ³)	Grain density (g/cm ³)
1H	1	78	82	0.78	59.69	80.18	1.38	0.55	2.75
1H	2	60	64	2.10	62.02	81.01	1.36	0.51	2.62
1H	3	60	64	3.60	35.81	61.66	1.68	1.08	2.92
1H	CC	1	6	4.10	43.97	68.20	1.62	0.91	2.76
2X	1	46	50	4.66	45.62	69.66	1.59	0.87	2.77
5X	1	24	28	32.94	32.16	57.02	1.84	1.25	2.84
6X	1	47	50	42.67	29.04	52.59	1.88	1.33	2.75
7X	1	1	3	51.71	31.66	56.17	1.83	1.25	2.80
8X	1	12	17	61.32	33.50	57.53	1.79	1.19	2.72
10X	CC	1	4	80.21	30.35	54.42	1.86	1.29	2.78
11X	1	88	90	90.58	28.36	52.15	1.88	1.35	2.79
12X	1	74	76	99.94	45.80	70.18	2.48	1.35	2.82
13X	1	36	40	109.06	26.77	50.15	1.93	1.41	2.79
14X	2	46	50	120.16	31.67	55.64	1.83	1.25	2.74
16X	1	110	114	138.30	25.53	48.39	1.96	1.46	2.78
16X	2	25	29	138.95	33.97	57.65	1.77	1.17	2.68
16X	3	80	84	141.00	34.61	57.91	1.75	1.15	2.63
16X	4	60	64	142.30	34.06	58.16	1.75	1.15	2.73
16X	5	101	105	144.21	34.12	58.80	1.78	1.17	2.79
16X	6	138	142	146.08	33.57	57.45	1.78	1.19	2.71
16X	7	44	48	146.64	30.01	53.10	1.85	1.30	2.68
17X	1	99	103	147.69	34.99	60.83	1.75	1.14	2.92
17X	2	80	84	149.00	35.02	56.63	1.74	1.13	2.45
17X	3	112	116	150.82	34.07	57.41	1.77	1.16	2.64
17X	4	45	49	151.65	35.22	59.96	1.76	1.14	2.79
17X	5	90	94	153.60	35.27	60.63	1.76	1.14	2.86
17X	6	36	40	154.56	29.52	53.40	1.86	1.31	2.78
17X	7	12	16	155.82	30.80	55.58	1.86	1.29	2.85
18X	1	130	134	157.50	33.57	57.31	1.79	1.19	2.69
18X	2	140	144	159.10	33.76	55.91	1.74	1.15	2.52
18X	3	14	18	159.34	31.90	55.27	1.78	1.22	2.67
18X	4	70	74	161.40	32.71	57.26	1.80	1.21	2.79
18X	5	134	138	163.54	29.50	25.50	1.85	1.31	0.87
18X	6	90	94	164.60	34.68	52.46	1.78	1.16	2.10
18X	7	32	36	165.52	31.03	53.47	1.80	1.24	2.59
18X	CC	4	8	165.77	27.81	50.23	1.89	1.37	2.66
19X	1	80	84	166.50	31.50	60.14	1.80	1.23	3.33
19X	2	105	109	168.25	33.65	56.36	1.75	1.16	2.58
19X	3	81	85	169.51	32.77	56.19	1.81	1.22	2.67
19X	CC	35	40	170.04	29.64	52.94	1.85	1.30	2.71
20X	1	146	150	176.66	29.77	53.25	1.84	1.30	2.72
20X	2	130	134	178.00	35.83	58.22	1.73	1.11	2.53
20X	3	146	150	179.66	32.46	55.02	1.78	1.20	2.58
20X	4	70	74	180.40	28.89	52.25	1.85	1.32	2.73
20X	5	70	74	181.90	32.46	53.10	1.79	1.21	2.39
20X	6	124	128	183.94	31.52	50.69	1.79	1.22	2.26
20X	7	31	35	184.51	27.76	51.52	1.91	1.38	2.80
21X	1	69	73	185.39	31.13	54.81	1.82	1.25	2.72
21X	2	90	92	187.10	33.07	54.35	1.77	1.19	2.44
21X	3	35	37	188.05	35.43	60.08	1.75	1.13	2.78
22X	1	110	114	195.30	27.98	51.65	1.90	1.37	2.79
22X	2	33	37	196.03	31.32	53.24	1.81	1.24	2.53
22X	3	136	140	198.56	32.75	56.44	1.79	1.21	2.70
22X	4	133	137	200.03	29.71	53.17	1.87	1.31	2.72
22X	5	84	88	201.04	31.81	56.34	1.83	1.25	2.80
22X	6	91	95	202.61	33.78	56.63	1.78	1.18	2.59
23X	1	105	109	204.75	33.73	58.55	1.78	1.18	2.81
23X	2	90	94	206.10	26.54	49.98	1.93	1.42	2.81
24X	1	66	70	213.86	28.28	52.26	1.89	1.36	2.82
25X	1	52	56	223.22	27.38	51.62	1.91	1.39	2.87
27X	1	116	120	242.86	28.76	52.66	1.88	1.34	2.79
27X	2	55	59	243.75	27.30	51.50	1.91	1.39	2.87
28X	1	40	44	251.60	28.80	52.42	1.88	1.34	2.76
28X	2	21	25	252.91	27.99	51.77	1.92	1.38	2.80
28X	3	108	112	255.28	28.21	52.41	1.89	1.36	2.84

Table 6 (continued).

Core	Sec./CC	Top (cm)	Bot. (cm)	Depth (mbsf)	Water content (%)	Porosity (%)	Bulk density (g/cm ³)	Dry bulk density (g/cm ³)	Grain density (g/cm ³)
28X	4	43	47	256.13	32.51	57.69	1.81	1.22	2.87
28X	5	115	119	258.35	28.43	52.72	1.92	1.38	2.85
28X	6	60	64	259.30	32.77	57.69	1.82	1.22	2.84
28X	7	20	24	260.40	24.95	47.73	1.97	1.47	2.79
29X	1	126	132	261.96	48.67	65.05	1.99	1.02	1.97
29X	2	80	84	263.00	30.25	54.73	1.88	1.31	2.83
29X	3	45	48	264.15	6.30	20.13	1.88	1.76	3.82
30X	1	65	69	270.85	28.70	52.71	1.88	1.34	2.81
30X	2	105	109	272.75	34.24	58.95	1.80	1.19	2.79
30X	3	18	22	273.38	29.10	52.47	1.88	1.33	2.73
30X	4	53	57	275.23	33.36	57.60	1.80	1.20	2.75
30X	5	52	56	276.72	33.31	58.19	1.83	1.22	2.82
30X	6	103	107	278.73	23.70	46.76	2.06	1.57	2.87
30X	7	47	51	279.67	31.97	53.43	1.84	1.25	2.47
31X	1	62	66	280.32	26.56	49.68	1.93	1.42	2.77
31X	2	105	109	282.25	33.35	58.05	1.79	1.20	2.80
31X	3	125	129	283.95	29.85	53.49	1.86	1.31	2.74
31X	4	15	19	284.35	26.10	49.51	1.97	1.45	2.82
31X	5	4	8	285.74	28.80	51.54	1.88	1.34	2.67
31X	6	23	27	287.43	26.33	49.97	1.98	1.46	2.83
32X	1	146	150	290.66	34.47	60.13	1.81	1.19	2.91
32X	2	91	95	291.61	33.42	57.14	1.80	1.20	2.69
32X	3	53	57	292.73	25.06	48.15	1.97	1.48	2.82
33X	1	124	127	299.94	31.19	55.23	1.84	1.27	2.76
33X	2	59	62	300.79	26.60	49.86	1.94	1.42	2.78
34X	1	80	84	309.00	29.11	53.16	1.88	1.33	2.80
34X	2	106	110	310.76	28.24	52.58	1.92	1.38	2.86
34X	3	85	89	312.05	25.19	47.86	1.98	1.48	2.77
34X	4	63	67	313.33	32.00	56.15	1.81	1.23	2.76
34X	5	61	65	314.81	27.74	51.30	1.91	1.38	2.78
34X	6	85	89	316.55	30.28	54.69	1.87	1.31	2.82
34X	7	1	7	317.21	24.94	48.05	1.98	1.49	2.82
35X	1	120	124	318.90	33.52	58.36	1.77	1.17	2.82
35X	2	108	112	320.28	30.55	54.22	1.83	1.27	2.73
35X	3	124	128	321.94	28.42	52.28	1.89	1.35	2.80
35X	4	1	5	322.21	26.70	50.13	1.92	1.41	2.80
36X	1	148	150	328.68	35.27	59.49	1.75	1.13	2.73
36X	2	100	104	329.70	30.83	54.88	1.83	1.26	2.77
36X	3	104	108	331.24	24.75	47.41	2.59	1.95	2.78
36X	4	53	57	332.23	31.56	56.01	1.83	1.26	2.80
36X	5	99	103	334.19	31.19	54.98	1.44	0.99	2.73
36X	6	90	94	335.60	25.84	49.16	1.98	1.47	2.82
37X	1	130	134	338.00	31.08	54.83	1.83	1.26	2.73
37X	2	107	111	339.27	31.51	55.25	1.82	1.24	2.72
37X	3	83	84	340.53	25.88	48.88	1.94	1.44	2.78
37X	4	145	150	342.65	23.57	46.67	1.99	1.52	2.88
37X	5	58	61	343.28	29.34	53.23	1.87	1.32	2.78
37X	6	39	43	344.59	23.45	45.60	2.00	1.53	2.78
38X	1	48	52	346.68	30.40	54.27	1.86	1.29	2.76
38X	2	90	94	348.60	25.58	48.83	1.95	1.45	2.82
38X	3	114	118	350.34	33.73	58.54	1.79	1.19	2.81
38X	4	90	94	351.60	31.58	55.64	1.85	1.27	2.76
38X	5	133	137	353.53	35.45	58.66	1.76	1.13	2.62
38X	6	22	26	353.92	27.59	52.78	1.93	1.40	2.98
39X	CC	17	21	357.22	21.60	43.77	2.09	1.64	2.87
42X	CC	1	3	385.24	24.21	47.07	1.99	1.51	2.83
44X	1	37	41	403.57	22.65	44.92	2.03	1.57	2.83
47X	1	54	56	432.24	23.51	45.92	1.99	1.53	2.80
48X	1	137	141	442.57	25.02	48.39	1.97	1.47	2.85
48X	2	85	89	443.55	28.99	53.27	1.88	1.34	2.83
48X	3	95	99	445.15	24.05	47.04	1.99	1.51	2.85
48X	4	6	10	445.76	28.47	53.16	1.92	1.38	2.89
48X	5	77	81	447.97	23.65	43.07	2.02	1.54	2.48
48X	6	30	34	449.00	24.49	47.24	2.00	1.51	2.80

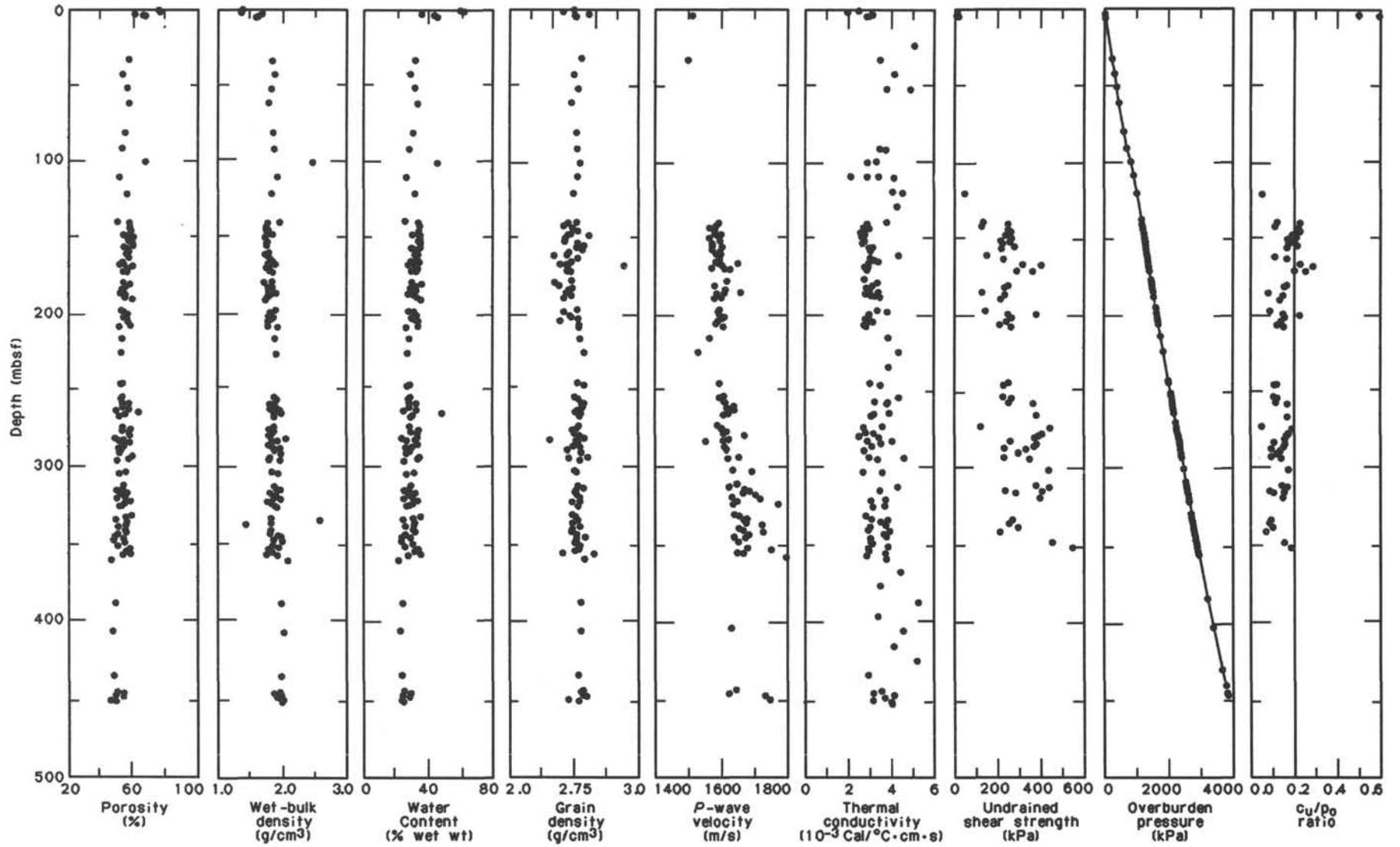


Figure 19. Porosity, bulk density, water content, grain density, sonic velocity, thermal conductivity, shear strength, effective overburden pressure, and the ratio of undrained shear strength c_u to effective overburden pressure p_o vs. depth at Hole 719A. In the last plot, sediments with a ratio of less than 0.2 are underconsolidated.

Table 7. Sonic velocity from Hole 719A.

Core	Sec.	Top (cm)	Bot. (cm)	Depth (mbsf)	Sonic velocity (m/s)
2X	1	46	50	4.66	1514.8
5X	1	24	28	32.94	1500.9
16X	2	25	29	138.95	1596.4
16X	3	80	84	141.00	1587.1
16X	4	60	64	142.30	1569.1
16X	5	101	105	144.21	1583.8
16X	6	138	142	146.08	1583.8
16X	7	44	48	146.64	1605.4
17X	1	99	103	147.69	1593.0
17X	2	80	84	149.00	1567.2
17X	3	112	116	150.82	1600.9
17X	4	45	49	151.65	1575.8
17X	5	90	94	153.60	1576.2
17X	6	36	40	154.56	1607.2
17X	7	12	16	155.82	1576.5
18X	1	130	134	157.50	1598.3
18X	2	140	144	159.10	1586.1
18X	3	14	18	159.34	1602.5
18X	4	70	74	161.40	1599.8
18X	5	134	138	163.54	1599.6
18X	6	90	94	164.60	1586.8
18X	7	32	36	165.52	1595.8
18X	CC	4	8	165.77	1655.5
19X	1	105	109	166.75	1605.6
19X	2	80	84	168.00	1576.2
19X	3	81	85	169.51	1615.4
19X	CC	35	40	170.04	1632.2
20X	1	130	134	176.50	1623.2
20X	2	146	150	178.16	1600.5
20X	3	146	150	179.66	1604.3
20X	4	70	74	180.40	1584.8
20X	5	70	74	181.90	1617.6
20X	6	124	128	183.94	1614.5
20X	7	31	35	184.51	1663.0
21X	1	69	73	185.39	1591.2
21X	2	90	92	187.10	1604.3
21X	3	35	37	188.05	1584.5
22X	1	110	114	195.30	1597.5
22X	2	33	37	196.03	1595.1
22X	3	136	140	198.56	1599.5
22X	4	133	137	200.03	1613.3
22X	5	84	88	201.04	1608.2
22X	6	91	95	202.61	1596.4
23X	1	105	109	204.75	1587.1
23X	2	90	94	206.10	1610.6
24X	1	66	70	213.86	1568.0
25X	1	52	56	223.22	1533.9
27X	2	55	59	243.75	1600.6
28X	1	40	44	251.60	1613.1
28X	2	21	25	252.91	1598.6
28X	3	108	112	255.28	1612.6
28X	4	43	47	256.13	1617.4
28X	5	115	119	258.35	1644.8
28X	6	60	64	259.30	1623.3

Table 7 (continued).

Core	Sec.	Top (cm)	Bot. (cm)	Depth (mbsf)	Sonic velocity (m/s)
28X	7	20	24	260.40	1645.4
29X	1	126	132	261.96	1627.4
29X	2	80	84	263.00	1628.0
29X	3	45	48	264.15	1612.9
30X	1	65	69	270.85	1593.4
30X	2	105	109	272.75	1608.2
30X	3	18	22	273.38	1605.9
30X	4	53	57	275.23	1622.0
30X	5	52	56	276.72	1611.4
30X	6	103	107	278.73	1677.0
30X	7	47	51	279.67	1626.5
31X	1	62	66	280.32	1611.4
31X	2	105	109	282.25	1558.4
31X	4	15	19	284.35	1614.7
31X	6	23	27	287.43	1621.5
32X	2	91	95	291.61	1658.6
32X	3	53	57	292.73	1626.5
33X	1	124	127	299.94	1639.8
33X	2	59	62	300.79	1699.3
34X	1	80	84	309.00	1653.7
34X	2	106	110	310.76	1628.5
34X	3	85	89	312.05	1677.8
34X	4	63	67	313.33	1693.9
34X	5	61	65	314.81	1672.5
34X	6	85	89	316.55	1710.2
34X	7	1	7	317.21	1637.7
35X	1	120	124	318.90	1724.8
35X	2	108	112	320.28	1655.2
35X	3	124	128	321.94	1642.6
35X	4	1	5	322.21	1780.4
36X	1	146	150	328.66	1646.0
36X	2	100	104	329.70	1660.7
36X	3	104	108	331.24	1685.6
36X	4	53	57	332.23	1674.6
36X	5	99	103	334.19	1682.8
36X	6	90	94	335.60	1731.2
37X	1	130	134	338.00	1659.0
37X	2	107	111	339.27	1673.4
37X	3	83	84	340.53	1734.9
37X	4	145	152	342.65	1690.6
37X	5	58	61	343.28	1644.6
37X	6	39	43	344.59	1680.9
38X	1	48	52	346.68	1657.3
38X	3	114	118	350.34	1686.3
38X	4	90	94	351.60	1758.2
38X	5	133	137	353.53	1654.4
38X	6	22	26	353.92	1672.7
39X	CC	17	21	357.22	1803.4
44X	1	37	41	403.57	1637.0
48X	2	85	89	443.55	1649.9
48X	3	95	99	445.15	1627.5
48X	5	77	81	447.97	1740.9
48X	6	30	34	449.00	1753.1

and 543.8 kPa at 270 and 349.8 mbsf, respectively. This interval corresponds to lithologic Unit IV.

The variations of shear-strength values within individual units appear to be facies controlled.

State of Consolidation

Methods used to estimate the state of consolidation of the sediments are described by Skempton (1970) relating undrained shear strength (cu) to effective overburden pressure (P_o).

P_o was calculated for every depth interval (Fig. 19) as described, for instance, by Richards (1962).

The relation of undrained shear strength vs. effective overburden pressure (cu/P_o) is shown in Figure 19. The cu/P_o relationship shows that most of the sediments at Site 719 are slightly underconsolidated, with the exception of the upper 5 m of the

sediments and the interval 138–200 mbsf. The sediments within these intervals are slightly overconsolidated or, rather, normally consolidated.

Overconsolidation of near-surface sediments could be caused by early cementation because apparent overconsolidation seems to be a widespread phenomenon in pelagic deep-sea sediments (Einsele, 1982). Removal of overburden or slumping may provide an explanation for the high cu/P_o values within lithologic Unit III. The conditions that would lead to underconsolidation are high rates of deposition, low permeabilities, and the presence of gas in the pore space of the sediments. The conditions of underconsolidation displayed by Site 719 sediments are attributed to high rates of sedimentation and low permeabilities of clays.

HEAT FLOW

The region of intraplate deformation in the central Indian Ocean is characterized by heat-flow measurements that show a

Table 8. Thermal conductivity measurements from Hole 719A.

Core	Sec.	Top (cm)	Bot. (cm)	Depth (mbsf)	Thermal conductivity (10^{-3} Cal/ ($^{\circ}\text{C} \times \text{cm} \times \text{s}$))
1H	1	115	116	1.15	2.4505
1H	2	62	63	2.12	1.9512
1H	3	60	61	3.60	3.0867
2X	1	70	71	4.90	2.8417
4X	1	20	21	23.40	5.0199
5X	1	20	21	32.90	3.4980
6X	1	39	40	42.59	4.1494
7X	1	39	40	52.09	4.8359
7X	1	39	40	52.09	3.7635
11X	1	20	21	89.90	3.4714
11X	1	71	72	90.41	3.7360
12X	1	20	21	99.40	3.3062
12X	1	71	72	99.91	2.8790
13X	1	12	13	108.82	2.8630
13X	1	27	28	108.97	2.1462
13X	1	43	44	109.13	3.4026
13X	1	71	72	109.41	4.1300
14X	1	100	101	119.20	4.5065
14X	2	60	61	120.30	4.0463
15X	1	40	41	128.10	4.2479
16X	1	110	111	138.30	3.7690
16X	2	62	63	139.32	2.8660
16X	3	110	111	141.30	2.7040
16X	4	62	63	142.32	2.9710
16X	5	110	111	144.30	2.6520
16X	6	62	63	145.32	2.5870
16X	7	21	22	146.41	2.7500
17X	1	111	112	147.81	2.7110
17X	2	62	63	148.82	2.6210
17X	3	111	112	150.81	2.7480
17X	4	62	63	151.82	2.6520
17X	5	111	112	153.81	3.1140
17X	6	62	63	154.82	2.9590
17X	7	40	41	156.10	3.0640
18X	1	60	61	156.80	3.0366
18X	3	60	61	159.80	4.3606
18X	4	60	61	161.30	3.0157
18X	5	107	108	163.27	3.2140
18X	6	63	64	164.33	3.4070
18X	6	114	115	164.84	2.9490
19X	CC	29	30	165.29	2.9090
19X	1	110	111	166.80	2.9060
19X	2	62	63	167.82	2.7630
19X	3	67	68	169.37	2.8790
20X	1	87	88	176.07	2.7391
20X	2	87	88	177.57	3.3493
20X	3	87	88	179.07	3.1509
20X	4	87	88	180.57	2.8208
20X	5	60	61	181.80	2.9424
20X	5	113	114	182.33	2.9607
20X	6	60	61	183.30	3.3960
20X	6	113	114	183.83	2.9310
21X	1	61	62	185.31	2.7809
21X	1	100	101	185.70	3.0252
21X	2	43	44	186.63	3.2285
21X	2	124	125	187.44	3.4654
22X	1	60	61	194.80	3.3511
22X	2	60	61	196.30	3.8023
22X	3	60	61	197.80	2.9650
22X	4	60	61	199.30	2.9428
22X	5	30	31	200.50	2.7820
22X	5	74	75	200.94	2.8542
22X	6	30	31	202.00	3.1392
22X	6	80	81	202.50	2.8692
23X	1	100	101	204.70	2.7260
23X	2	60	61	205.80	2.8146
24X	1	60	61	213.80	3.8690

Table 8 (continued).

Core	Sec.	Top (cm)	Bot. (cm)	Depth (mbsf)	Thermal conductivity (10^{-3} Cal/ ($^{\circ}\text{C} \times \text{cm} \times \text{s}$))
25X	1	40	41	223.10	4.3696
26X	1	60	61	232.80	3.8440
27X	1	115	116	242.85	3.0209
27X	2	70	71	243.90	3.4998
28X	1	115	116	252.35	4.3366
28X	2	60	61	253.30	3.8690
28X	3	115	116	255.35	3.2295
28X	4	60	61	256.30	3.8212
29X	1	115	116	261.85	3.9080
29X	2	60	61	262.80	3.2091
29X	3	60	61	264.30	3.0721
30X	1	110	111	271.30	3.5876
30X	2	60	61	272.30	2.7051
30X	3	110	111	274.30	3.1614
30X	4	60	61	275.30	2.8014
30X	5	110	111	277.30	2.5117
30X	6	60	61	278.30	3.4128
30X	7	30	31	279.50	2.8659
31X	1	110	111	280.80	4.0330
31X	2	62	63	281.82	3.4880
31X	3	110	111	283.80	3.0800
31X	5	110	111	286.80	2.7290
32X	1	110	111	290.30	2.9350
32X	2	82	83	291.52	4.5740
32X	3	57	58	292.77	3.3570
33X	1	110	111	299.80	2.7086
33X	2	62	63	300.82	3.5826
34X	2	62	63	310.32	4.2461
34X	3	110	111	312.30	3.4807
35X	1	60	61	318.30	3.7326
35X	2	60	61	319.80	3.0524
35X	3	60	61	321.30	3.6989
35X	4	20	21	322.40	3.1058
36X	1	110	111	328.30	2.8242
36X	2	110	111	329.80	3.0698
36X	3	110	111	331.30	3.8153
36X	4	110	111	332.80	3.5000
36X	5	110	111	334.30	3.7382
36X	6	62	63	335.32	3.0012
37X	1	113	114	337.83	2.9060
37X	2	60	61	338.80	3.9130
37X	3	113	114	340.83	3.6674
37X	4	60	61	341.80	3.7579
37X	5	47	48	343.17	3.0260
37X	6	47	48	344.67	3.0307
38X	1	47	48	346.67	3.1177
38X	2	47	48	348.17	3.8361
38X	3	90	91	350.10	2.9387
38X	4	90	91	351.60	2.9566
38X	5	90	91	353.10	3.7277
38X	6	15	16	353.85	2.8537
39X	1	70	71	356.40	3.7710
40X	1	14	15	365.34	4.4100
41X	1	14	15	374.84	3.4865
42X	1	70	71	384.90	5.2338
43X	1	50	51	394.20	3.3819
44X	1	40	41	403.60	4.5366
45X	1	40	41	413.10	4.0954
46X	1	30	31	422.50	5.1755
47X	1	40	41	432.10	2.9331
48X	1	110	111	442.30	3.5283
48X	2	60	61	443.30	3.1528
48X	3	110	111	445.30	4.0935
48X	4	60	61	446.30	3.6679
48X	5	110	111	448.30	3.1244
48X	6	60	61	449.30	3.9833
48X	7	30	31	450.50	4.0089

great deal of variation, but average higher than theoretically predicted for seafloor of its age (Weissel et al., 1980; Geller et al., 1983). The heat-flow measurements made during the site survey confirmed that both of these observations, made on a regional scale from scattered data points, also are found on a lo-

cal scale within the region investigated on Leg 116 (Fig. 20). Measurements ranged from 44 to 166 mW/m² with a mean of 83.7 mW/m² and a standard deviation of 21.7 mW/m².

The presence of such large variations over a short distance points to the influence of water flow in the subsurface. This was confirmed by temperature measurements at Site 718, which is

Table 9. Shear-strength measurements from Hole 719A.

Core	Sec.	Top (cm)	Bot. (cm)	Depth (mbsf)	Shear strength (kPa)
1H	2	74	75	2.24	11.8
1H	3	79	80	3.79	9.5
2X	1	70	71	4.90	16.6
14X	2	51	52	120.21	49.7
16X	1	118	119	138.38	132.4
16X	2	22	23	138.92	245.9
16X	3	85	86	141.05	125.3
16X	4	67	68	142.37	245.9
16X	5	108	109	144.28	257.7
16X	6	135	136	146.05	236.4
16X	7	40	41	146.60	234.1
17X	1	104	105	147.74	260.1
17X	2	87	88	149.07	210.4
17X	3	118	119	150.88	253.0
17X	4	60	61	151.80	219.9
17X	5	95	96	153.65	274.3
17X	6	41	42	154.61	215.2
18X	3	89	90	160.09	149.0
18X	4	123	124	161.93	224.6
18X	7	43	44	165.63	312.1
19X	1	100	101	166.70	397.2
19X	3	86	87	169.56	283.7
19X	CC	30	31	169.99	357.0
20X	3	70	71	178.90	248.3
20X	4	20	21	179.90	231.7
20X	6	76	77	183.46	127.7
21X	1	65	66	185.35	229.3
21C	CC	15	16	188.35	212.8
22X	1	102	103	195.22	144.2
22X	3	29	30	197.49	245.9
22X	3	128	129	198.48	373.6
22X	4	133	134	200.03	264.8
22X	6	84	85	202.54	238.8
23X	1	110	111	204.80	208.1
23X	2	94	95	206.14	262.4
27X	1	112	113	242.82	248.3
27X	2	40	41	243.60	227.0
28X	1	48	49	251.68	224.6
28X	2	26	27	252.96	262.4
28X	3	113	114	255.33	253.0
28X	4	45	46	256.15	364.1
29X	3	57	58	264.27	375.9
30X	1	62	63	270.82	122.9
30X	2	100	101	272.70	437.4
30X	4	60	61	275.30	401.9
30X	5	50	51	276.70	385.4
30X	6	101	102	278.71	366.5
31X	1	69	70	280.39	255.3
31X	2	112	113	282.32	375.9
31X	3	120	121	283.90	364.1
31X	4	90	91	285.10	231.7
31X	5	90	91	286.60	328.6
31X	6	91	92	288.11	293.2
32X	1	124	125	290.44	229.3
32X	2	95	96	291.65	345.2
33X	1	20	21	298.90	432.7
34X	1	85	86	309.05	373.6
34X	2	15	16	309.85	437.4
34X	3	117	118	312.37	236.4
34X	4	20	21	312.90	401.9
34X	4	85	86	313.55	281.4
34X	6	110	111	316.80	394.8
36X	3	138	139	331.58	267.2
36X	5	16	17	333.36	253.0
36X	CC	18	19	335.81	293.2
37X	2	50	51	338.70	210.4
38X	1	45	46	346.65	449.2
38X	3	60	61	349.80	543.8

located on a local heat-flow high (Fig. 20). Temperature measurements at that site showed a temperature inversion at depth. This observation can be explained by an upward flow of warm water along the fault to the north of Site 718. This water appears to spread laterally through the permeable silty turbidites

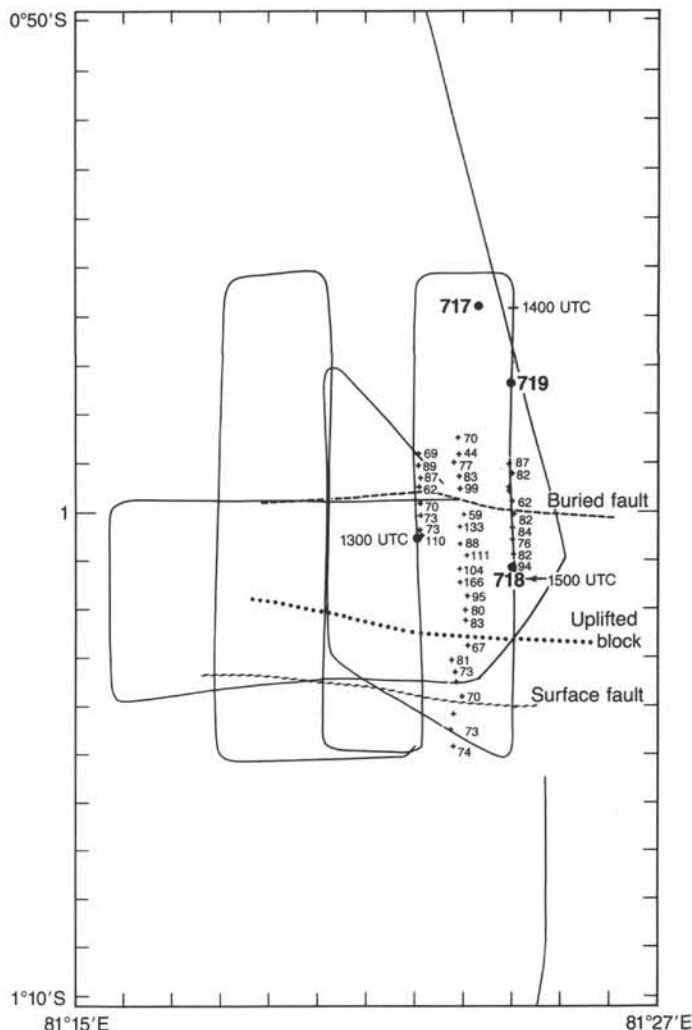


Figure 20. Site survey for Leg 116 carried out in 1986 on board *Robert D. Conrad*. Heat flow stations are shown by small crosses with value in mW/m^2 . Locations of Leg 116 sites are shown by large dots. Also shown are seismic reflection lines (heavy solid lines).

of lithologic Unit II. At the same time, cooler sea water is moving downward through permeable horizons within the underlying clayey turbidites which appear on seismic records to crop out a few km to the south of Site 718.

Downhole temperature measurements were taken in the sediment at the bottom of Hole 719A preceding Cores 116-719A-8X (61.2 mbsf), -719A-11X (89.7 mbsf), -719A-14X (118.2 mbsf), and -719A-18X (156.2 mbsf). The measurements were made with the Uyeda/Kinoshita temperature probe described in the "Explanatory Notes" chapter. The first three temperature runs were successful, yielding good-quality data. However, on the fourth run, the temperature probe fell off of the wire line during retrieval and fell 4000 m back into the hole, slightly damaging the instrument and resulting in garbled data.

Plots of temperature vs. time are shown for the three successful runs in Figure 21. The temperature vs. time curves have a characteristic shape. The lowering of the probe through the water is marked by a rapid cooling followed by a relatively constant temperature as it is held at the mud line prior to insertion. Insertion is marked by a sharp rise in temperature caused by frictional heating followed by a gradual cooling as the probe cools to the temperature of the sediments. Pullout may be accompanied by another frictional spike and the temperature profile ob-

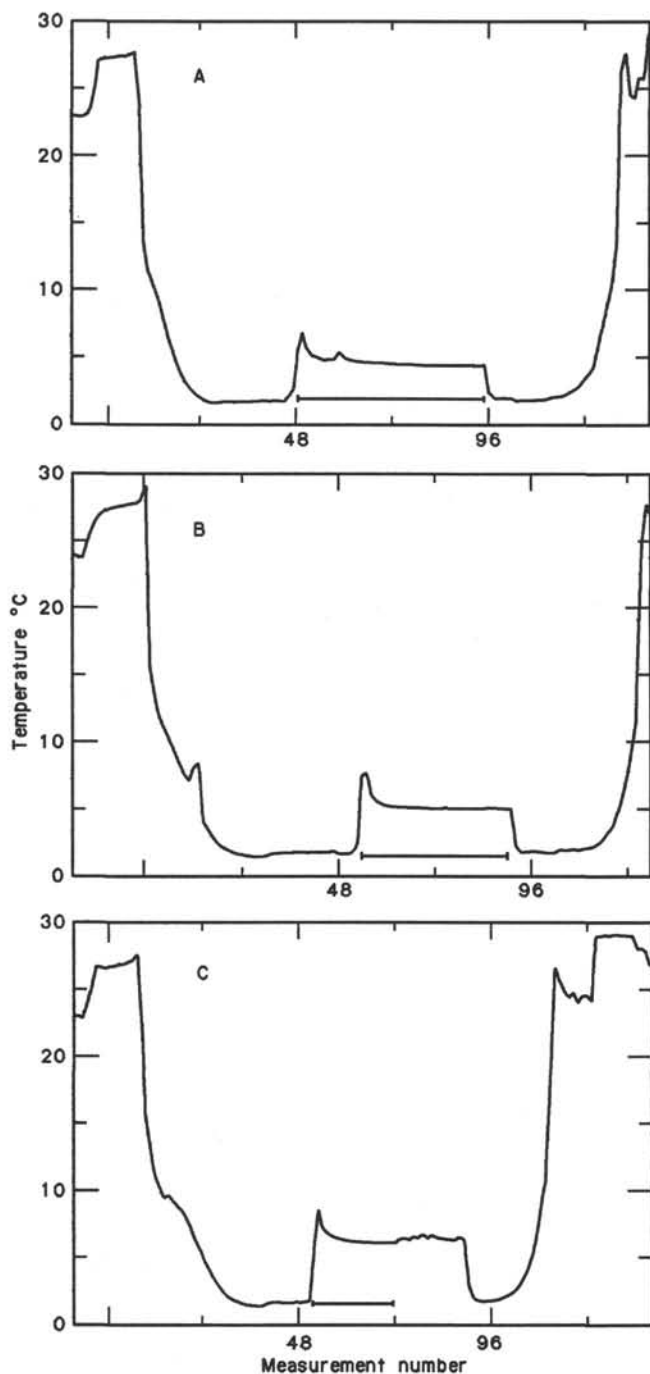


Figure 21. Barnes-Uyeda Probe temperature vs. time record for down-hole temperature measurements. Bars under temperature readings show portion of record used to extrapolate to the equilibrium temperature. (A) Depth 61.2 mbsf preceding Core 116-719A-8X. (B) 89.7 mbsf preceding Core 116-719A-11X. (C) 118.2 mbsf preceding Core 116-719A-14X.

tained during lowering is mirrored while the instrument is raised to the surface. The portion of the plot during which the probe was inserted into the sediments is marked on each plot. The temperature does not return completely to equilibrium during the time that the probe is in the sediments, but the temperature vs. time values can be extrapolated to find the asymptotically-approached equilibrium temperature.

The temperature measurements, extrapolated to equilibrium, are listed in Table 10 and plotted against depth in Figure 22. The points appear to lie on a straight line which can be fit with a slope of $27.67\text{ }^{\circ}\text{C}/\text{km}$ (standard error = 0.06). Thermal conductivity measurements in the upper 150 m of sediment have given average values of $3.2 \times 10^{-3}\text{ cal}/(^{\circ}\text{C} \times \text{cm} \times \text{s})$ or $1.34\text{ W}/(\text{m} \times ^{\circ}\text{C})$ at all three Leg 116 sites. This thermal conductivity implies a heat flow of $37.1\text{ mW}/\text{m}^2$. The temperature gradient determined at Site 719 is considerably smaller than that determined at Site 717 ($39.5\text{ }^{\circ}\text{C}/\text{km}$). The best fitting line to the Site 719 data also predicts a temperature of $2.8\text{ }^{\circ}\text{C}$ at the sea-floor, which is more than $1\text{ }^{\circ}\text{C}$ higher than the observed temperature of about $1.7\text{ }^{\circ}\text{C}$.

However, if the temperature measurements from Site 717 are plotted along with the measurements from Site 719 (Fig. 23), it can be seen that there is no great difference in the temperatures with depth at the two sites and all of the measurements appear to fall on a single trend. If a straight line is fit to all five measurements, a slope of $34.08\text{ }^{\circ}\text{C}/\text{km}$ (standard error = 0.21) is found with a projected sea-bottom temperature of $2.23\text{ }^{\circ}\text{C}$. The best fitting line when the sea-bottom temperature of $1.7\text{ }^{\circ}\text{C}$ is included in the fit has a slope of $37.93\text{ }^{\circ}\text{C}$ (standard error = 0.23) and a sea-bottom temperature of $1.84\text{ }^{\circ}\text{C}$.

It can be argued that the temperature gradient is nearly the same beneath Sites 717 and 719 and is in the range of 34 to $38\text{ }^{\circ}\text{C}/\text{km}$. The resulting heat flow through the fault block under Sites 717 and 719 is thus in the range of 45.6 to $50.9\text{ mW}/\text{m}^2$. This is very close to, although slightly less than, the theoretical heat flow for 78-Ma crust, which is $53.5\text{ mW}/\text{m}^2$ (Parsons and Sclater, 1977).

The fact that the temperature gradient in the upper 150 m of sediment is the same at Sites 717 and 719 and appears to be linear with depth would tend to suggest that hydrothermal circulation is not occurring at shallow depth above the fault block on which these two sites are located. This is in marked contrast to the block immediately to the south, where downhole temperatures at Site 718 gave direct evidence for vigorous hydrothermal circulation. However, the tip of the fault block on which Sites 717 and 719 is located is completely buried by the upper silty turbidite layer and thus the lower units are not directly exposed to sea water as they appear to be on the southern fault block. Therefore, it is probable that such a hydrothermal system would not be developed under the northern block. If this is the case, it would also be expected that surface heat-flow measurements would give relatively constant values across the northern block. However, the surface heat-flow pattern is not known across the block containing Sites 717 and 719 as the site survey of heat flow stopped just north of the fault separating the two blocks (Fig. 20). As a result there is no data other than the downhole temperature measurements on the nature of the thermal regime in the sediments around Sites 717 and 719.

SEISMIC STRATIGRAPHY

Site 719 was chosen on the basis of single-channel seismic reflection data acquired with a water-gun source during a site survey conducted by R/V *Robert D. Conrad* on cruise C2706. The

Table 10. Downhole temperature measurements at Site 719.

Measurement	Depth (mbsp)	Temperature ($^{\circ}\text{C}$)
719A-8X	61.2	4.52
719A-11X	89.7	5.24
719A-14X	118.2	6.10

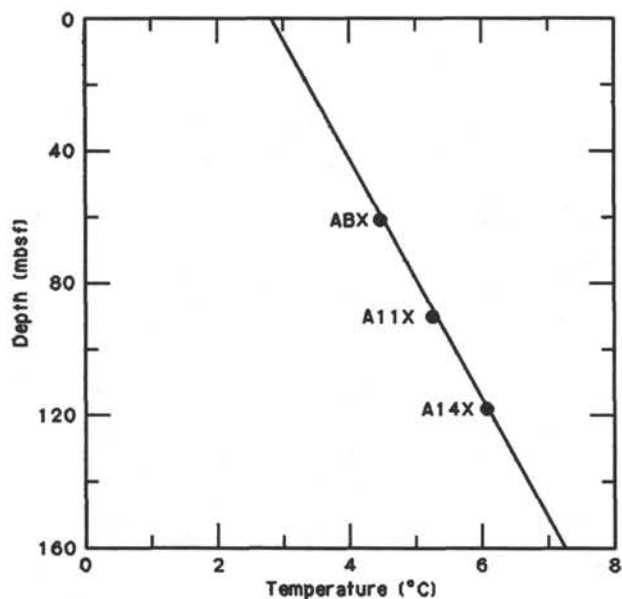


Figure 22. Plot of temperature vs. depth for Hole 719A. Solid line is geotherm determined by a least-squares fit to a straight line.

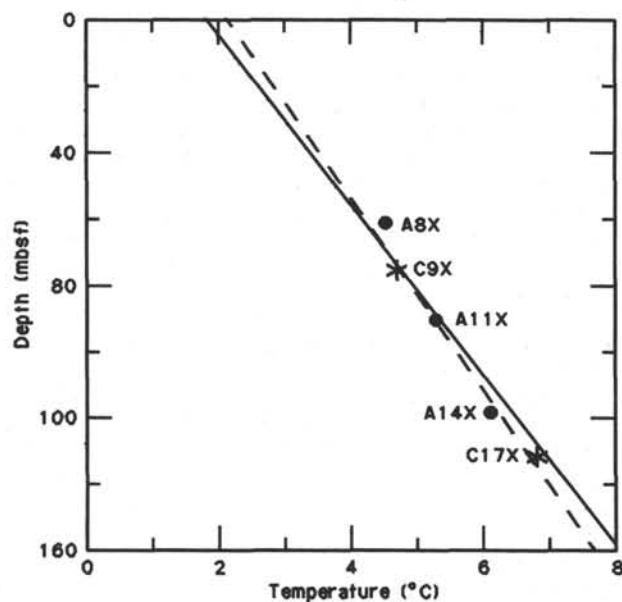


Figure 23. Plot of temperature vs. depth for Holes 717C (triangles) and 719A (dots). Dashed line is geotherm determined by a least-squares fit to a straight line. Solid line is geotherm obtained when sea bottom water temperature is included as a datum point.

Conrad seismic line was filtered using a time varying band-pass filter and single-channel migration was employed to improve the resolution and to more precisely locate the fault surfaces. The processing greatly improved the amount of detail that could be observed in the acoustic stratigraphy and removed most of the diffractions associated with the faults (Fig. 24).

The site chosen was located at time 1418Z 11 July 1986 on the *Conrad* seismic record (Fig. 2; see Fig. 20 for track chart). The site is located near the center of one of the tilted fault blocks that make up the tectonic fabric of the area of intraplate deformation in the central Indian Ocean. It is designed as a companion site to Site 717, 3.2 km to the north-northwest on

the northern (lower) edge of the same fault block. Site 717 drilled a complete syn-deformation sedimentary sequence in the axis of a synclinal structure developed in the sediments. Site 719 is located part way up the fault block in an area where the sedimentary section is attenuated, to determine the time of deformation and the history of motion on the faults. The sediment thickness at Site 719 is 1.82 s (two-way traveltime), compared to 1.96 s at Site 717.

The seismic stratigraphic section in the region studied by Leg 116 can be divided into two first-order acoustic units separated by a prominent unconformity labeled "A" on Figures 2 and 24. The lower unit is consistently 1.15 to 1.35 s thick and reflectors within it are parallel and follow the basement. This unit appears to represent the pre-deformation sedimentary sequence. Drilling at Site 717 suggested that Unconformity "A" lies within a sequence of upper Miocene silty turbidites. It was assigned an age of about 7.5 Ma by interpolation between paleontologic horizons. This identification was confirmed at Site 718, although dating there suggests a slightly older age. Unconformity "A" thus probably corresponds to the *Upper Unconformity* noted by Curray and Moore (1972) farther up the fan, which was assigned an upper Miocene age based drilling results from Site 218 of DSDP Leg 22 (Moore et al., 1974). Unconformity "A" is found at a depth of 0.71 s (two-way traveltime) at Site 717 and at 0.52 s at Site 719.

The upper acoustic unit, above Unconformity "A," records a complex history of the motion on the fault block. It includes an upper, highly layered sequence which is essentially flat lying and laps up onto the uplifted sediments at the tip of the tilted block. Further down the block, this sequence overlies and truncates inclined reflectors within the underlying sediments (Unconformity "B" on Figs. 2 and 24). The syn-depositional sediments between Unconformities "A" and "B" are characterized by numerous reflectors which are tilted up to the south (higher side of the tilted block) and which commonly terminate by pinching out against underlying reflectors. It is within this interval that most of the thinning of the sediments over the top of the tilted block occurs. Unconformity "B" is at a depth of 0.19 s at Site 717 and 0.17 s at Site 719, thus the section between the two unconformities thins from 0.50 s at Site 717 to 0.34 s at Site 719.

JOIDES Resolution approached Site 719 from Site 718 in dynamic positioning (DP) mode with 4500 m of drill pipe suspended from the ship. Thus no seismic line was acquired during the final approach. However the location of Site 719 was directly beneath the *Conrad* site survey line which was positioned with GPS navigation. This line is shown in Figure 24.

A synthetic seismogram was calculated using acoustic impedance values calculated from bulk density and compressional wave velocity obtained from the wireline logs (see "Logging" section). The synthetic program utilizes a 1-D convolution of a digitized *Conrad* air-gun source signature with the log-derived impedance profile. The program includes the effects of internal multiples but not sea-floor multiples. The calculated acoustic impedance profile and synthetic seismogram are shown with the lithologic column in Figure 25, and the synthetic seismogram is compared with the observed seismic record in Figure 26.

The upper portion of the section consists of a thin upper layer (4.0 m) of mud turbidites and pelagic calcareous muds (lithologic Unit I) over a thicker (131 m) sequence of micaceous silt turbidites (lithologic Unit II). The silts abruptly overlie a sequence of mud turbidites interbedded with pelagic clays (lithologic Unit III) at 135 m. The synthetic seismogram implies that the lithologic boundary between Units II and III corresponds to the upper of two continuous reflectors marking unconformity "B" at 170 ms depth in the seismic section (Figs. 25 and 26).

The mud turbidite and pelagic clay sequence (lithologic Units III and IV) extends from 135 to 357 m. In the reference section

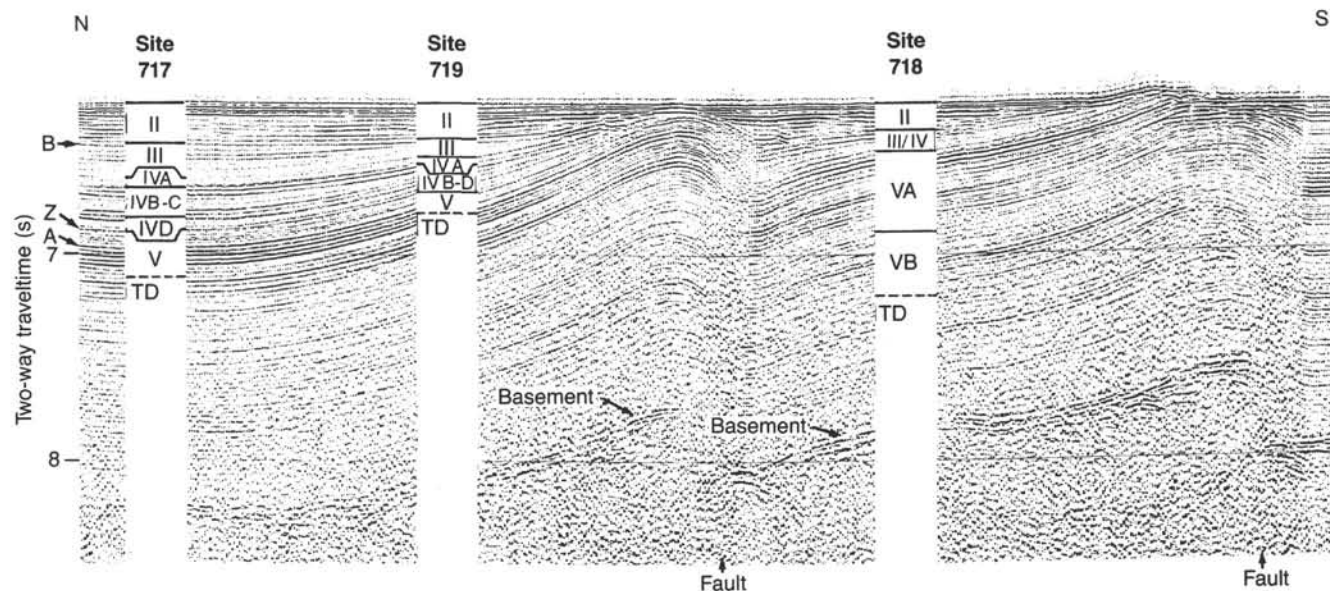


Figure 24. Single-channel seismic line across the Leg 116 sites collected during the *Conrad* survey. A lithologic column is shown for each site location with depths converted to two-way travel time. The total length of the seismic line is 18.5 km.

drilled at Site 717, this sequence contains two intervals of silty turbidites (lithologic Units IVA and IVC). Lithologic Unit IVA is also recognized at Site 719, extending from 207 to 240 mbsf. The base of this layer is characterized by a small reflector in the synthetic seismogram, which is also found in the seismic section. The synthetic peak has a characteristic wide peak (Fig. 25) also found in the observed section (Fig. 26). The lower silty unit (lithologic Unit IVC) was not recognized in the lithologic column. However, it appears to be present in the log data as a thin (10-m) zone of high acoustic impedance at 300 mbsf, corresponding to a zone of poor recovery. The logs show a sharp increase in both density and velocity at that depth. This creates a prominent reflector in the synthetic seismogram. This synthetic reflector corresponds to a reflector in the observed section that does not have a large amplitude at the location of Site 719 but increases rapidly to the north toward Site 717, where the lithologic Unit is better developed.

The top of lithologic Unit V at 357 mbsf is marked by a sharp increase in the acoustic impedance, which creates a corresponding reflector (Fig. 25). This reflector does not correspond to the Unconformity "A", but rather to a reflector labeled "Z" located about 0.09 s above. Unconformity "A" corresponds to a double-peaked reflector at the bottom of the synthetic seismogram about 90 m below the top of Unit V.

LOGGING

Three Schlumberger wireline logging tool strings were used in Hole 719B with the objective of providing a continuous record of *in-situ* physical and chemical properties of the sediments. These logs will provide a correlatable record of the lithostratigraphic as well as the seismic stratigraphic sections vs. true depth.

The first tool string was the seismic stratigraphic combination consisting of three separate instruments: (a) a digital long-spacing sonic log (LSS) measuring interval transit time of sound waves in microseconds per foot, (b) a phasor dual induction log (DIT) measuring the bulk resistivity of the formation in ohm-meters, and (c) a natural gamma spectral log (NGT) measuring the absolute magnitude of gamma radioactivity of the formation and the relative content of the primary radioactive elements

potassium (% weight) and uranium and thorium (parts per million).

The second tool string, the geochemical combination, consisted of three separate instruments: (a) a gamma spectroscopy log (GST), which measures various elemental yields in the sediments using gamma-ray spectra emitted by formation nuclei after bombardment by 14-Mev neutrons; (b) an aluminum activation clay log (AACT), which measures the weight percent of aluminum via neutron capture and subsequent emission of 1.78-Mev gamma rays; and (c) an NGT log to aid in correlation between the two logging runs.

The third tool string, the lithoporosity combination, was three instruments: (a) a lithodensity log (LDT) measuring bulk density (RHOB in units of g/cm^3) and photoelectric absorption cross section of 661 Kev gamma rays (PEF in units of barns/electron), (b) a compensated neutron-porosity log (CNT) measuring the hydrogen content of the formation and converting this into porosity (NPHI in percent using the Schlumberger limestone porosity scale), and (c) an NGT log to correlate with the other logs.

A more complete description of the logging measurements can be found in the "Explanatory Notes" chapter. The original logging data are displayed at the end of this chapter, along with correlations to core locations and recovery. The "Total" and "Computed" gamma-ray curves represent the total activity and the total activity minus the contribution from uranium. The "yield" curves from the geochemical tools (AACT and GST) represent relative counts from the specified elements, with the total count sum normalized to 1.0.

Measurements

Seismic Stratigraphic Combination

This tool string provided excellent-quality data from the bottom of the drill pipe at 87 to 450 mbsf. Although a borehole diameter measurement was not available, the sonic transit time curve indicated that the borehole was much more uniform and smaller in diameter than Hole 718C. Small washouts may have occurred in the intervals 104–119, 134–135, 158–162, and 187–189 mbsf.

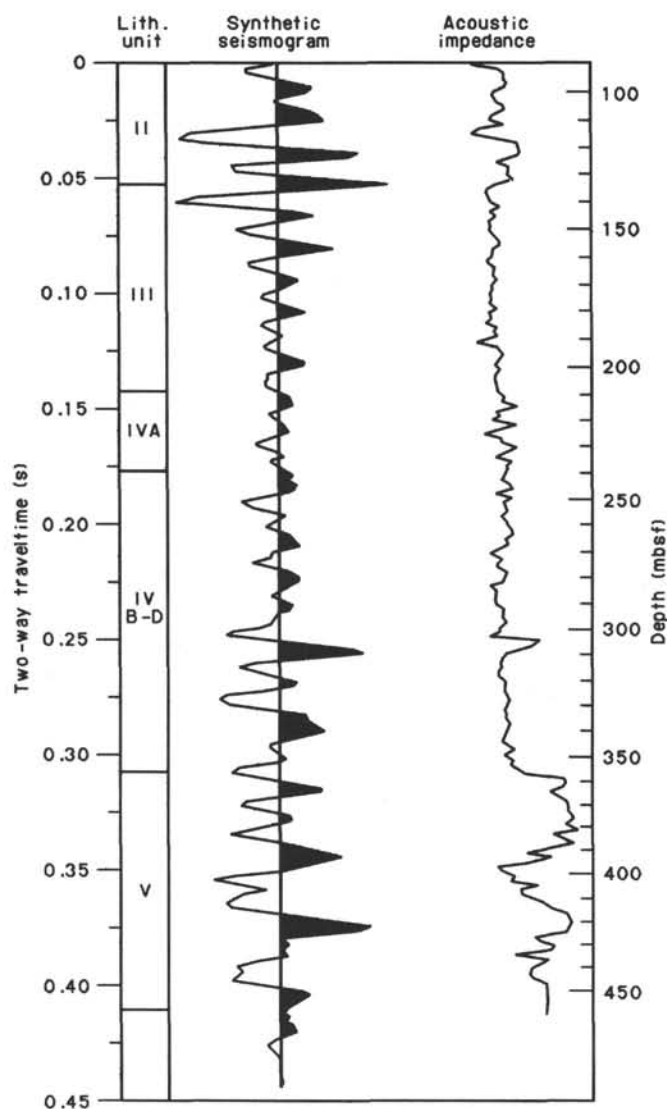


Figure 25. Synthetic seismogram for Site 719 compared with the lithologic column. The acoustic impedance profile was determined from sonic velocity and bulk-density logs. The two-way traveltme scale is linear and measured from the top of the logged interval (90 mbsf).

Sonic transit time and resistivity measurements showed a generally increasing trend downhole with relatively featureless intervals alternating with intervals of greater variability. Both of these measurements respond to porosity, and this general trend can be attributed to compaction of sediments with depth. The intervals of greater variability indicate areas of greater porosity variation. Transit time varies from approximately 185 $\mu\text{s}/\text{ft}$ at the top of the logged interval to 150 $\mu\text{s}/\text{ft}$ near the bottom. This corresponds to a sonic velocity of 1643 m/s at the top to 2027 m/s at the bottom. The maximum observed velocity was 2251 m/s at 381 mbsf.

Natural gamma-ray emissions show large variability and character throughout the hole and range from a high of 110 API units to a low 20 of API.

Geochemical Combination

This tool string provided good-quality data from the bottom of the pipe to the bottom of the hole and was run twice for improved resolution of the measurements. The AACT and GST curves shown at the end of the chapter are the result of com-

puter processing of the merged spectra from the two passes. The logs of relative abundance of sulfur, iron, calcium, silicon, titanium, and gadolinium are of good quality and will be useful in lithological identification. Chlorine and hydrogen readings are affected by borehole fluids and must be carefully examined before they are employed in any analysis.

Relative abundances as calculated by the Schlumberger logging computer can give good qualitative estimates of the component elements of the formation. Readings of negative relative abundances are an effect of the normalization of total abundances to 1.0 and should not be interpreted as true formation percentages.

Weight percentage of the elements can be found by correcting the bulk-density reading for porosity and bringing apparent grain density and atomic weight into the calculation. The computation can then be compared to clay mineralogy analysis of core samples. This data will also be invaluable in electrofacies analysis.

Silicon has a fairly constant relative abundance throughout the log, generally varying about 0.1. Maximum silicon reading is 0.15 with a minimum of 0.06. Calcium is present through most of the hole but is absent or reduced in three intervals, 89–122, 162–182, and 369 mbsf to the bottom of the hole. Calcium varies from -0.02 to 0.06 and anticorrelates with silicon. Iron is also present throughout the log about an approximate mean of 0.15. Sulfur generally correlates with iron variation with the exception of a 1-m interval at 216 mbsf. Sulfur varies between -0.05 and $+0.05$ (Fig. 27). The wet-weight percent of aluminum averages approximately 7% with a minimum of 4% and a maximum of 12%.

A detailed geochemical analysis of the GST data may show systematic differences in clay mineralogy in the units and will be compared to laboratory analysis.

Lithoporosity Combination

This tool string also provided logs of good quality over the entire logged interval.

The character of bulk density (RHOB) and neutron porosity (NPHI) readings closely correlates with sonic transit time (DELTA T) measurements reflecting the close relationships between bulk density, porosity, and transit time. This will allow a good determination of grain density as porosity is well constrained. NPHI, RHOB, and photoelectric cross-section readings may be erroneous in the intervals of large hole diameter because accurate measurements of these formation parameters requires close contact between the tool and the borehole wall.

NPHI is not a good measure of true porosity in clays as the presence of bound water in clays appears as porosity to the CNT instrument. This fact may be useful in these sequences because differences in porosity computed from RHOB, NPHI, and DELTA T may provide a clue to the sedimentary structures causing this response.

Photoelectric cross-section (PEF) measurements vary between 1.8 and 3.5 but generally are fairly constant between 2.5 and 3. PEF does not show a lot of useful detail throughout but may aid in lithological identification as it is sensitive to the iron content of clay minerals and can distinguish between calcite and dolomite.

Good-quality measurements of all parameters will allow a detailed comparison of log response to the chemical and physical structures observed in core samples. Sonic velocity data and bulk-density measurements have enabled a good synthetic seismogram to be computed (see "Seismic Stratigraphy" section).

A comparison of shaling upward and downward trends observed in NGT data with the appropriate cores will allow identification of the facies sequences responsible for these distinctive patterns.

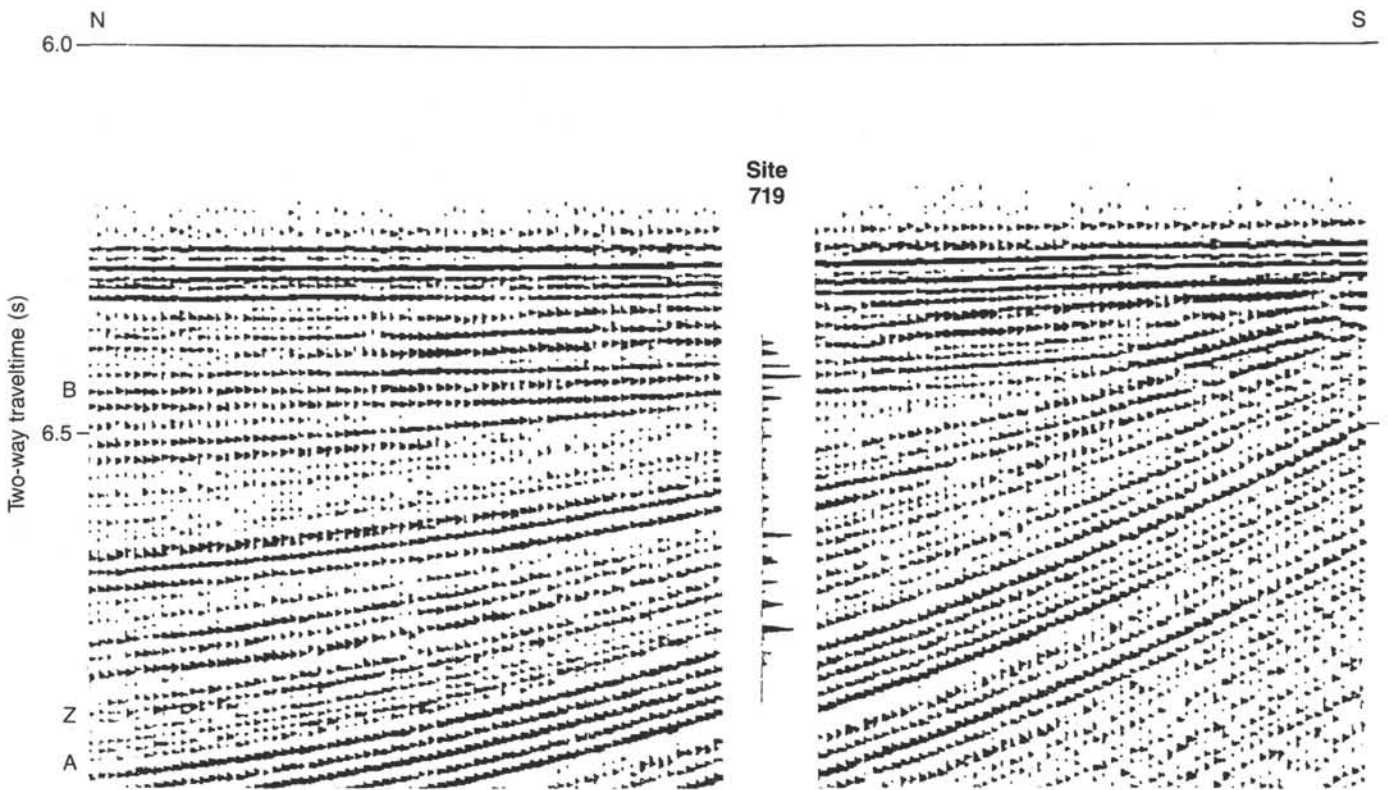


Figure 26. Single-channel seismic reflection record obtained by the *Conrad* at Site 719, along with the synthetic seismogram. Unconformities "A" and "B" and reflector "Z" discussed in text are noted to the left of the profile.

Wireline Unit Characteristics

Unit boundaries as picked from the wireline logs are chosen on the basis of distinct changes in the physical parameters measured in the borehole. As these are different criteria than those used by sedimentologists, the unit boundaries indicated on logs may not be in agreement with lithologic boundaries chosen on the basis of facies observed in cores. Wireline depth determination was based on a continuous measurement of the line length, whereas the drillers depth is based on an incremental measurement of pipe lengths (chaining). These and other reasons, including differences in stretch in the line and the pipe, can cause small discrepancies in the depths of lithologic units and wireline units.

Unit II

The lower third of lithologic Unit II was observed in this hole from the bottom of the drill string at 87 mbsf, to 138 mbsf. Two shaling-upwards sequences are observed on the NGT log. (For an explanation of the term "shaling upwards", see "Logging" section, Site 718 chapter. These sequences are characterized by a sharp decrease at the base and a gradual incremental increase in gamma emissions upwards. The bulk density (RHOB) also decreases sharply at the base to near 1.5 g/cm^3 and then increases rapidly to close to 2 g/cm^3 . Neutron porosity and interval transit time indicate higher porosity at the base of these intervals which decreases upward.

Values of RHOB recorded through the washout in this interval may be erroneously low. There is a broad interval from 91 to 102 mbsf of high gamma emissions (100–110 API) at the top of the logged interval registering RHOB of 1.9 g/cm^3 .

Between these shaling-upward sequences is what appears to be a 5-m uniform interval of lower NGT readings (40 API) at 115–120 mbsf. Lower iron and aluminum readings indicate a de-

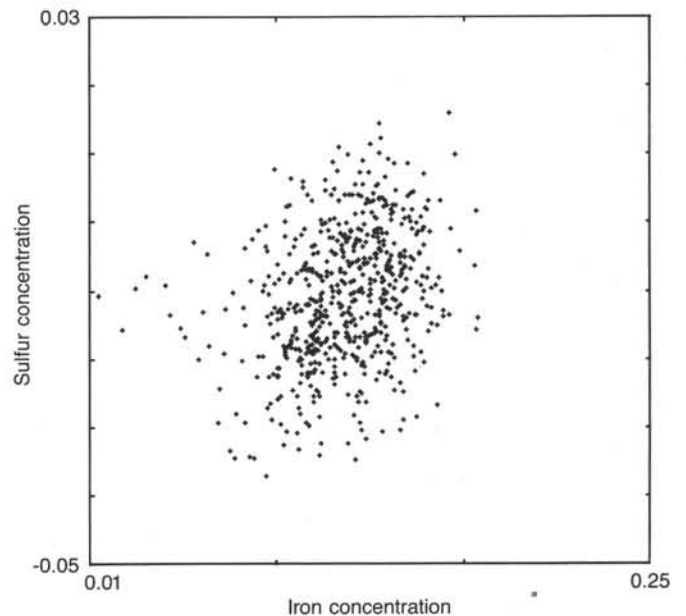


Figure 27. Relative concentrations of sulfur vs. iron over entire logged interval as measured by the geochemical combination.

crease in clay content. There is a washout indicated on the sonic curves through this interval and measurements will require corrections when borehole diameter is available. Core recovery is poor in this unit so few direct comparisons can be made. Log analysis will enable a reconstruction of the major facies in the unit.

There is a 1-m thick radioactive marker at 127 mbsf. This interval is not in a recovered interval but may correlate with similar features observed in Hole 718.

The low-density readings near the bottom of the pipe are probably not valid as the tool will lose contact with the borehole wall as the top of the string enters the pipe.

Unit III

The top of wireline Unit III at 137 mbsf was selected on the logs on the basis of the increasing RHOB and decreasing NPHI readings that depart from the measurements of these parameters in the rest of Unit III below. This trend can also be observed in sonic transit time.

Unit III is characterized by alternating shaling-upward and shaling-downward sequences on the NGT curves, some of which have sharp bottom boundaries or inflection points. Other sequences grade more gradually into each other. These observations generally agree with NGT measurements in Unit III in Hole 718C. In a shaling-upward interval, RHOB decreases upward. The converse is observed over a shaling-downward interval. NPHI measurements indicate the porosity structure in these sequences alternate rapidly but generally follow a trend that confirms the RHOB response with porosity decreasing upwards in a shaling-upward sequence. Good core recovery in this unit will allow a direct comparison of the cores to the logs.

Sonic velocity throughout this unit is fairly constant at 1690 m/s. RHOB is also relatively stable, varying around a value of 1.7 g/cm³. NPHI readings average 58%.

Geochemically, the transition from Unit II to Unit III is subtle, with a slight decrease in potassium and an increase in the neutron-capture cross section.

Unit IV

The top of Unit IV can be picked from the logs at 214 mbsf. Features on three of the curves mark this boundary. The interval transit time increases and becomes less variable above the transition; RHOB and NPHI also indicate the boundary by a sharp transition.

NGT character in Unit IV is similar to that in Hole 718C, but the magnitude of the radiation level is not appreciably lower in this unit compared to other units as it was in Hole 718C, indicating that the large borehole in 718C was shielding the tool from formation radioactivity.

NGT curves show shaling-upward sequences with sharp bottom boundaries and increasing gamma emissions upward. Relatively less uranium content is observed in this unit with respect to thorium and potassium as indicated by the tight tracking of the SGR and CGR curves. Pronounced cycling between near 100 and 60 API is observed in some intervals with wavelengths of close to 1 m. Shaling-downward sequences are not pronounced in this unit but are observed in the intervals 250–257, 329–332, and 342–347 mbsf. The latter two correspond to Cores 116-719A-36X and -718A-37X.

Transit time and RHOB measurements show considerable variation at the top of the unit in the interval 214–237 mbsf. NPHI shows two sequences of decreasing porosity. Below this, the interval 237–267 mbsf has less activity on all curves apart from a 2-m section centered at 248 mbsf. This section is characterized by a drop in the NGT, a bulk density of 1.4 g/cm³, and a PEF of 2.2. In the rest of the interval, RHOB varies between 1.7 and 1.9 g/cm³. NPHI varies about a mean of 55%. PEF reads close to 2.7 throughout.

The interval 267–357 mbsf has more variation on all curves. A distinctive 3-m interval centered at 305 mbsf has a bulk density of 2.15 g/cm³ and sonic velocity of 2100 m/s (145 μ s/ft). PEF measures 3. This may be a silty interval.

The GST and AACT measurements indicate a slight decrease in aluminum and an increase in silicon throughout the unit, along with an abrupt decrease in the neutron-capture cross section.

Unit V

The transition from Unit IV to Unit V at 357 mbsf is characterized on the logs by a decrease in sonic transit time from near 2030 to 1790 m/s (170 to 150 μ s/ft) accompanied by an increase in RHOB from 1.8 to 2.15 g/cm³ and a sharp drop in NPHI from 55% to 35%.

Unit V is very similar in character to the same unit in Hole 718C and shows shaling-upward sequences with abrupt bottom boundaries mixed with shaling-downward trends. Poor core recovery will make the log analysis of this unit important. Measurements of all parameters show greater variability in this unit than above. Sonic transit time measurements vary from a low of 1740 m/s to a high of 2260 m/s (135 to 175 μ s/ft); RHOB from 1.3 to 2.25 g/cm³; NPHI from 38% to 58%.

The geochemical measurements provide a clear indication of the transition from clay-rich to silt-rich sediments across the Unit IV/Unit V boundary at 357 mbsf. The iron yield increases from an average of 0.10 to 0.16, and the neutron-capture cross section drops from 32 capture units to 28 capture units. The wet-weight percents of aluminium and potassium remain approximately constant through both units, but the combination of lower porosity and increase in mica content in Unit V probably accounts for this. The marked increase in thorium in Unit V is also a reflection of lower porosity and increased mica content.

SUMMARY AND CONCLUSIONS

Two holes were drilled at Site 719 on the distal Bengal Fan in a water depth of 4737 m. Hole 719A was cored continuously from the seafloor to a depth of 460.2 mbsf, using one APC core and then the XCB system. Core recovery averaged 40% and, as at the two previous sites, was good in the mud sections and poor in the presumed loose silts and sandy silts. The second hole (Hole 719B) was immediately adjacent to the first and was washed down to 466 mbsf for wireline logging. Three successful logging runs were completed in good hole conditions and without technical problems.

Site 719 was drilled as a companion hole to Site 717 on the same fault block and is located 3.2 km further south and part way up the block (Fig. 2). Here, the syn-deformation section has thinned from 0.70 s at Site 717 to 0.52 s, whereas the pre-deformation section below reflector "A" remains constant at 1.2 to 1.3 s thick. The main objective at Site 719 was to determine the history of motion and uplift on the block by comparison of the sedimentary record with that at the reference Site 717.

The recovered stratigraphic section ranges from late Pleistocene to late Miocene in age and has been divided into five main lithologic units (Fig. 5). The section is in all respects very similar to that at Site 717. Unit I (0–4.0 mbsf) represents the topmost calcareous clays and mud turbidites of late Quaternary age that are present at all three sites, although the Holocene section is mostly missing, presumably due to disturbance by the initial core penetration. Unit II (4–135 mbsf) is dominated by micaceous silt turbidites in the 10% of section recovered. It is assumed that the nonrecovered intervals are of a similar lithology and, by extrapolation between widely-spaced age control, that sediment accumulation rates were well in excess of 135 m/m.y. The base of this Unit corresponds to seismic reflector "B", which at Site 719 gives the appearance of being an erosional surface (Fig. 24). Units III and IV are a 222-m thick section of mainly light- and dark-grey mud turbidites and thin interbedded pelagic clays, which are calcareous only in the upper 20–30 m.

Unit III is characterized by distinctive greenish colored biogenic turbidites, and Unit IV by an increased proportion of silty turbidites. The average accumulation rate was between 40 and 50 m/m.y. Slightly over 100 m of Unit V gray micaceous silts were penetrated before drilling was stopped just below a 10-m thick greenish clay horizon that correlates with a similar interval near the top of Unit V at Site 717. Seismic reflector "Z" marks the top of the silty section and reflector "A" is about 90 m deeper near the bottom of the hole (Fig. 24).

The biostratigraphic control at Site 719 is based largely on nanofossils as most of the other microfossil groups are either poorly preserved or absent in all but the uppermost unit. The seafloor at the site apparently lay beneath the carbonate compensation depth for much of its early history and then beneath the lysocline for the past 2-3 m.y. Siliceous fossils have probably also been removed by dissolution. Most of the fossils used for dating, therefore, have been resedimented by turbidity currents, but the general absence of mixing between nanofossil zones indicates that resedimentation took place shortly after deposition. A consistent feature of the biostratigraphic record at all three sites is the presence of a much-condensed sequence in the sedimentary record between late Pleistocene and Pliocene that occurs near the top of, but within Unit III.

The geochemical data from interstitial pore waters are remarkably similar to those from the equivalent sections at Site 717. The downhole trends in Ca, Mg, Na + K, and alkalinity indicate a significant exchange with the sediments during early diagenesis. From the inorganic carbonate content measurements and from observations on smear slides, it would appear that carbonate is being precipitated preferentially in the silty beds. Total organic carbon contents range up to 2.5%, tend to be slightly higher in the muddy units, and show a distinct cyclicity of high and low values at a spacing of between 20 and 40 m. Rock-Eval measurements show that the organic carbon consists exclusively of vitrinites and inertinites derived from land plants. Biogenic gas contents are low throughout.

Whereas all attempts at deducing magnetostratigraphy had been abandoned for Site 719 due to the problems of non-oriented cores and equatorial location encountered at the two previous sites, the data on magnetic susceptibility and intensity proved very interesting. In general, these data show the same correlation between sites as that determined from the lithostratigraphy, but with some discrepancy in the upper part of Unit III. The magnetic studies imply significant erosion (about 50 m) at the top of this interval.

A good suite of physical property measurements was obtained at Site 719 from both the shipboard analysis of core material and from the three successful logging runs. In particular, the gamma-ray, sonic, and density logs show interesting variations in character within, as well as between, lithologic units. The siltier units show higher sonic velocities than the muddy units, but also show an increased gamma reading. It is not yet clear what is causing this particular response as both clay and organic carbon contents are higher in the muds.

The temperature gradient through the upper 150 m of sediment at Site 719 is very similar to that at Site 717. When plotted together, temperature data from the two sites give a linear gradient of between 34 and 38 °C/km. These observations suggest that hydrothermal circulation is not active in the upper sedimentary section of the fault block containing Sites 717 and 719, in contrast to the results found at Site 718. This is believed to be due to the fact that the tip of the fault block to the south, on which Site 718 is situated, is exposed to the seafloor, allowing cold water influx from the surface, whereas the block beneath Sites 717 and 719 is completely buried by the upper units.

In summary, the principal results of drilling at Site 719 depend upon its correlation to and comparison with the reference Site 717.

1. The general lithostratigraphic correlation between all three sites is good (Fig. 28). The main lithologic units can be readily correlated and a number of marker horizons can also be recognized within the units. These correlations are supported by the biostratigraphic data and, for the most part, by the other shipboard analyses. However, certain discrepancies in detail remain to be resolved by further work, for example, the degree of erosion at the top of Unit III.

2. As expected, the main difference in the thickness of units occurs within the syn-deformation sequence. There is an approximate 30% reduction in this upper section between Sites 717 and 719. Most of the reduction (160 m) takes place within Units III and IV, much less within Unit II (15 m), and no observable difference is noted in the topmost part of Unit V.

3. Detailed bed-to-bed correlation indicates that this reduction has taken place in part by the thinning of individual turbidite beds, in part by the pinching-out of beds, and in part by erosion at the top of Unit III. It appears that this process has been relatively constant through most of the period since the onset of fault-block rotation at about 7.5 Ma, suggesting that movement on the fault has also been gradual. The apparent blanketing of the uplifting fault block by the silts of Unit II suggests that, since the mid-Pleistocene, the rate of sediment accumulation outstripped motion on the fault.

4. The existence of a fault block with a significant elevation above the surrounding seafloor has had a profound effect on the deposition of turbidites on this part of the fan. Many turbidity currents clearly passed over the obstacle but deposited thinner beds higher up the flank. In some cases the currents passed into a nondepositional or erosional mode; whereas other minor ones may have been deflected completely.

5. The highly condensed late Pleistocene to late Pliocene section that occurs within the top of Unit III is not yet fully understood and likely relates to a period when turbidity currents either eroded or simply did not deposit material at this part of the fan. This was presumably due to the relatively high elevation of the tip of the fault block on which the two sites are located. Alternatively, an intensified bottom circulation system coupled with a period of very low input of fan sediments may be responsible.

REFERENCES

- Barron, J. A., 1983. Latest Oligocene through early middle Miocene diatom biostratigraphy of the eastern tropical Pacific. *Mar. Micropaleontology*, 7:487-516.
- Berggren, W. A., Kent, D. V., and van Couvering, J. A., 1985. The Neogene: Part 2, Neogene geochronology and chronostratigraphy. In Snelling, N. J., (Ed), *The Chronology of the Geological Record*, *Geol. Soc. Mem.* 10:211-260.
- Boltovskoy, E., 1977. Neogene deep water benthonic foraminifera of the Indian Ocean. In Heitzler, J. R., Bolli, H. M., Davies, T. A., Saunders, J. B., and Sclater, J. G., *Indian Ocean Geology and Biostratigraphy*: Washington (American Geophysical Union), 599-616.
- Burkle, L. H., 1972. Late Cenozoic planktonic diatom zones from the eastern equatorial Pacific. *Nova Hedwigia Beihefte*, 39:217-246.
- Curry, J. R., and Moore, D. G., 1971. Growth of the Bengal deep-sea fan and denudation of the Himalayas. *Geol. Soc. Am. Bull.*, 82: 563-572.
- Curry, J. R., Emmel, F. J., Moore, D. G., and Raitt, R. W., 1982. Structure, tectonics and geological history of the northeastern Indian Ocean. In Nairn, A.E.M., and Stehli, F. G. (Eds.), *The Ocean Basins and Margins*, (Vol. 6) *The Indian Ocean*: New York (Plenum Press), 399-450.

Einsele, G., 1982. Mass physical properties of Pliocene to Quaternary Sediments in the Gulf of California, Deep Sea Drilling Project Leg 64. In Curray, J. R., Moore, D. G., et al., *Init. Repts. DSDP*, 64, Pt. 2: Washington (U.S. Govt. Printing Office), 529-542.

Emmel, F. G., and Curray, J. R., 1983. The Bengal deep sea fan, north-eastern Indian Ocean, *Geo-marine Letters*, 3:119-124.

Gansser, A., 1964. *The Geology of the Himalaya*: London (Wiley Interscience).

Gansser, A., 1981. The geodynamic history of the Himalaya. In Gupta, H. K., and Delany, F. M. (Eds.), *Zagros—Hindu Kush—Himalaya Geodynamic Evolution*: Washington (American Geophysical Union), *Geodynamics Series*, 3:111-121.

Geller, C. A., Weissel, J. K., and Anderson, R. N., 1983. Heat transfer and intraplate deformation in the central Indian Ocean. *J. Geophys. Res.*, 88:1018-1032.

Moore, D. G., Curray, J. R., Raitt, R. W., and Emmel, F. J., 1974. Stratigraphic-seismic section correlation and implications to Bengal fan history. In von der Borch, C. C., Sclater, J. G., et al., *Init. Repts. DSDP*, 22: Washington (U.S. Govt. Printing Office), 403-412.

Nigrini, C., 1971. Radiolarian zones in the Quaternary of the equatorial Pacific Ocean. In Funnell, B. M., Riedel, W. R. (Ed.). *The Micropaleontology of Oceans*: 443-461.

Nigrini, C. and Moore, T. C., 1979. A guide to modern Radiolaria. *Spec. Publ.* 16, Cushman Foundation.

Okada, H. and Bukry, D., 1980. Supplementary modification and introduction of code numbers to the low latitude coccolith biostratigraphic zonation (Bukry, 1973, 1975). *Mar. Micropaleontol.*, 5:321-325.

Parsons, B., and Sclater, J. G., 1977. An analysis of the variation of ocean floor bathymetry and heat flow with age. *J. Geophys. Res.*, 82:803-827.

Powell, C. M. A., and Conaghan, P. J., 1973. Plate tectonics and the Himalayas. *Earth Planet. Sci. Lett.*, 20:1-12.

Richards, A. F., 1962. Investigations of deep sea sediment cores II: Mass physical properties. *U.S. Navy Hydrographic Office, Tech. Rep.* 106.

Sclater, J. G., and Fisher, R. L., 1974. The evolution of the east central Indian Ocean with emphasis on the tectonic setting of the Ninety East Ridge, *Geol. Soc. Am. Bull.*, 85:683-702.

Sclater, J. G., Luyendyk, B. P., and Meinke, L., 1976. Magnetic lineations in the southern part of the Central Indian Basin. *Geol. Soc. Am. Bull.*, 87:371-378.

Stein, S., and Okal, E. A., 1978. Seismicity and tectonics of the Ninety East Ridge area: Evidence for internal deformation of the Indian plate. *J. Geophys. Res.*, 83:2233-2245.

van Morkhoven, F.P.C.M., Berggren, W. A., and Edwards, A. S., 1986. Cenozoic Cosmopolitan Deep-Water Benthic Foraminifera. *Bull. Centres Rech. Explor.—Prod. Elf-Aquitaine, Mem.* 11; Pau, 1-421.

von der Borch, C. C., Sclater, J. G., et al., 1974. *Init. Repts. DSDP*, 22: Washington (U.S. Govt. Printing Office).

Weissel, J. K., Anderson, R. N., and Geller, C. A., 1980. Deformation of the Indo-Australian plate. *Nature*, 287:284-291.

Ms 116A-107

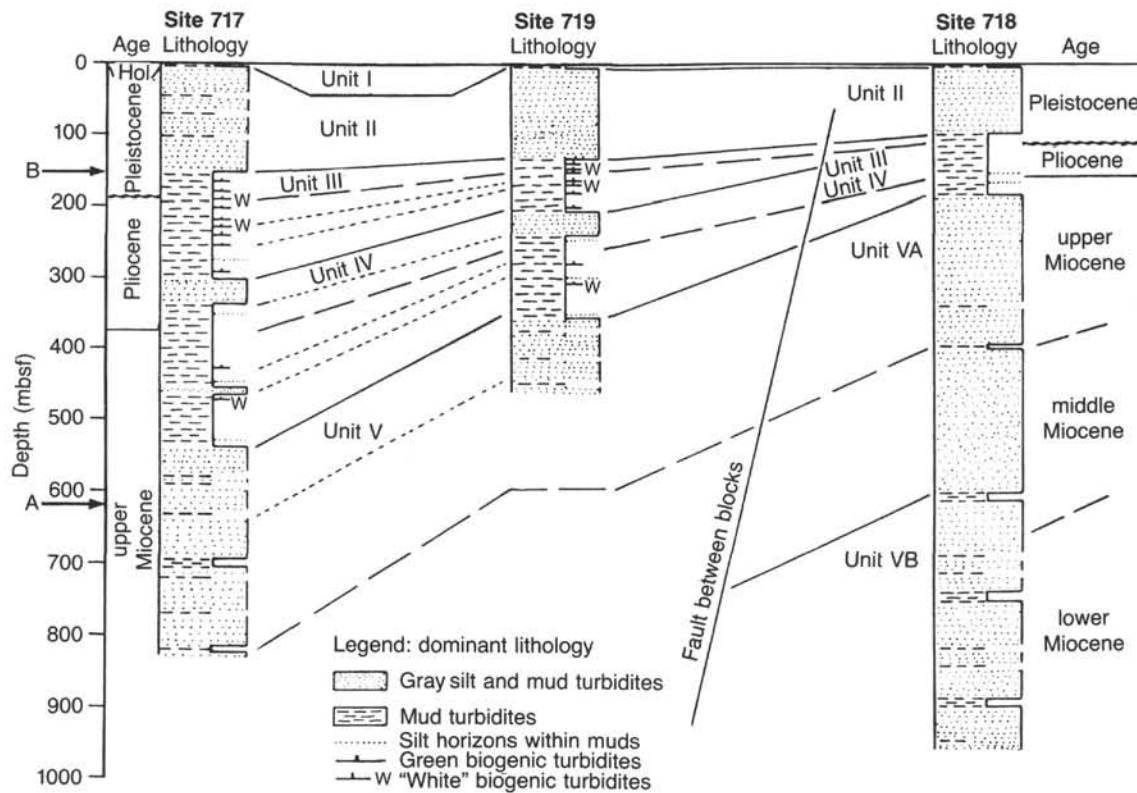
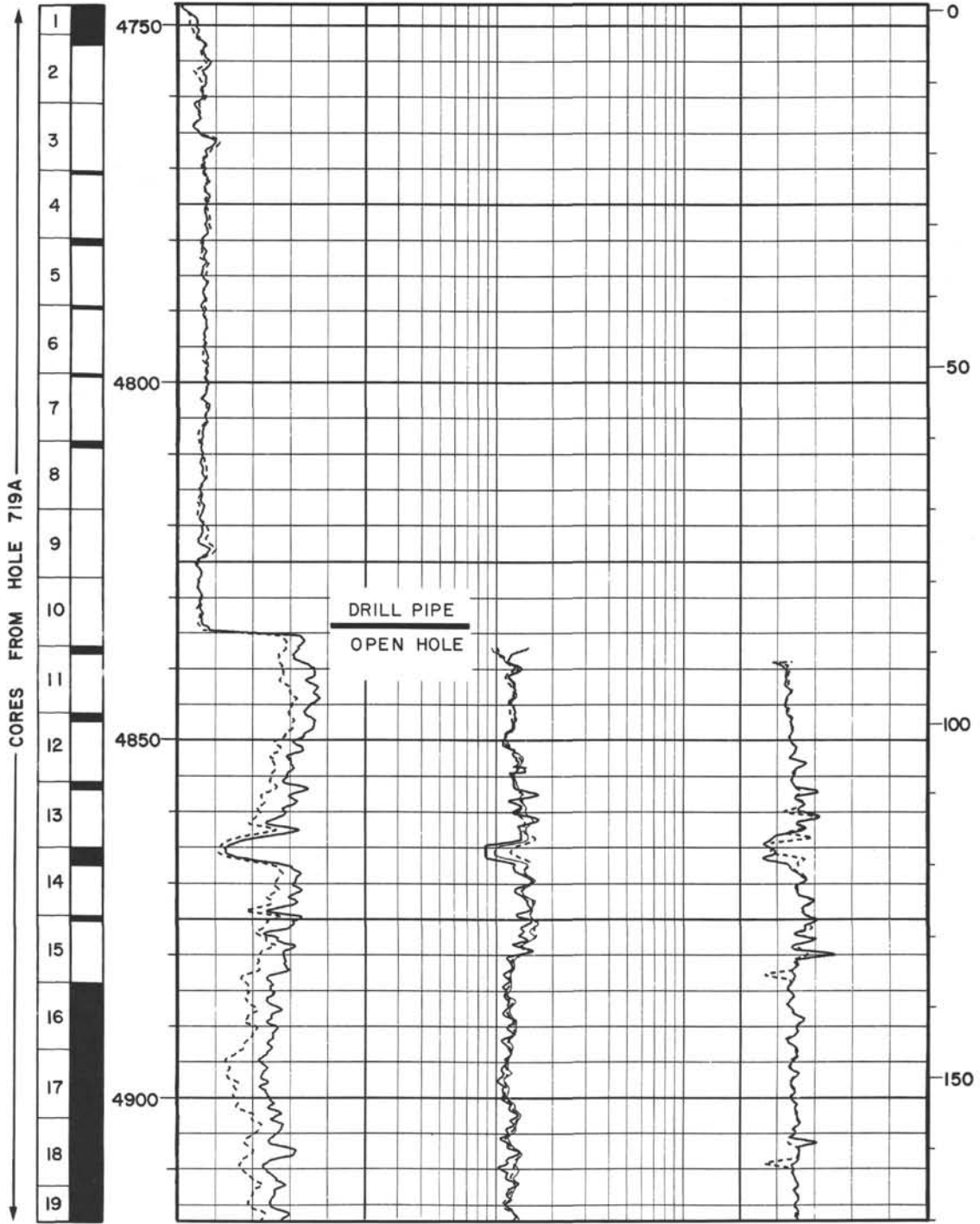


Figure 28. Lithostratigraphic correlation between Sites 717, 718, and 719.

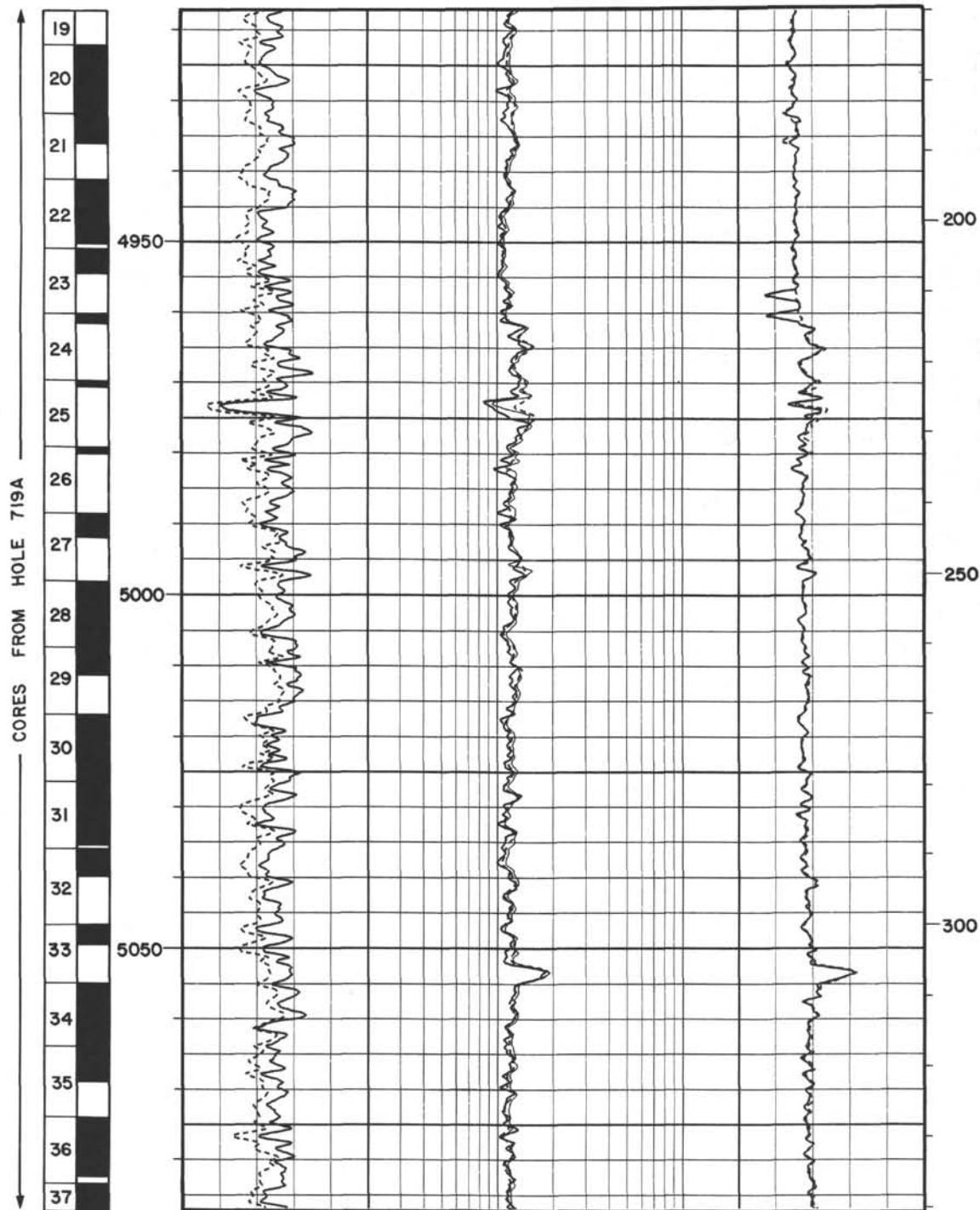
Summary Log for Hole 719B

CORE RECOVERY	DEPTH BELOW RIG FLOOR (m)	SPECTRAL GAMMA RAY		SHALLOW RESISTIVITY		TRANSIT TIME		DEPTH BELOW SEA FLOOR (m)		
		COMPUTED		DEEP RESISTIVITY		LONG SPACING				
		GAPI units	150	0.2	ohm-m	20	210		us/ft	110
		TOTAL	FOCUSED RESISTIVITY		SHORT SPACING					
0	GAPI units	150	0.2	ohm-m	20	210	us/ft	110		

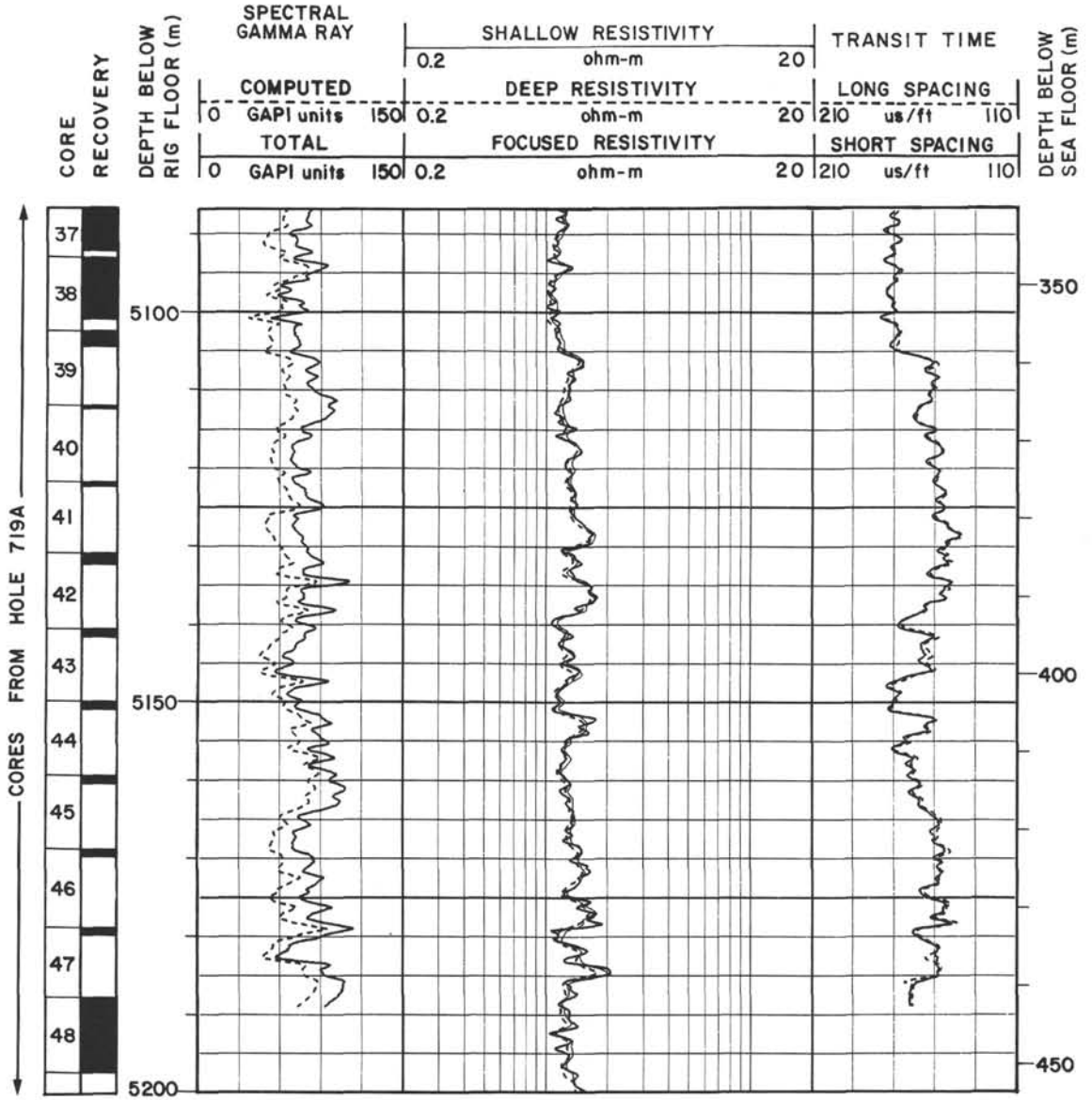


Summary Log for Hole 719B (continued)

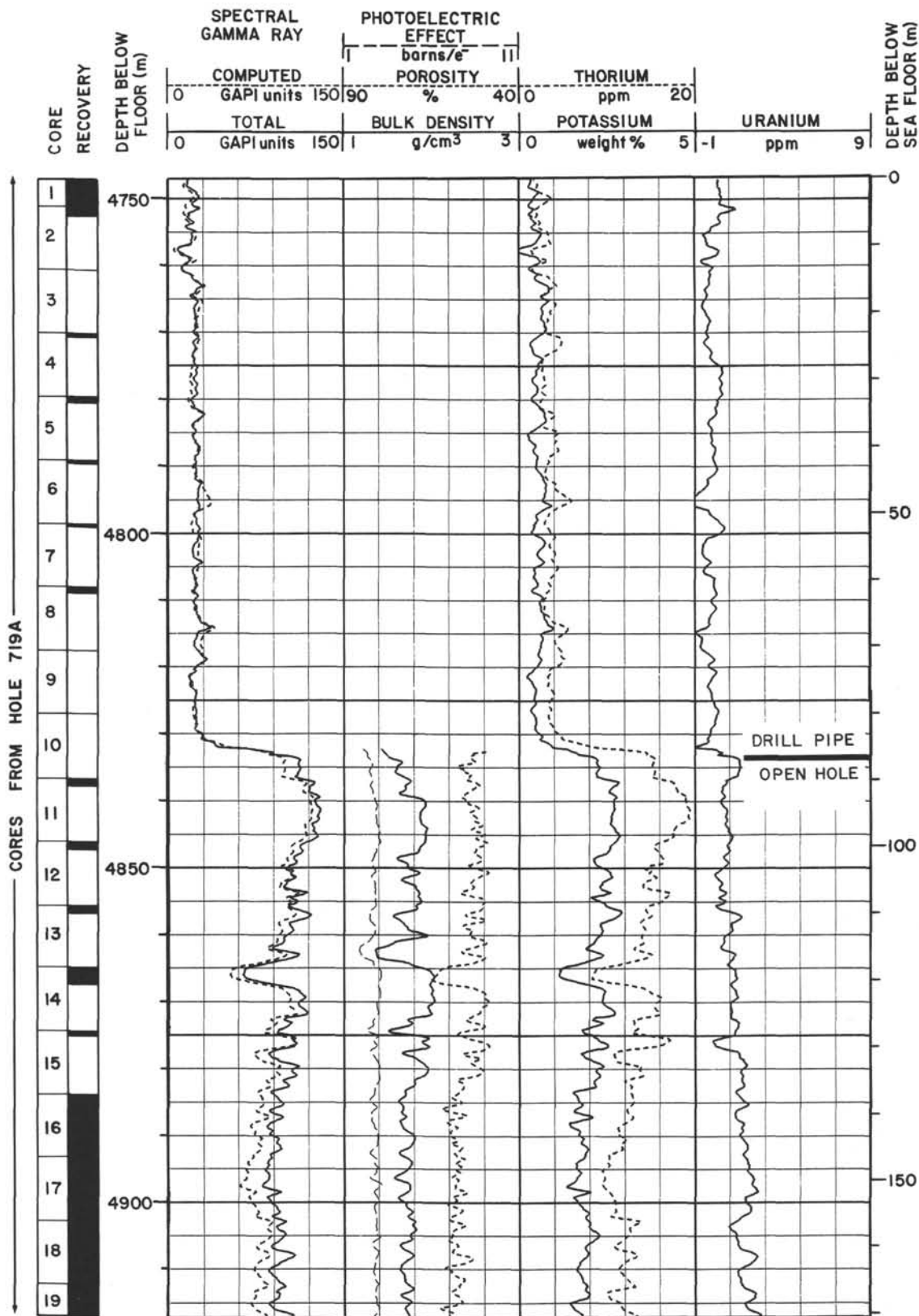
CORE RECOVERY	DEPTH BELOW RIG FLOOR (m)	SPECTRAL GAMMA RAY		SHALLOW RESISTIVITY		TRANSIT TIME		DEPTH BELOW SEA FLOOR (m)		
		COMPUTED		DEEP RESISTIVITY		LONG SPACING				
		GAPI units	150	0.2	ohm-m	20	210		us/ft	110
		TOTAL	FOCUSED RESISTIVITY		SHORT SPACING					
	0	GAPI units	150	0.2	ohm-m	20	210	us/ft	110	



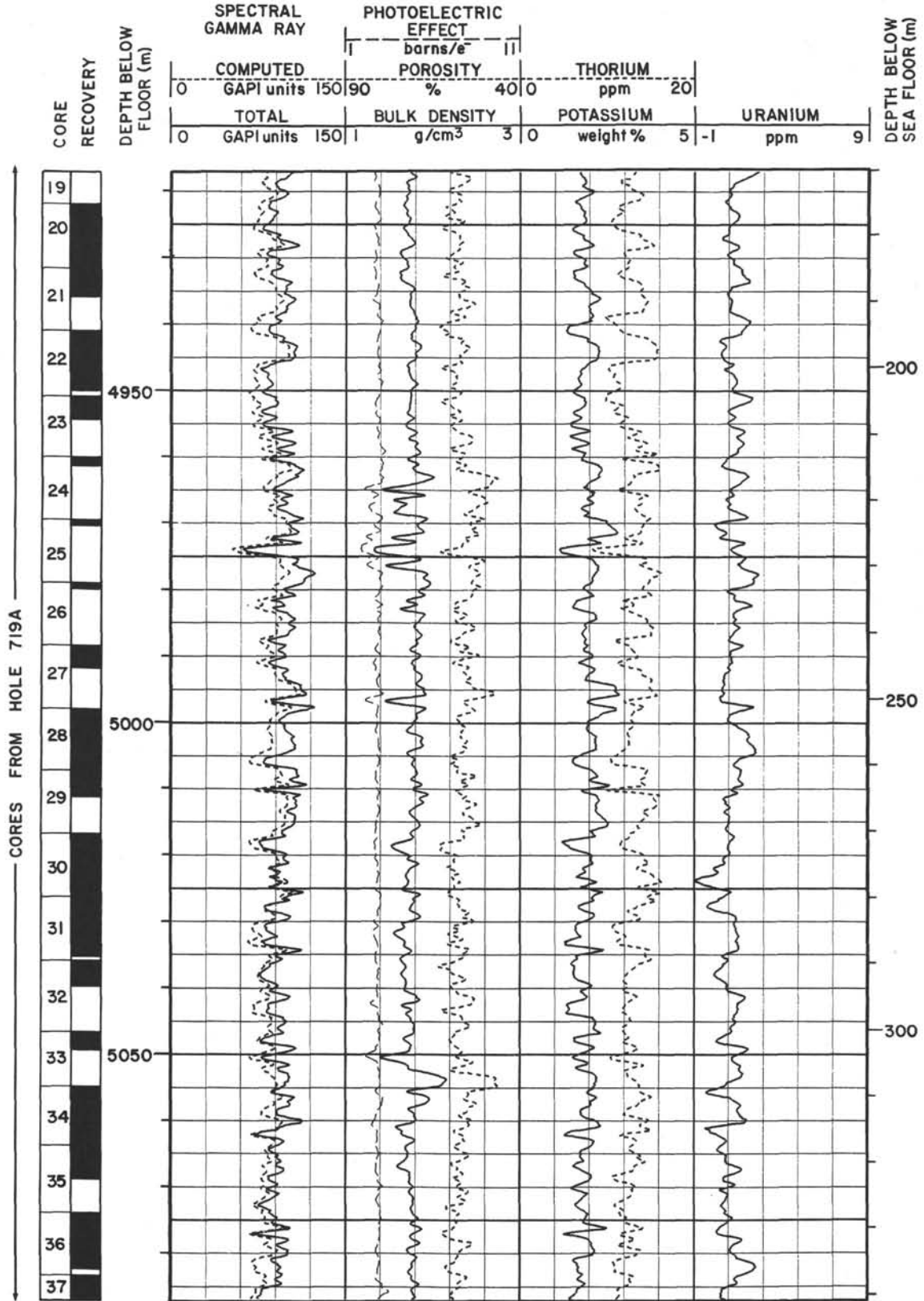
Summary Log for Hole 719B (continued)



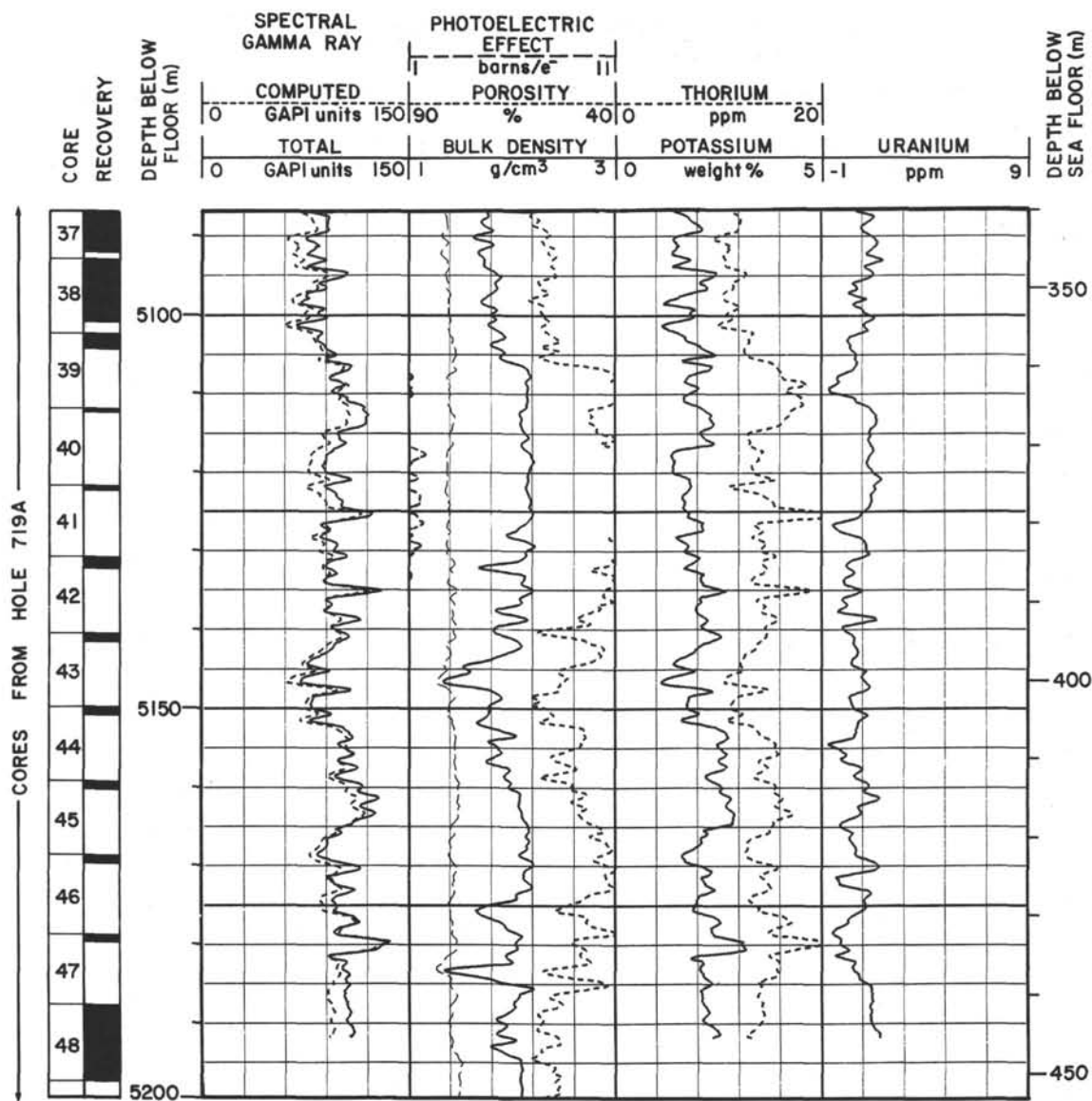
Summary Log for Hole 719B (continued)



Summary Log for Hole 719B (continued)

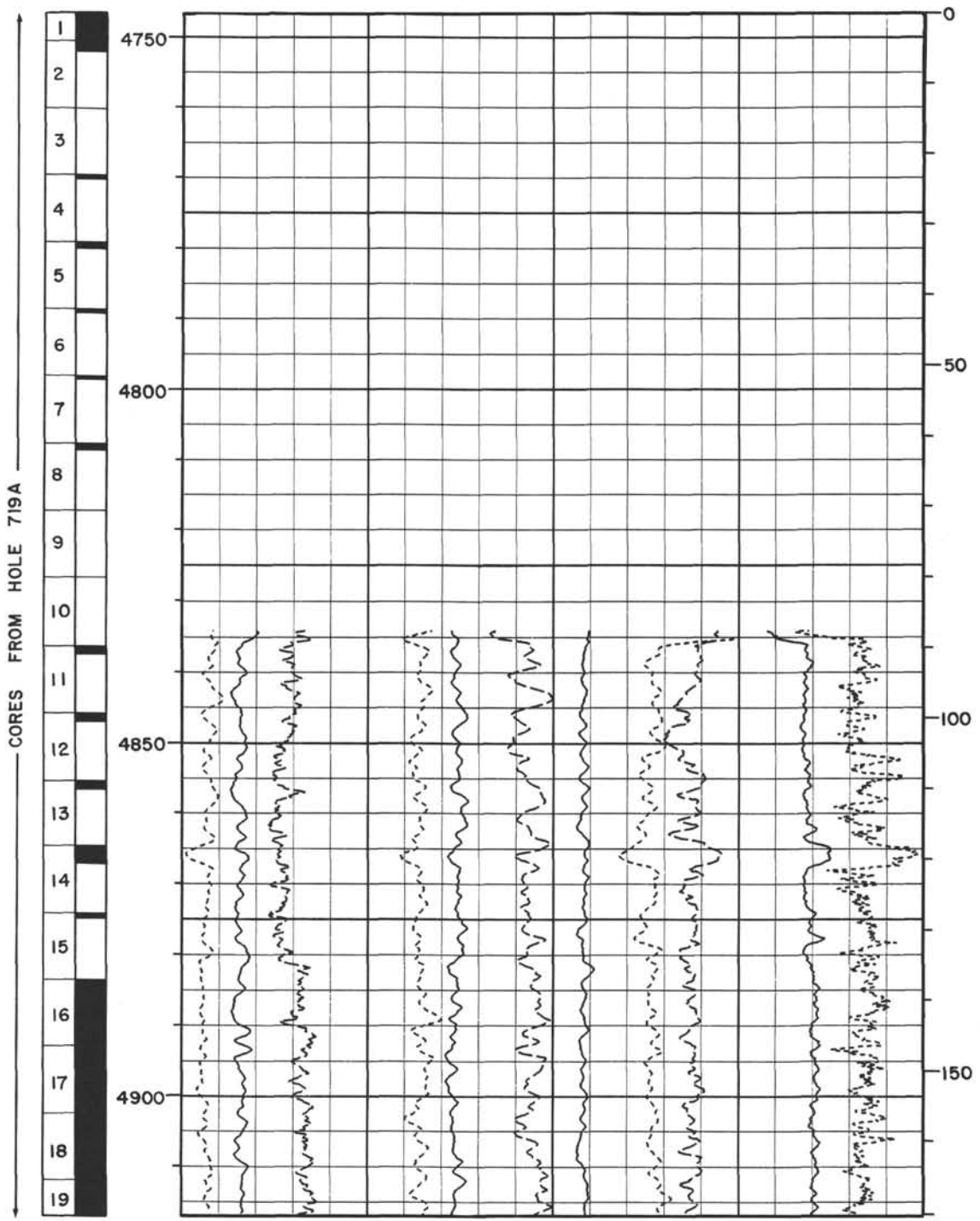


Summary Log for Hole 719B (continued)

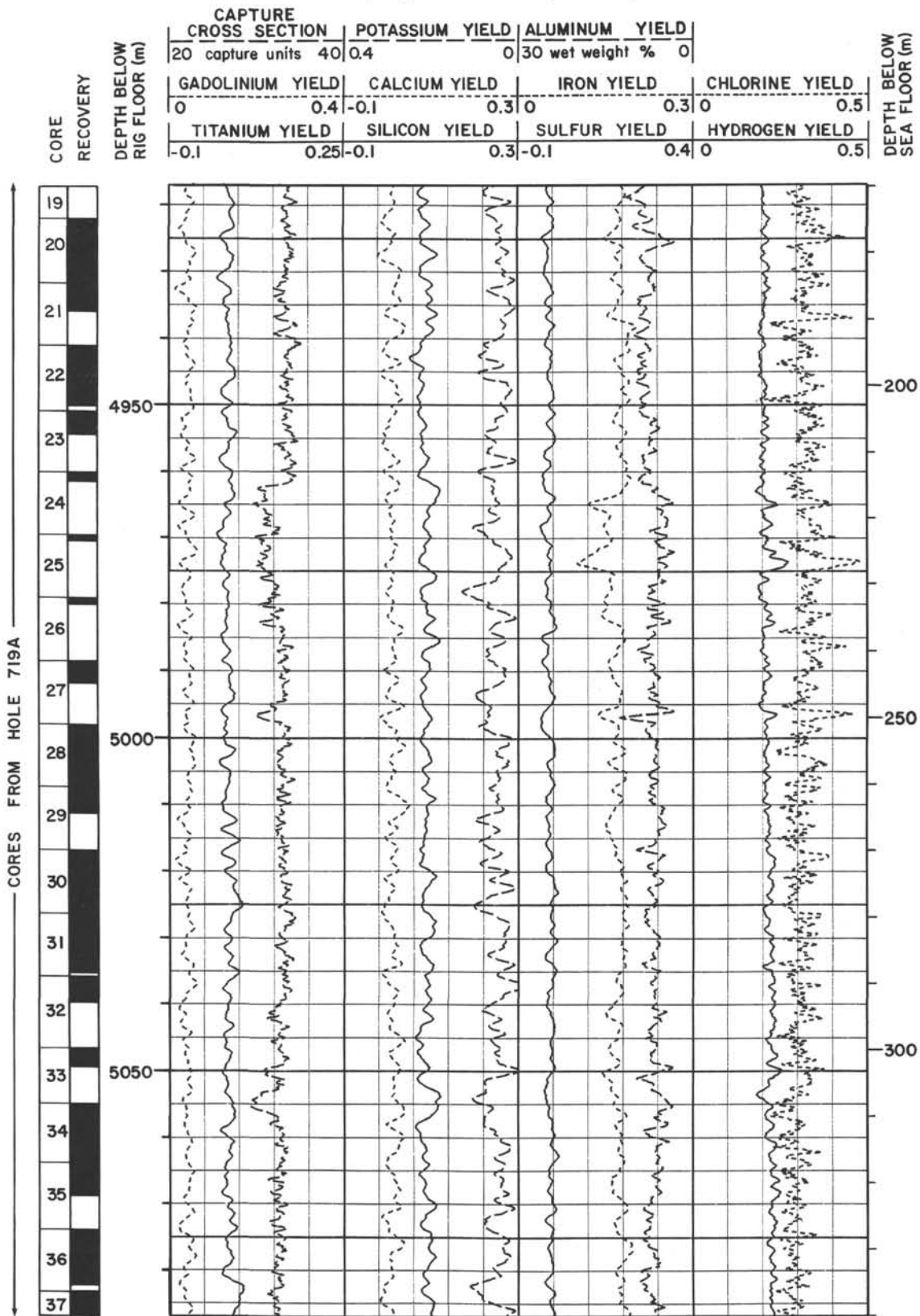


Summary Log for Hole 719B (continued)

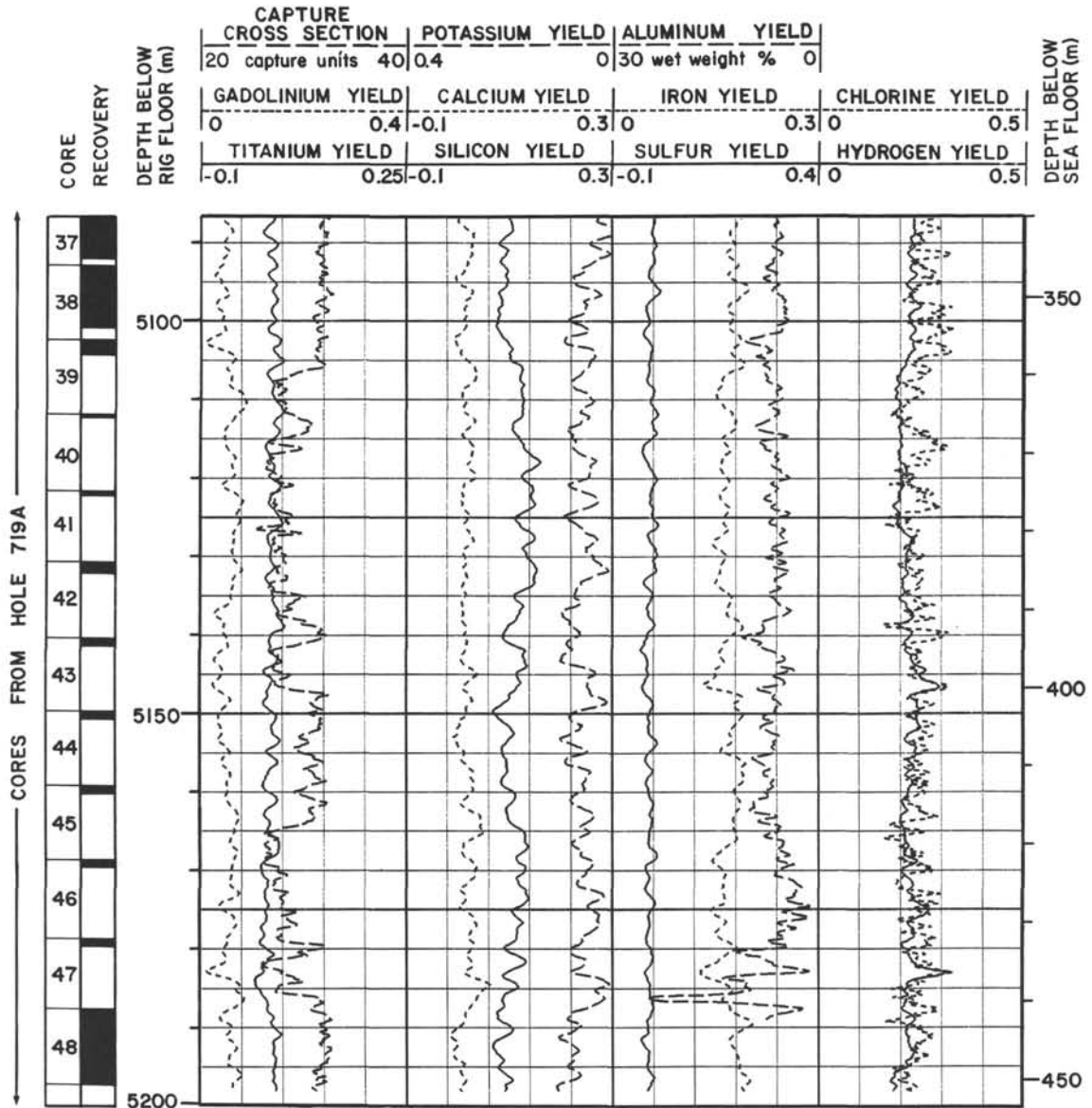
CORE RECOVERY	DEPTH BELOW RIG FLOOR (m)	CAPTURE CROSS SECTION		POTASSIUM YIELD	ALUMINUM YIELD			
		20	40	0.4	0			
		capture units		30 wet weight %				
		GADOLINIUM YIELD	CALCIUM YIELD	IRON YIELD	CHLORINE YIELD			
		0	0.4	0.3	0	0.3	0	0.5
		TITANIUM YIELD	SILICON YIELD	SULFUR YIELD	HYDROGEN YIELD			
		-0.1	0.25	0.3	-0.1	0.4	0	0.5



Summary Log for Hole 719B (continued)



Summary Log for Hole 719B (continued)



NOTE: All core description forms (“barrel sheets”) and core photographs have been printed on coated paper and bound as Section 3, near the back of the book, starting on page 213.